

DISSERTATION

EXAMINING THE IMPACTS OF CONVECTIVE ENVIRONMENTS ON STORMS USING  
OBSERVATIONS AND NUMERICAL MODELS

Submitted by

Sean William Freeman

Department of Atmospheric Science

In partial fulfillment of the requirements

For the Degree of Doctor of Philosophy

Colorado State University

Fort Collins, Colorado

Summer 2022

Doctoral Committee:

Advisor: Susan C. van den Heever

Michael M. Bell  
Sonia M. Kreidenweis  
Richard Eykholt

Copyright by Sean William Freeman 2022

All Rights Reserved

## ABSTRACT

### EXAMINING THE IMPACTS OF CONVECTIVE ENVIRONMENTS ON STORMS USING OBSERVATIONS AND NUMERICAL MODELS

Convective clouds are significant contributors to both weather and climate. While the basic environments supporting convective clouds are broadly known, there is currently no unifying theory on how joint variations in different environmental properties impact convective cloud properties. The overarching goal of this research is to assess the response of convective clouds to changes in the dynamic, thermodynamic and aerosol properties of the local environment. To achieve our goal, two tools for examining convective cloud properties and their environments are first described, developed and enhanced. This is followed by an examination of the response of convective clouds to changes in the dynamic, thermodynamic and aerosol properties using these enhanced tools.

In the first study comprising this dissertation, we assess the performance of small temperature, pressure, and humidity sensors onboard drones used to sample convective environments and convective cloud outflows by comparing them to measurements made from a tethered sonde platform suspended at the same height. Using 82 total drone flights, including nine at night, the following determinations about sensor accuracy are made. First, when examining temperature, the nighttime flight temperature errors are found to have a smaller range than the daytime temperature errors, indicating that much of the daytime error arises from exposure to solar radiation. The pressure errors demonstrate a strong dependence on horizontal wind speed with all of the error distributions being multimodal in high wind conditions. Finally, dewpoint

temperature errors are found to be larger than temperature errors. We conclude that measurements in field campaigns are more accurate when sensors are placed away from the drone's main body and associated propeller wash and are sufficiently aspirated and shielded from incoming solar radiation.

The Tracking and Object-Based Analysis of Clouds (*tobac*) tracking package is a commonly used tracking package in atmospheric science that allows for tracking of atmospheric phenomena on any variable and on any grid. We have enhanced the *tobac* tracking package to enable it to be used on more atmospheric phenomena, with a wider variety of atmospheric data and across more diverse platforms than before. New scientific improvements (three spatial dimensions and an internal spectral filtering tool) and procedural improvements (enhanced computational efficiency, internal re-gridding of data, and treatments for periodic boundary conditions) comprising this new version of *tobac* (v1.5) are described in the second study of this dissertation. These improvements have made *tobac* one of the most robust, powerful, and flexible identification and tracking tools in our field and expanded its potential use in other fields.

In the third study of this dissertation, we examine the relationship between the thermodynamic and dynamic environmental properties and deep convective clouds forming in the tropical atmosphere. To elucidate this relationship, we employ a high-resolution, long-duration, large-area numerical model simulation alongside *tobac* to build a database of convective clouds and their environments. With this database, we examine differences in the initial environment associated with individual storm strength, organization, and morphology. We find that storm strength, defined here as maximum midlevel updraft velocity, is controlled primarily by Convective Available Potential Energy (CAPE) and Precipitable Water (PW); high

CAPE ( $>2500 \text{ J kg}^{-1}$ ) and high PW (approximately 63 mm) are *both* required for midlevel CCC updraft velocities to reach at least  $10 \text{ m s}^{-1}$ . Of the CCCs with the most vigorous updrafts, 80.9% are in the upper tercile of precipitation rates, with the strongest precipitation rates requiring even higher PW. Furthermore, vertical wind shear is the primary differentiator between organized and isolated convective storms. Within the set of organized storms, we also find that linearly-oriented CCC systems have significantly weaker vertical wind shear than nonlinear CCCs in low- (0-1 km, 0-3 km) and mid-levels (0-5 km, 2-7 km). Overall, these results provide new insights into the joint environmental conditions determining the CCC properties in the tropical atmosphere.

Finally, in the fourth study of this dissertation, we build upon the third study by examining the relationship between the aerosol environment and convective precipitation using the same simulations and tracking approaches as in the third study. As the environmental aerosol concentrations are increased, the total domain-wide precipitation decreases (-3.4%). Despite the overall decrease in precipitation, the number of tracked terminal congestus clouds increases (+8%), while the number of tracked cumulonimbus clouds is decreased (-1.26%). This increase in the number of congestus clouds is accompanied by an overall weakening in their rainfall as aerosol concentration increases, with a decrease in overall rain rates and an increase in the number of clouds that do not precipitate (+10.7%). As aerosol particles increase, overall cloud droplet size gets smaller, suppressing the initial generation of rain and leading to clouds evaporating due to entrainment before they are able to precipitate.

## ACKNOWLEDGEMENTS

In science, it is said that one “stands on the shoulders of giants” to complete any work. I am fortunate to stand on the shoulders of giants both personally and professionally, and none of this work would have been possible without them. First, I would like to thank my advisor, Dr. Susan C. van den Heever. Sue has been an incredible role model, mentor, scientist, and advisor throughout the duration of my graduate work. When I first joined her group, she told me that she would be my greatest ally and greatest constructive critic. Now, after completing two degrees under her supervision, I can say with certainty that that is true. Sue has made me a better scientist, a better writer, a better presenter, and a better person. She has encouraged me to pursue the parts of science that interested me and has consistently put me in a position to succeed. Without Sue’s support and guidance, I would not have gotten to participate in any of the myriad activities that have been both fun and of critical importance to my development as a scientist and I would not be the scientist that I am today.

I also want to acknowledge my committee members Dr. Sonia Kreidenweis, Dr. Michael Bell, and Dr. Richard Eykholt. Each one of them has made important, positive contributions to this work and I have been fortunate to work with them throughout my PhD. In addition to serving on my doctoral committee, Sonia has consistently enabled opportunities for me that I would not have had otherwise, from bringing me into the proposal that founded the CSU Drone Center to allowing me to talk about my research in front of multiple important university committees.

Each of the four scientific papers that are part of this dissertation have been substantially impacted by the contributions of coauthors that are not formally part of my doctoral committee.

For Chapter 2, I want to acknowledge Dr. Jennie Bukowski, Dr. Leah Grant, Dr. Peter Marinescu, Dr. Minnie Park, and Dr. Stacey Hitchcock. Conducting this drone work would not have been possible without all of their contributions dating back to 2016. They supported me on this work both scientifically and in the collection of data, bringing me drone batteries at Christman Field even through the dead of night in the winter. Beyond their contributions to this paper, each one of them has been a valuable collaborator and friend throughout my graduate work. I felt truly privileged to work on a scientific manuscript with a group that I see not just as scientific collaborators, but friends as well.

The developments in *tobac* described in Chapter 3 would not have been possible without Alex Sokolowsky and the entire *tobac* team. Alex served as joint first author with me on this work and has been a valuable partner in the development of *tobac* and a great friend and office mate. With *tobac*, Alex and I really made a great team and complement each other's strengths. I will miss the many in depth discussions we had about *tobac* in our office. *tobac* is a large international collaborative project and working with the entire team has been a wonderful experience. I want to specifically thank Dr. Max Heikenfeld and Dr. Peter Marinescu for their work creating *tobac* in the first place; when I first heard them discussing this, I had no idea that it would become a major part of my graduate work. I also want to thank Will Jones, Julia Kukulies, and Dr. Fabian Senf for welcoming me into the world of *tobac* and allowing me to become a core maintainer of the project.

Chapter 4 benefitted greatly from the contributions of Dr. Jeff Reid at the Naval Research Laboratory and Dr. Derek Posselt at the NASA Jet Propulsion Laboratory. In addition to their contributions to this chapter specifically, Jeff and Derek have both also served as mentors for me. Derek is a source of great confidence to me and has always been supportive, even during

some of the worst days in the field. Jeff has consistently elevated me into positions that graduate students normally do not get to do, from planning flights of a multimillion dollar NASA aircraft, to serving as flight scientist, to convening sessions at the AGU conference. I would not be in the position that I am in today without Jeff's consistent support and guidance.

Despite joining a modeling group, much of my time in graduate school has been shaped by field campaigns. I want to thank the entire teams behind the CSU Convective Cloud Outflows and UpDrafts Experiment (C<sup>3</sup>LOUD-Ex), NASA Cloud, Aerosol, and Monsoon Processes Philippines Experiment (CAMP<sup>2</sup>Ex), and the NSF BioAerosols and Convective Storms (BACS) field campaigns. I also want to acknowledge Sue for encouraging me to be a full participant on all of these campaigns, and allowing me the freedom and flexibility to help out where I could on them. In addition to those acknowledged earlier above, I want to specifically thank Dr. Leah Grant for putting up with my ideas and being an invaluable mentor and partner on both C<sup>3</sup>LOUD-Ex and BACS and Rose Miller for her friendship and willingness to be a shoulder to cry on during the most stressful days of CAMP<sup>2</sup>Ex.

I also want to thank the entire van den Heever group, both past and present, for their steadfast support and confidence throughout my graduate career: Steve Saleeby, Dr. Leah Grant, Dr. Emily Riley Dellaripa, Dr. Bowen Pan, Ben Ascher, Nick Falk, Bee Leung, Christine Neumaier, Alex Sokolowsky, Kristen van Valkenburg, Dr. Minnie Park, Dr. Yasutaka Murakami, Dr. Peter Marinescu, Dr. Stacey Kawecki, Dr. Adele Igel, Dr. Aryeh Drager, Dr. Jennie Bukowski, Dr. Rick Schulte, Dr. Ross Heikes, Steve Herbener, and Dr. Brenda Dolan. Our group really is more like a family than a research group. Everyone is always willing to help out, have discussions about science, food, or anything else, and celebrate and commiserate the best and worst days of graduate school. I am especially grateful to the group for their consistent

support and discussions during the worst days of the pandemic. Without our sometimes hour-long coffee breaks and other coping strategies, I would have been much more miserable during the pandemic. Everyone in the CSU Department of Atmospheric Science, including the students, faculty, and departmental staff, are the best in the world, and are kind while doing it. Special thanks to Amanda Davey, who has endured hundreds of strange purchase requests from me over the past several years, and to Sarah Tisdale, who is an incredible source of knowledge and help on the rules governing graduate work.

Completing a doctoral degree does not happen just during graduate school, and for that reason I am grateful to all those that have supported me before my time at CSU. I am grateful for Dr. Derick Strode, who called me in the summer between my sophomore and junior years of high school and explained to me the concept of research. For Dr. Rezaul Mahmood and Dr. Astrid Suarez for being patient as a high schooler learned how to do research for the first time. For Dr. Henry Fuelberg, who was an invaluable mentor to me during my undergraduate years and allowed an undergraduate opportunities beyond my dreams, and to Dr. Nick Heath who was my first office mate and mentored me as I developed as a person and researcher. And finally for Dr. Emily Schaller who mentored me as I learned how to be a mentor and enabled hundreds of young scientists an incredible experience through the NASA Student Airborne Research Program (SARP).

I am fortunate to be surrounded by numerous friends and family that continue to help me succeed. My fiancée Dr. Anna Walter has put up with me for well over a decade at this point and has always been kind, encouraging, and willing to listen to my complaints and whatever interests me at the moment. Anna has also turned me into a cat person, and for that I want to thank Minerva, Molly, Socks, and Nyx Walter (all cats) for their warmth, meows, and for only sitting

on my keyboard sometimes. My parents, Will and Lynn, have been consistently supportive, even as I extended my graduate career beyond what they—or I—thought possible. Justin Whitaker and Alissa Williams have been dear friends to me ever since I arrived at CSU. They have traveled with me, laughed with me, cried with me, and have always been there for me. Minnie Park and Jennie Bukowski have both been continuous sources of inspiration for me and have been there to listen to my many rants. Emily Bell, Rick Schulte, Tyler Slonecki, Aryeh Drager, Bee Leung, and the entire intermural and kickball teams have been a consistent source of fun and have always made me feel better after work.

Finally, this work has been supported by NSF through the Graduate Research Fellowship Program via #DGE-1321845 and the NASA CAMP<sup>2</sup>Ex field project, #80NSSC18K0149. Resources supporting the work in Chapters 4 and 5 were provided by the NASA High-End Computing (HEC) Program through the NASA Advanced Supercomputing (NAS) division at Ames Research Center.

# TABLE OF CONTENTS

ABSTRACT.....	ii
ACKNOWLEDGEMENTS.....	v
Chapter 1: Introduction.....	1
1.1. Importance of Convective Clouds .....	1
1.2. Convective Cloud Environments.....	1
1.3. Dissertation Outline and Science Questions.....	3
Chapter 2: Where Should the Sensor Go? An Evaluation of Multirotor Drone Sensor Siting Locations.....	7
2.1. Introduction.....	7
2.2. Methodology.....	10
a. Drone and Sensor Setup.....	11
b. Drone and Sensor Setup.....	13
c. Sampling Conditions.....	15
d. Data Quality Control.....	16
2.3. Results.....	16
a. Daytime Temperature.....	17
b. Nighttime Temperature.....	20
c. Pressure .....	22
d. Dewpoint Temperature .....	24
e. Temperature and Dewpoint Temperature Gradients.....	25
2.4. Discussion and Implications for Field Campaigns .....	27

2.5. Conclusions.....	29
2.6. Tables and Figures .....	32
Chapter 3: <i>tobac</i> v1.5: Introducing Fast 3D Tracking and Other Enhancements for Identifying Meteorological Phenomena .....	43
3.1. Introduction.....	43
3.2. <i>tobac</i> v1.2 overview.....	47
3.3. <i>tobac</i> v1.5 – Scientific Improvements .....	51
a. 3D Tracking .....	51
b. Spectral Filtering.....	54
3.4. <i>tobac</i> v1.5 – Procedural Improvements .....	56
a. Code Optimization .....	56
b. Remapping Data on Different Grids .....	57
c. PBC Treatments .....	58
3.5. Summary and Conclusions .....	60
3.6. Figures .....	62
Chapter 4: Dynamic and Thermodynamic Environmental Modulation of Tropical Congestus and Cumulonimbus in the Maritime Continent .....	69
4.1. Introduction.....	69
4.2. Numerical Model and Experiment Setup.....	72
4.3. CCC Identification and Tracking.....	74
a. Tracking Step 1: CCC Feature Identification.....	74
b. Tracking Step 2: Full-cloud volume segmentation.....	75
c. Tracking Step 3: CCC Tracking.....	75

d. Determining CCC Properties .....	76
e. Determining CCC Environmental Properties.....	79
4.4. Results.....	81
a. Convective Environments associated with Storm Intensity .....	82
b. Stratifying by convective organization .....	88
c. Organized Storm Linearity.....	90
4.5. Summary and Discussion.....	92
4.6. Tables and Figures .....	96
Chapter 5: Aerosol-induced Enhancement of Congestus and Suppression of Cumulonimbus Clouds in the Tropics .....	108
5.1. Introduction.....	108
5.2. Methodology .....	110
a. Numerical Simulation Experiments .....	110
b. CCC Identification and Tracking.....	111
5.3. Results.....	111
a. Precipitation Distribution Changes .....	112
b. Tracked CCC Changes.....	113
c. Convective Cloud Organization .....	115
5.4. Conclusions.....	115
5.5. Tables and Figures .....	118
Chapter 6: Conclusions .....	122
6.1. Summary of Studies.....	122
6.2. Implications of this research and future work .....	126

References..... 129

## CHAPTER 1: INTRODUCTION

### 1.1. Importance of Convective Clouds

Convective clouds are essential components of the atmospheric system at local through global spatial scales and weather and climate temporal scales. They are responsible for many different weather hazards, including flooding, tornadoes, large hail, and strong winds. On a global scale, convective clouds are the source of about half of the total rainfall on earth (Yang and Smith 2008) and are important contributors to the global circulation (Riehl and Malkus 1958). The formation and development of convective clouds require certain thermodynamic, dynamic, and aerosol environmental conditions, and the combination of environmental parameters can change the behavior of the clouds that form. Changes to the global environment will inevitably also cause variations in these environmental properties, which can then lead to changes to the convective clouds that form. These variations in convective cloud properties are likely to produce immediate changes to the local weather effects, and, subsequently feedbacks to the global circulation and climate. Understanding the impacts of environmental parameters on convective clouds is therefore critical for processes across weather and climate scales.

### 1.2. Convective Cloud Environments

The basic properties of environments favorable for convective clouds are already broadly known and understood. In the extreme case, clouds cannot form in an environment with no water vapor, as vapor is required to condense for clouds to form in the first place. In a more realistic case, the development of convective clouds requires a vertical temperature profile such that as air rises, the latent energy released by condensing or freezing water vapor into liquid drops or ice particles allows the upward moving air to remain warmer and, therefore, less dense than

surrounding environmental air. Thermodynamic characteristics are not the only environmental properties that have important impacts on convection. Dynamical properties, such as wind shear, are also critical contributors to convective properties, in particular how and whether convective clouds tend to organize themselves (Klemp and Wilhelmson 1978; Weisman and Klemp 1982; LeMone et al. 1998; Johnson et al. 2005) or rotate, as in the case of supercell thunderstorms (Doswell 1987).

The thermodynamic and dynamic properties of the local environment are not the only contributor to convective properties. Convective clouds also require the presence of aerosol particles that water vapor can condense onto in order to become cloud drops. These cloud condensation nuclei (CCN) are a subset of aerosol particles in the atmosphere, and convective cloud properties can be highly influenced by their number, size, type, and properties (Squires 1956; Twomey 1960; Albrecht 1989). Further, through their effects on radiative properties, CCN may influence the thermodynamic environment (Shine et al. 1990).

While the basic properties of the thermodynamic, dynamic, and aerosol environments required to produce and maintain convective clouds are known, there is still not a universal theory linking joint variations in environmental conditions to convective properties. The desire to quantify this environment – convective storm relationship has been highlighted in recent years (National Academy of Science, 2017), in particular as we now enter the era of observations and numerical modeling of individual convective cloud properties globally. To couple to these observations and model data of convective properties on a global scale, new technologies for observing convective environments and quantifying the links between environments and convective clouds must be developed. Further, we must first understand the relationships

between environments and convective cloud properties on local scales before we can understand their impacts globally.

### **1.3. Dissertation Outline and Science Questions**

As the relationships between environments and convective cloud properties are not fully known, the primary goal of this dissertation is to first describe new tools for sampling convective environments and then to use those tools to examine the links between environment properties and convective clouds, regionally.

In Chapter 2<sup>1</sup>, an extensive analysis of the use of multirotor drones (also known as small Uncrewed Aerial Systems [sUAS] or small Uncrewed Aerial Vehicles [sUAV]) for sampling key thermodynamic parameters in the boundary layer is performed. While fixed-wing drones have long been used in atmospheric science (Vorontsov et al. 1958), the use of multirotor drones is much more recent, thanks to advances in flight controller and battery technology. The accuracy of atmospheric environmental parameters measured from fixed-wing drones is well quantified, thanks to their long heritage and overall similarity to research aircraft platforms. However, because of their multiple rotors and internal electronics, the measurement accuracy from multirotor drones is not as well understood. While some previous studies have examined the measurement accuracy of temperature, pressure, and humidity sensors from multirotor drones (Greene et al. 2019; Barbieri et al. 2019), a complete quantification of the thermodynamic measurement accuracy of unshielded sensors has not been previously conducted. Understanding potential biases and the accuracy of thermodynamic measurements from novel drone platforms is

---

<sup>1</sup> This study, titled “Where Should the Sensor Go? An Evaluation of Multirotor Drone Sensor Siting Locations” (Freeman, S.W., J. Bukowski, L.D. Grant, P.J. Marinescu, J.M. Park, S.M. Hitchcock, and S.C. van den Heever, 2022) is to be submitted to the Journal of Atmospheric and Oceanic Technology

critical for their use in measurements of convective boundary layers. Therefore, the first goal of this dissertation is to:

- (1) *Evaluate the errors and biases induced by a multirotor drone on measurements of pressure, temperature, and humidity in the boundary layer.*

In Chapter 3<sup>2</sup> of this dissertation, enhancements to a cloud object tracking tool used for identifying, tracking, and segmenting convective clouds and other atmospheric phenomena is presented. As both model and observational datasets continue to grow, tools for automatically tracking convective clouds and their environments are required. However, many existing tracking tools are only able to be used with one kind of atmospheric phenomena (e.g., Núñez Ocasio et al. 2020), or one kind of variable (Dixon and Weiner 1993). Data on convective clouds and other atmospheric phenomena are produced from a variety of different sources, such as satellites, radars, and numerical models. Tracking the same phenomenon in multiple different data sources should not require multiple different algorithms, as such approaches can produce mismatches and hence different results owing to their differing methodologies. The Tracking and Object-Based Analysis of Clouds (*tobac*; Heikenfeld et al. 2019) package resolves this issue, allowing users to track any atmospheric phenomenon with any variable on any grid. *tobac*'s variable- and grid-agnostic capabilities sets it apart from all other tracking algorithms commonly used in atmospheric science, but the original (v1.2) version of *tobac* is computationally slow and can only track in two spatial dimensions. As convective cloud datasets continue to grow, the

---

<sup>2</sup> This study, titled “*tobac* v1.5: Introducing Fast 3D Tracking, Splits and Mergers, and Other Enhancements for Identifying Meteorological Phenomena” (Sokolowsky, G.A.\* , S.W. Freeman\*, W.K. Jones, J. Kukulies, F. Senf, P.J. Marinescu, M. Heikenfeld, K. Brunner, E.C. Bruning, S.M. Collis, R.C. Jackson, G.R. Leung, B. Raut, S.M. Saleeby, P. Stier, S.C. van den Heever, 2022; \*these authors contributed equally to this work) is to be submitted to Geoscientific Model Development

ability to identify and track millions of convective clouds rapidly and in three dimensions is necessary to quantify convective cloud properties and processes, how they evolve over storm lifecycles, and the environments that create them. Hence, the second goal of this dissertation is to:

*(2) Enhance the ability to identify, track, and segment convective cloud properties and processes and their environments.*

In Chapter 4<sup>3</sup>, we explore how the dynamic and thermodynamic environment influences the properties of the two deeper convective cloud modes in the tropics: congestus and cumulonimbus clouds (Johnson et al. 1999). Obtaining robust environment – cloud relationships requires a large database of both convective cloud properties and their environments. To build this database of clouds, a novel long-duration, high-resolution, large-area numerical model simulation (termed “basin-scale simulation”) is conducted. The *tobac* tracking package, described in Chapter 3, is used to track nearly 200,000 individual clouds throughout their entire lifecycle to build a substantial database of convective clouds and their environments. Using this database, three environmental properties of convective clouds were examined: convective cloud intensity (both precipitation intensity and vertical velocity intensity), convective cloud organization, and the linearity of organized convective systems. Understanding how the basic properties of convective environments influence these three key cloud properties is the first step towards building a unified theory on how convective clouds influence their environment. Therefore, the third goal of this dissertation is to:

---

<sup>3</sup> This study, titled “Dynamic and Thermodynamic Environmental Modulation of Tropical Congestus and Cumulonimbus in the Maritime Continent” (Freeman, S.W., D.J. Posselt, J.S. Reid, S.C. van den Heever, 2022, accepted pending revision) is accepted pending revision at the Journal of the Atmospheric Sciences

*(3) Elucidate the relationships between convective cloud intensity, organization, and morphology and the thermodynamic and dynamic environmental properties of the tropical atmosphere*

Finally, in Chapter 5<sup>4</sup> of this dissertation, an analysis of how the aerosol environment influences convective cloud precipitation in the tropics is presented. As discussed in Section 1.2 above, the concentration of aerosol particles in the atmosphere can have impacts on clouds and precipitation from changing cloud properties directly and from influencing the broader convective environments indirectly. Expanding on the basin-scale methodology introduced in Chapter 4, two additional basin-scale numerical experiments with *tobac*-enabled tracking are conducted, in which only the concentration of aerosol particles in the atmosphere is varied. This experimental design allows for an examination of how aerosol particles alone influence convective properties on both a storm- and scene-scale. Hence, the fourth goal of this dissertation is to:

*(4) Examine the relationship between aerosol particles and the precipitation produced by the congestus and cumulonimbus modes of tropical convection on both a cloud- and scene-level.*

In Chapter 6, a summary of this dissertation research, a discussion of the findings, and the implications of this work are presented. Impacts on future missions examining convective environments, such as the upcoming INvestigation of Convective UpdraftS (INCUS) and Atmosphere Observing System (AOS) satellites are discussed, and opportunities for future model-observational research are examined.

---

<sup>4</sup> This study, titled “Aerosol-induced Enhancement of Congestus and Suppression of Cumulonimbus Clouds in the Tropics” (Freeman, S.W. and S.C. van den Heever, 2022, in preparation) is in preparation for Geophysical Research Letters

## CHAPTER 2: WHERE SHOULD THE SENSOR GO? AN EVALUATION OF MULTIROTOR DRONE SENSOR SITING LOCATIONS

### 2.1. Introduction

Small drones (hereafter referred to as drones; also known as small Uncrewed Aerial Systems [sUAS or UAS] or small Uncrewed Aerial Vehicles [sUAV or UAV]) have been used for atmospheric science research since as early as 1956 (Vorontsov et al. 1958; Humphrey 1961). Until the 2010s, the drones utilized were exclusively fixed-wing drones (e.g., Schafer et al. 2001; Houston et al. 2011; Elston et al. 2014; Riganti and Houston 2017). Multirotor drones were then introduced into atmospheric science research and have since increased in popularity (e.g., Brady et al. 2016; Lee et al. 2017; Geerts et al. 2017, 2018; Vömel et al. 2018). This enhanced popularity of multirotor drones is due in part to their ability to take off and land vertically, their ability to hover, their low cost, and their relative ease to fly.

A wide body of research has investigated the accuracy of measurements made on fixed-wing drones, including thermodynamic variables (e.g., Spiess et al. 2007; Houston et al. 2016) and winds (e.g., Shuqing et al. 1999; van den Kroonenberg et al. 2008). However, relatively less work has examined the accuracy of thermodynamic measurements made from multirotor drones as compared to fixed-wing drones. This is in spite of the fact that multirotor drones have complex aerodynamic interactions caused by their multiple propellers operating at different speeds close to each other (Yoon et al. 2016) which can be expected to impact the measurements being made.

Although the accuracy and precision of measurements made aboard multirotor drones are not yet well characterized, several field campaigns have already employed multirotor drones to

measure thermodynamic variables. These campaigns include the Colorado State University Convective CLOUD Outflows and UpDrafts Experiment (C<sup>3</sup>LOUD-Ex; van den Heever et al. 2021); the Verification of the Origins of Rotation in Tornadoes EXperiment-SouthEast (VORTEX-SE; <https://www.nssl.noaa.gov/projects/vortexse/>; Lee et al. 2017; Lee et al. 2019); the Lower Atmospheric Process Studies at Elevation-a Remotely piloted Aircraft Team Experiment (LAPSE-RATE; Barbieri et al. 2019); and the Land-Atmosphere Feedback Experiment (LAFE; Wulfmeyer et al. 2018; Lee et al. 2019). A thorough characterization of multirotor thermodynamic measurement accuracy is needed to best interpret and results of these recent field campaigns (Koch et al. 2018).

Several recent studies have made some progress in assessing the accuracy of measurements made using multirotor drones. Greene et al. (2018) completed approximately an hour of experiments in which an octocopter drone (a multirotor with eight rotors) was secured to a surface and the rotors were turned on within an insulated indoor chamber. They moved a plastic cylindrical sensor shield containing a hot wire anemometer and a temperature sensor to several under-propeller positions. In these trials Greene et al. (2018) found that the location with the smallest temperature bias was approximately 5-10 cm below the propeller and one third the length of the propeller from the propeller tip (i.e., 1 cm away from the propeller tip for a 3 cm propeller). They argued that this placement allows for aspiration but is sufficiently far from the heat generated by the motor and wingtip vortices. Green et al. (2018) also observed that when the drone's propellers were idle, their temperature measurements were biased between 0.5 and 1 K. They determined that this was due in part to the hot wire anemometer, which was located adjacent to their temperature sensor.

Greene et al. (2019) completed a follow-up study to (Greene et al. 2018) by flying a quadcopter (a multicopter with four rotors) next to an Oklahoma Mesonet station. They completed seven flights, totaling approximately an hour of flight time, and examined three siting locations on the quadcopter. They found that solar radiation biased the sensor measurements by up to 0.2 K when the sensors were not properly shielded. They also found that a sensor mounted inside a duct at the front of the quadcopter produced more consistent temperature results than sensors mounted in cylindrical shields underneath the propellers, although they did not statistically compare the drone-based measurements to measurements made from a separate platform. Overall, Greene et al. (2019) recommended siting temperature sensors inside a ducted fan at the center of the drone to ensure sufficient aspiration. The results in Greene et al. (2018) and (2019), which tested different platforms with different sensor siting locations, indicated that more research must be done to better understand the biases and accuracy of drone-based measurements.

While Greene et al. (2018, 2019) examined thermodynamic measurement errors on one drone platform based on sensor placement, Barbieri et al. (2019) investigated measurements made from multiple drone platforms, some with multiple sensors in different places on a single drone. Their study utilized intercomparison data from the LAPSE-RATE field campaign, which employed 35 different fixed-wing and multicopter drones. Their drone-measured temperature, pressure, relative humidity, and wind measurements were compared to measurements from a nearby instrumented tower. In these tests they found that the mean value differences in the thermodynamic measurements made from the drones against the instrumented tower were  $1.6 \pm 2.6$  K in temperature,  $1.01 \pm 1.16$  hPa in pressure, and  $-3.15 \pm 12.12\%$  in relative humidity. Barbieri et al. (2019) examined the measurements made from a large number of platforms,

sensors, and sensor placements. This approach did not fully characterize the errors from sensor placement. Their work instead characterized the worst-case error possible from measurements made by many drones.

These three previous studies have provided steps toward understanding the errors induced by measuring thermodynamic variables onboard multirotor drones. However, no current work has investigated the accuracy of thermodynamic measurements made from multiple sensor positions aboard a multirotor while in flight and compared those measurements to observations recorded with identical sensors mounted to platforms other than drones. The work that is described here compares eight different sensor positions of drone-based temperature, pressure, and dewpoint temperature measurements to those made using tethered instruments located sufficiently far away from the direct influence of the drone's propellers. Our goal is to analyze the errors induced by the multirotor itself in the measurements of each of these fundamental atmospheric variables. Further, in investigating these errors, we aim to provide already-completed field campaigns such as C<sup>3</sup>LOUD-Ex, LAFE, and others with a robust characterization of drone-based thermodynamic measurement errors. Finally, we include recommendations for sensor placement for future field campaigns that employ multirotor drones.

## **2.2 Methodology**

To assess the accuracy of thermodynamic measurements made from multirotor drones, a comprehensive experiment suite using a hexacopter drone (a multirotor with six rotors) was designed. The experiments included 82 outdoor flights, 9 of which were flown at night, and were conducted adjacent to an instrumented tethered balloon (hereafter tethered sonde). The flights were conducted from October 2018 to January 2019 and provided approximately 12.5 hours of total

sampling time. During each test flight eight different sensor siting locations onboard the multirotor were compared to the measurements taken on board the tetheredsonde.

#### *a. Drone and Sensor Setup*

The DJI Matrice 600 Pro (SZ DJI Technology Co., Ltd., Shenzhen, China) hexacopter is employed in these experiments. The Matrice 600 Pro, pictured in Figure 2.1a and 1b, has been used in atmospheric science field campaigns and published literature (e.g., Islam et al. 2019; van den Heever et al. 2019). The Matrice 600 Pro is powered by six batteries positioned at the center of the drone platform, which is also the location of the avionics and flight computers. Six arms extend radially from the center, and each arm contains an independently spinning motor and an attached 53 cm propeller. The drone dimensions are 1.668 m x 1.518 m x 0.727 m when in takeoff and landing configuration. After takeoff, the drone switches to cruise configuration and its landing legs fold upwards to the sides, reducing the height of the drone (Figure 2.1a). The legs remain retracted until the drone is configured for landing.

The International Met Systems iMet XQ (Grand Rapids, MI, USA) sensor is used to make the thermodynamic measurements for this work. This particular sensor (Figure 2.1c) has been previously used to make thermodynamic measurements from multirotor drones (e.g., Hemingway et al. 2017; Themistocleous 2017; Dexheimer et al. 2018; Lee et al. 2019; van den Heever et al. 2019). The iMet XQ measures pressure, temperature, and humidity at 1 Hz. The specifications and sensor technologies of these measurements are detailed in Table 2.1. The humidity sensor reports relative humidity rather than an absolute measure of humidity and has a separate temperature sensor that can be used for more accurate conversions between humidity variables. To analyze the humidity for this research, the relative humidity values that are recorded by the sensors are converted to dewpoint temperature, an absolute value of atmospheric

moisture, using the temperature from the humidity sensors. The conversion from the native relative humidity values to dewpoint temperature is performed to eliminate the impacts of temperature bias on the relative humidity sensors, as relative humidity relies on accurate measurements of both temperature and moisture. Nine of the 12 sensors employed in these tests save the temperature of the humidity sensor in addition to the other three variables, while three of the older sensors do not report the humidity sensor's temperature and are therefore excluded from the analysis of humidity. This should not bias the results because between each flight experiment each of the sensors was progressively moved from one location to the next. None of the sensors used in these experiments has a shield covering the temperature or humidity sensor, although the temperature sensor's reflective coating helps mitigate the radiation error during daytime flights.

To examine the impacts that different sensor placements have on thermodynamic measurements, eight different sensor sites onboard the drone are chosen for these experiments. The sensor sites are shown in Figure 2.1a and b. These eight different sensor sites represent what we believe are the most common and/or logical locations for sensors onboard multirotor drones. Two of the positions, *CWProp* and *CCWProp* (CW for a ClockWise rotating propeller and CCW for a CounterClockWise rotating propeller) are approximately 2 cm underneath the propellers and 5.5 cm inside the tip of the propeller when the propeller and arm are parallel. This distance is located away from the propeller tip by approximately 1/3 of the length of the propeller (8.8 cm on this platform), as recommended by Greene et al. (2018). The *Top* and *OverBatt* positions are situated on top of the drone. *Top* is located at the highest point atop the avionics bay but below the three upward pointing GPS antennae, and the *OverBatt* position is located on top of a battery bay with the temperature sensor extended away from the central portion of the drone by

approximately 2 cm. A similar placement to the *OverBatt* position was also used by Lee et al. (2019). One of the landing legs of the aircraft contain two positions, *TopLeg* and *BotLeg*, which are approximately 8 cm below one of the drone arms when in cruise configuration (Figure 2.1a). The *TopShelf* and *BotShelf* positions are on platforms mounted below the main electronics bay by approximately 7 and 15 cm, respectively. The *TopShelf* position was used to house the thermodynamic sensors during the C<sup>3</sup>LOUD-Ex field campaign.

#### *b. Drone and Sensor Setup*

To identify the drone-induced errors of the eight examined positions, the drone is flown adjacent to a tethersonde. The tethersonde is anchored in dead scrubland at the now-retired Christman Field Airport (hereafter Christman Field) in Fort Collins, CO. The anchor point of the tethersonde is at least 50 m from roads, fences, and other objects that could inadvertently influence the observations. The tethersonde is initially raised to a height of at least 50 m above the surface during the day and 30 m at night using a rope, but it is allowed to change its horizontal and vertical position with the wind. The altitude for the tethersonde is chosen to be high enough such as to be above the surface layer but low enough to reduce needed battery to climb and maneuver and allow more sampling time on a single battery set.

The tethersonde instrumentation is mounted approximately 50 cm below the base of the balloon. This instrumentation consists of an International Met Systems iMet-1 radiosonde with an iMet XQ sensor of the same type as that on board the drone (Figure 2.1d). Although both the iMet-1 radiosonde and iMet XQ record GPS and thermodynamic variables, the GPS from the iMet-1 radiosonde is used as the tethersonde's location value because the iMet XQ's GPS antenna is directed at the surface, causing degraded accuracy. On the other hand, the iMet XQ is used for the thermodynamic measurements to remove any error that may potentially be caused

by differences in instrument technology between the iMet XQ and the iMet-1 radiosonde. The tethered sonde is launched at the beginning of each flight day and allowed to remain airborne for the entire duration of the flights held on any one day. The tethered sonde is, however, occasionally raised or lowered in order to avoid interference with manned aircraft traffic or to change the attached iMet XQ sensor halfway through the flight day as part of the iMetXQ drone sensor rotations. The iMet XQ sensors aboard the tethered sonde are included in the rotations of the sensors aboard the drone; most sensors used on the drone are also on the tethered sonde for at least a few flights. It should be noted that as for the sensors aboard the drone, the iMet XQ aboard the tethered sonde is not shielded and instead has a reflective coating on the temperature sensor. While we recognize that this adds another possible source of error to the daytime flights in association with solar radiation, we have treated the measurements made from the tethered sonde's iMetXQ sensor as truth for this study as they are not subject to the airflow and perturbations induced by the drone.

The drone takeoff and landing position is located 20 m east of the tethered sonde anchor point. After takeoff, the drone is flown directly upwards until the altitudes of both the tethered sonde and the drone are within a few meters of one other. Despite this initial check, the tethered sonde is on average 9.13 m higher than the drone for the 82 flights in this study (9.71 m during the day flights and 4.2 m for the night flights). This mean altitude bias does not substantially affect the thermodynamic errors measured. When comparing only the data when the drone was higher than the tethered sonde, the thermodynamic measurement errors are similar (not shown). The drone is oriented such that the front of the drone (the angle of the drone shown in Figure 2.1a) faces due south. While the tethered sonde's horizontal position and altitude is allowed

to vary in flight with the changing winds, the drone's position is fixed in space for each of the 82 flights using the drone's autopilot function.

Each of the flights has at least nine consecutive minutes of sampling time, not including the additional flight time necessary for takeoff, setup, and landing. After each flight, the sensors attached to each of the positions on the drone are rotated, with each sensor aboard the drone being sequentially moved to a different position. The sensor rotation is performed to remove any potential bias caused by a specific sensor-position combination. While the sensors aboard the drone are rotated after each flight, the sensor aboard the tethersonde is only changed either between flight days or halfway through the flights on a given day. The sensor on board the tethersonde each day is drawn from the set of sensors used in the drone rotations and is rotated between the tethersonde and the drone between flight days.

### *c. Sampling Conditions*

The 82 flights are conducted at Christman Field in a variety of nonprecipitating meteorological conditions, which are sampled by the co-located Christman Field weather station (hereafter surface weather station) (Figure 2.2). The range of observed pressure (Figure 2.2c) is limited to between 830 and 855 hPa due to the site's elevation (1573 m above sea level). Like the pressure, the moisture conditions observed (Figure 2.2b) are also bounded due to the dry climate in Colorado. The experiments are performed primarily in low wind conditions, as is evident from the distribution of sustained wind (Figure 2.2e) and gusts (Figure 2.2f). Low wind conditions are necessary to limit the motion of the tethersonde, and thus its altitude variability with respect to the drone. The wide range of thermodynamic and solar radiation (Figure 2.2d) conditions tested in this study significantly extends all of the previous studies described in Section 2.1 by

providing a statistically robust characterization of the errors associated with sampling thermodynamic conditions using multirotor drones.

#### *d. Data Quality Control*

Several steps are taken to quality control both the tethersonde and drone thermodynamic data. First, all twelve iMet XQ sensors employed in this study are placed in an insulated chamber 11 times for between 8 and 72 hours each and calibrated to one another to remove any bias between the sensors. The maximum measured biases between sensors are 0.4 K in temperature, 1 hPa in pressure, and 4% in relative humidity. The measured biases between the sensors for each variable are removed from the data obtained in this study. Next, only those measurements for which the drone's measured altitude is within 30 m (50 m) in the vertical (horizontal) of the tethersonde's measured altitude are used in order to enhance the likelihood that the tethersonde and drone measured air with similar thermodynamic properties. The 30 m vertical threshold is chosen because the nominal accuracy of the GPS aboard the iMet-1 radiosonde is  $\pm 15$  m. The 50 m horizontal threshold is selected because the length scale of boundary layer eddies is proportional to the height above the surface (Arya 2001). We therefore assume that 50 m in the horizontal approximated the width of the eddies at an altitude of 50 m above ground. Analysis reveals that the results of this study are not sensitive to the distance thresholds (not shown). In addition to removing data points where the drone and tethersonde are too far apart, data points are also removed where the iMet-1 or the iMet-XQ aboard the tethersonde record invalid data. No averaging is performed on the data except where described in Section 2.3e.

### **2.3. Results**

For each thermodynamic variable, we examine the differences at each time between the measurements taken aboard the drone and the measurements taken aboard the tethersonde. We

define this difference as the error. The error is comprised of three potential sources: instrument error, drone-induced error, and radiative error. The instrument error is defined as any error caused by fluctuations in the instrument itself other than the calibration biases that have already been corrected. The drone-induced error is any error directly associated with the drone that would not exist if the instrument was mounted to the tethersonde. Possible sources of drone-induced error include heat dissipated by the drone motors, avionics, and batteries, and airflow perturbations induced by the rapidly spinning rotors and their associated vortices. The radiative error component is defined as any error resulting from the effects of solar radiation, including heating of the sensor itself by the sun, heating of the surface of the drone below the sensor, or any other error that does not exist at night.

The results from the 82 flights are discussed separately for each thermodynamic variable. Temperature is further stratified into daytime (73 flights) and nighttime (9 flights) results. A night flight is defined as any flight completed after nautical twilight and where  $0.0 \text{ W m}^{-2}$  insolation is measured by the surface weather station.

#### *a. Daytime Temperature*

The temperature error, defined as the temperature measured by the tethersonde subtracted from the temperature measured by the drone at each time, is calculated separately for each sensor position (i.e.,  $T_{\text{drone, sensor location}} - T_{\text{tethersonde}}$ ; where  $T$  is the temperature in K). The temperature error for each sensor location on the drone is shown in Figure 2.3 for the 73 daytime flights (a total of approximately 40,000 individual temperature observations for each sensor position). The mean errors between the drone and tethersonde are less than  $\pm 0.42 \text{ K}$  for all eight tested siting locations, although the spread between the 2.5<sup>th</sup> and 97.5<sup>th</sup> percentiles reaches 2.79 K, with the largest spread being  $-0.91 \text{ K} \leq T \leq +1.88 \text{ K}$  for *TopShelf* (Figure 2.3). The *BotLeg*

position, which is approximately 8 cm below the propeller and is shielded from the direct downward air forced from the propeller by the leg it is mounted to, has the smallest magnitude mean error (-0.07 K). This is in contrast to *TopLeg*, which has the largest magnitude mean error (+0.42 K) despite it being located only ~10 cm horizontally from the *BotLeg* position.

One can categorize the eight sensors shown in Figure 2.3a into two main groups: those sensors that have a cold mean bias and lower error standard deviations (*BotLeg*, *CCWProp*, *CWProp*, *OverBatt*, *Top*), and those positions that have a warm mean bias and higher error standard deviations (*BotShelf*, *TopLeg*, *TopShelf*). These differences can be seen more clearly in Figure 2.3b-i, which show histograms of the errors for each of the eight sensor positions. The three sensor positions with the warm mean bias and higher errors (Figure 2.3c, h, and i) can generally be characterized as non-normal distributions that are skewed towards warmer temperatures relative to the tethersonde data. In contrast, the remaining positions (Figure 2.3b,d-g) are similarly non-normal, but have smaller error standard deviations and negative tails, which indicates a large cold bias relative to the tethersonde. The situations in which this occurs will be explored below.

We now assess the three components of error (instrument, drone, and radiation) to understand the causes of the mean temperature errors. The substantial sampling time during daytime (11 hours; ~200,000 data points total) in this study and the fact that instrument errors are typically symmetric around zero after being corrected for any mean bias, means that the instrument errors are largely mitigated and thus play a trivial role in the mean thermodynamic errors. Therefore, the mean observation errors are primarily caused by drone-induced errors, radiative errors, or both.

To better characterize the radiative error present during the daytime flights, the flights are stratified by the average solar radiation that is observed at the surface weather station (Figure 2.4). Each of the solar radiation bins shown in Figure 2.4 contains between eight and ten flights. With increasing insolation, the median bias generally becomes colder for those sensors receiving a large amount of aspiration (*BotLeg, CCWProp, CWProp, OverBattery, Top*). For those sensors receiving less aspiration (*BotShelf, TopLeg, TopShelf*), the mean bias typically becomes warmer with more insolation (*BotShelf, TopLeg*) and/or the error bars become substantially larger (*TopLeg, TopShelf*). The reason for these opposite trends appears to be twofold: (1) the reflective coating onboard the iMet sensors is likely inadequate to reflect all of the incoming solar energy; and (2) since the tethersonde does not receive forced aspiration unlike the drone which receives some from the propellers, the temperature measured on the tethersonde might be biased warm relative to the true environmental temperature, thus leading to a *perceived* cold bias on the drone for the five positions receiving more aspiration. Figure 2.4 further shows that the spread of the error generally increases with increasing solar radiation for all sensor positions. This suggests that simply placing sensors underneath propellers may not be sufficient to counteract the solar radiative error. Rather, Figure 2.4 suggests that efforts to properly shield sensors could be worthwhile. However, such shields can block ambient airflow, including airflow produced by the drone, thereby reducing sensor aspiration. Such effects should therefore be taken into consideration when designing sensor shields. The impacts of radiative error on the mean thermodynamic errors and how we can separate this source of error from drone-induced error will be further examined in Section 2.3b below.

The temperature results demonstrate that for the worst-case scenario for any single temperature measurement made during the daytime that the accuracy at a 95% confidence

interval (hereafter CI) has a range of  $-1.34 \text{ K} \leq T \leq +1.88 \text{ K}$  when not removing the mean biases (Figure 2.3b-i). The sensor position with the narrowest CI is *BotLeg*, which had a 95% CI of  $-0.75 \text{ K} \leq T \leq +0.65 \text{ K}$ . Section 2.3e contains an analysis of the errors when measurements of temperature gradients are sought instead of measurements of absolute temperature values, and the implications of the accuracy measures elucidated in this work for field campaigns will be discussed in Section 2.4.

### *b. Nighttime Temperature*

Nighttime flights were conducted to understand the effects of radiative error and to separate the radiative error from the drone-induced error. Figure 2.5 shows the analyses of temperature using only the 9 nighttime flights (approximately 1.5 total flight hours). The errors in measured temperature are notably smaller at night than during the day. The largest mean bias in temperature decreases from 0.42 K during the day to 0.24 K at night, and the largest 95% CI range decreases from 2.75 K to 1.5 K. This indicates that radiative errors, either due to the heating of the sensor itself or as a result of heating the drone body, are substantial contributors to the total errors observed in the daytime flights.

Recall that for the daytime flights, the various drone sensor positions either have a warm or cold mean bias depending on the amount of aspiration they received. In contrast, at night, all eight tested positions have a warm bias (Figure 2.5), and the magnitude of the warm bias ranges from +0.05 K to +0.24 K. This could be due to a combination of two factors: the mean altitude bias between the drone and tether sonde (4.2 m) and the heat generated by the drone. However, a 4.2 m mean altitude bias is unlikely to result in a warm bias on the order of 0.1 K. Even if a dry-adiabatic lapse rate is assumed in the near-surface boundary layer (an unrealistically strong lapse rate at night), a 4.2 m altitude difference only translates to a mean bias of +0.04 K. We therefore

speculate that the primary cause of the temperature bias is that the drone, unlike the tethered drone, is a significant source of heating. The batteries' onboard temperature sensors indicate that each battery can increase its temperature by up to 25 K while in flight. The *TopShelf* position has the highest mean bias, which is likely due to its position directly below the main electronics and battery bay. The *BotLeg* has the lowest mean bias, similar to the daytime temperature results. The small bias for the *BotLeg* position is once again likely because this sensor position is farthest from the main electronics bay and motors. Even the two positions that are located directly below the propellers (*CWProp* and *CCWProp*), which should receive the most aspiration among the sensor positions, have warm biases at night. The warm biases for the under-propeller positions are likely due to the heat generated by the motors in flight or by the propellers circulating air warmed over the main body of the drone to these positions. Overall, the nighttime flight results demonstrate that even if sensors are properly shielded from radiation error during the day that drone-induced errors are present and must be accounted for during daytime and nighttime flights.

When comparing the nighttime distributions of error (Figure 2.5b-i) to those of the daytime position errors (Figure 2.3b-i), the nighttime distributions are narrower (Figure 2.5b-i). For the nighttime flights, the 95% CI of all the sensor siting locations is at worst  $-0.31 \text{ K} \leq T \leq +0.82 \text{ K}$  when not adjusting for the mean bias, a substantial improvement on the  $-1.34 \text{ K} \leq T \leq +1.88 \text{ K}$  analyzed from the daytime flights. Although these data are not normally distributed, the smaller tails and narrower distributions characteristic of the nighttime flights suggest that shielding the temperature sensor aboard the drone will improve data quality and reduce error for the daytime measurements for all the sensor siting locations tested.

### c. Pressure

All 82 flights are analyzed together for the pressure analyses as there is no substantive difference between daytime and nighttime pressure errors (not shown). The drone errors for all eight sensor locations have a negative pressure bias (Figure 2.6). The low-pressure bias on the drone occurs despite the drone being lower in altitude than the tether sonde by 9.13 m on average (see Section 2.2b). This suggests that there is some amount of drone-induced error that leads to the observed consistent negative pressure bias. We speculate that this negative pressure bias may be induced by the complicated aerodynamic interactions discussed in Section 2.1. However, a study that can model these complex interactions on our platform, similar to that of Yoon et al. (2016), would be required to confirm this hypothesis. All eight positions have similar error standard deviations and mean biases (Figure 2.6). The 95% CIs are all within  $-2.0 \text{ hPa} \leq P \leq +0.9 \text{ hPa}$  for a single independent measurement.

Unlike the temperature error distributions, the error distributions for pressure are multimodal for most siting locations (Figure 2.6b-i). The multimodal distributions are particularly evident in the *BotLeg*, *BotShelf*, and *TopLeg* positions, which are all bimodal. To understand this bimodality, we stratify the pressure errors for all sensor positions into strong and weak wind flights. Strong wind flights are defined as flights during which the surface weather station reports an average 5-minute gust greater than  $3 \text{ m s}^{-1}$  during the sampling period. Approximately half of the flights are classified as strong wind flights and half as weak wind flights. The results for one position (*BotShelf*) demonstrate that the bimodal distribution is primarily caused by the 39 flights with stronger wind gusts (Figure 2.7b). The 43 flights classified as having weak surface winds more closely approximate a unimodal distribution (Figure 2.7a).

Although it is not possible to determine the reason for the pressure error bimodality during the high wind gust events using the data collected here, we speculate that it is caused either by the motion of the tether sonde or by unequal dynamic pressure perturbations on the drone due to its complex aerodynamics (Yoon et al. 2016). Since the tether sonde is not rigidly tethered to the ground and is instead secured with a string, the tether sonde tilts downwind as the horizontal winds increase, lowering its altitude. If the wind changes speed or direction, the tether sonde's altitude quickly changes, but the drone maintains a constant altitude. The tether sonde, therefore, oscillates between being higher and lower than the drone in high wind events, which could explain the observed bimodal structure. Using the Hypsometric equation and typical values for the temperature and pressure during this study, the expected change in pressure is 1 hPa for a 10 m change in height. This is approximately the magnitude of the spread in pressure in the bimodal positions, which suggests that the majority of the multimodality may be because of the oscillating tether sonde. However, if this effect accounts for all of the multimodality, all eight sensor positions should have similar bimodal error distributions, which is not the case (Figure 2.6d,e,i). Instead, the bimodality in the error distribution is most likely caused by multiple factors, including the motion of the tether sonde and the impact of dynamic pressure perturbations from the drone's aerodynamics. In stronger winds, the dynamic pressure force is larger, and this force may be unequally applied to the drone and tether sonde instruments. However, this hypothesis also cannot be confirmed without experiments in a controlled wind environment, experiments utilizing a fixed observational tower, or detailed computer modeling of the airflow around the drone. Since the highest wind speed experienced in this study was  $5.5 \text{ m s}^{-1}$ , it is difficult to predict whether the pressure error will follow similar distributions under even higher

wind situations. More data need to be collected before a more thorough analysis and characterization of the pressure errors can be conducted.

#### *d. Dewpoint Temperature*

As with pressure, the dewpoint temperatures from all 82 flights are analyzed together (Figure 2.8). All sensor positions except *CWProp* have mean bias magnitudes in dewpoint temperature of less than 0.5 K, with three positions having a near-zero mean bias against the tethersonde (*BotLeg*, *TopLeg*, and *TopShelf*; Figure 2.8a). Furthermore, the non-propeller positions (i.e., all but *CWProp* and *CCWProp*) have unimodal distributions with 95% CIs of less than  $\pm 2.75$  K for all but *OverBatt* (Figure 2.8b-i). This is in contrast to the sensor siting locations under the propellers (*CWProp* and *CCWProp*), which have a total 95% CI of  $-1.5 \text{ K} \leq T_d \leq +5.4 \text{ K}$  (Figure 2.8d,e).

The wide 95% CIs of the *CCWProp*, *CWProp*, and *OverBatt* positions merit investigation. In each of these cases (Figure 2.8d-f), the wider CIs are caused by relatively longer tails on the positive side of the distribution (where the drone is moister than the tethersonde), especially for the *CWProp* position. As the drone does not carry any water onboard and does not produce water in flight, the unequal moisture distributions must be a result of error induced either by the drone or by solar radiation.

The 82 flights are stratified by solar radiation (Figure 2.9), as is done in Section 2.3a, to determine the contribution of solar radiation to the dewpoint error. This figure indicates that, generally, the errors (spread and mean bias) in dewpoint temperature decrease with decreasing solar radiation, suggesting that there is some component of radiative error to the total dewpoint temperature error. This is despite the fact that the relative humidity sensor measures the temperature that the relative humidity is based on. We speculate that the radiative error may

result from the relative humidity measurement having a different response time than the temperature measurement on the relative humidity sensor module. If these two parts of the sensor reported their temperature and humidity with different response times, the measured relative humidity may lag behind the temperature measurement, leading to errors when the temperature is rapidly changing, such as in direct sunlight. However, it is impossible to determine the exact cause of the radiative error conclusively with the data collected. Future work should explore this issue further.

#### *e. Temperature and Dewpoint Temperature Gradients*

Some field campaigns that have utilized multirotor drones, such as C<sup>3</sup>LOUD-Ex and LAFE, have been interested in measuring temporal or spatial gradients in the thermodynamic variables rather than in singular measurements of these variables. In this section, we examine the accuracy of the drone measurements when considering temperature or dewpoint temperature gradients in time, where the relative magnitudes, as opposed to the absolute magnitudes are important.

To determine the accuracy of examining temperature or dewpoint temperature gradients instead of singular measurements of temperature or dewpoint temperature, the autocorrelations of the error are first examined. The e-folding time of the error autocorrelation is greater than 1 s for all positions (not shown), which indicates that noise which is present in this error may be eliminated by applying a moving average. We therefore apply a 20-second moving average to the temperature and dewpoint temperature data. This interval is chosen because it is longer than the e-folding times of error autocorrelation for all sensor positions in temperature and most sensor positions in dewpoint temperature (not shown). We specify that only 75% of the data points contained in the moving average window must be valid data points. This requirement

means that for a single 20 s period, there must be 15 valid data points for a moving average to be calculated. If there are fewer than 15 valid data points, the moving average will not be calculated and the point will be set as invalid. These newly filtered data will be notated with an overbar for the remainder of this work (e.g.  $\overline{T}$ ,  $\overline{T_d}$ ).

To characterize the measurement error expected when sampling some  $\frac{\Delta\overline{T}}{\Delta t}$ , where  $t$  is time, an appropriate time interval ( $\Delta t$ ) must first be chosen. We consider time intervals of 9 min (the total time of each flight) or less for this analysis. Increasingly large  $\Delta t$ s reduce the number of useable data points. To provide a compromise between a sufficiently long  $\Delta t$  such that it is larger than the e-folding time and a sufficiently short  $\Delta t$  to allow as large a sample size as possible, a time interval of 60 seconds is chosen. The results are not particularly sensitive to the exact  $\Delta t$  used (not shown). Figure 2.10 shows the results of this analysis, where for each time, the filtered temperature ( $\overline{T}$ ) is subtracted from the temperature 60 seconds later (i.e.  $\overline{T}_{t+60s} - \overline{T}_t$ , notated here as  $\overline{T}_{60s}$ ). It is evident from this figure that when examining the daytime temperature gradients, the errors at each sensor siting location are smaller than the errors in measuring the absolute value of temperature (Figure 2.3), with a worst-case  $\overline{T}_{60s}$  error of (-1.08 K, +1.12 K) at a 95% CI (Figure 2.10). Unlike the absolute measurements of temperature, in  $\overline{T}_{60s}$ , the biases are all near zero. The implications of this accuracy CI for field campaigns are discussed further in Section 2.4.

As shown in Sections 2.3a and 2.3b, the daytime and nighttime temperature accuracies differ due to the impacts of solar radiation. With that in mind, an analysis of  $\overline{T}_{60s}$  error is conducted for the nighttime flights. The 95% confidence error for temperature gradients at night (Figure 2.11) are approximately the same as each independent nighttime temperature

measurement (Figure 2.5). This result suggests that when measuring temperature gradients during the day that the accuracy may differ if there are variations in the incoming solar radiation, such as might ensue from changing cloud properties.

We also have performed an examination of the error when measuring dewpoint temperature gradients. Figure 2.12 shows the error distributions for all eight sensor siting locations for  $\bar{T}_{d,60s}$ . In all eight sensor siting locations, the maximum dewpoint temperature gradient error is  $\pm 2.00$  K at the 95% confidence level, lower than most of the absolute value dewpoint temperature errors. Furthermore, the mean dewpoint temperature gradient error is approximately zero for all sensor positions. Examining temperature and dewpoint temperature gradients is often the goal of field campaigns rather than examining absolute temperature or dewpoint temperature, and the implications of these results will be explored in the next section.

## **2.4. Discussion and Implications for Field Campaigns**

The results presented here characterize the accuracy of thermodynamic measurements made from unshielded sensors in eight different sensor siting locations on one multirotor drone platform. To understand the implications of these findings for the use of drone platforms in field campaigns, two recent campaigns that used unshielded sensors to measure thermodynamics from multirotor drones are now examined. The C<sup>3</sup>LOUD-Ex field campaign (van den Heever et al. 2019) was conducted in July of 2016 and May-June of 2017 and employed a suite of instruments to measure storm updrafts and surface outflows with targeted observations. C<sup>3</sup>LOUD-Ex used six multirotor drones to measure storm-produced cold pools. Cold pools are areas of evaporatively-cooled dense air in contact with the ground that can be identified using gradients in temperature near their edges. The results for temperature and dewpoint temperature gradients outlined in this study (Section 2.3e) are therefore particularly relevant for C<sup>3</sup>LOUD-Ex. The

drones used in C<sup>3</sup>LOUD-Ex were identical to the drone used in the present study, and the C<sup>3</sup>LOUD-Ex drone sensors were placed in the *TopShelf* position. Continental cold pools produced by deep convection, the focus of C<sup>3</sup>LOUD-Ex, typically have near-surface temperature differences ranging from -2 to -20 K relative to the environment (Engerer et al. 2008). The results presented here indicate that  $\bar{T}_{60s}$  errors onboard the drone are at worst  $-1.08 \text{ K} \leq \bar{T}_{60s} \leq +1.12 \text{ K}$  at the 95% confidence level. We therefore conclude that the drone measurements are certainly sufficient to successfully measure most midlatitude continental cold pools produced from deep convection, even without radiation shielding.

The Land-Atmosphere Feedback Experiment (LAFE; Wulfmeyer et al. 2018) was a field campaign completed in August 2017 in central Oklahoma. LAFE used a suite of instruments to observe land-atmosphere feedbacks over different soil types and soil moisture conditions. During LAFE, two multicopter drones with thermodynamic instruments were operated, including at least one drone that had an *in situ* thermodynamic sensor near the *OverBatt* position tested in this work (Wulfmeyer et al. 2018; Lee et al. 2019). The drones were used to measure vertical and horizontal profiles of temperature and humidity over different soil types and soil moisture to identify the spatial structures that may exist in these variables. Lee et al. (2019) reported that during the transects, the temperature varied by  $\pm 0.5 \text{ K}$  and dewpoint temperature varied by approximately  $\pm 1 \text{ K}$ . Our study indicates that the magnitudes of the variance in temperature and dewpoint reported by the LAFE campaign measured by the drones are likely to be real atmospheric features rather than instrument noise at the 90% CI.

The results demonstrated here also elucidate some of the best practices when sampling pressure, temperature, and humidity with multicopter drones. In general, the lowest error spread and mean bias in temperature and humidity were found for the siting location furthest away from

the main body, including the batteries and avionics. For the specific drone used in the present study, the *BotLeg* position best meets these criteria. Future developments in drone sensor engineering should also focus on ways to extend the sensors away from the main body of the drone without substantially increasing the weight or changing the aerodynamic characteristics. For drone platforms where a probe or extension is not possible, measurement errors are likely to be higher due to the heat generated by the drone itself. Even aspiration and shielding may not be sufficient to remove the errors induced by the drone heating, as suggested by the nighttime results presented here. Many test flights should also be completed to better understand the errors and biases when introducing an aspirated shield. For field projects that have already completed their sampling phase with unshielded sensors onboard, the error values that have been characterized in this work should be accounted for when analyzing the data collected.

## **2.5. Conclusions**

Multicopter drones have enabled new types of observational strategies and sampling in field campaigns. This work provides new insights into understanding the measurements made onboard multicopter drones. We have examined temperature, pressure, and humidity measurements made from drones and have characterized the biases and errors induced by placing sensors in different positions on multicopter drones. Eight sensor positions, representing the most common locations utilized in field campaigns to date, were tested by flying a multicopter drone for 82 flights (12.5 total flight hours), including 9 flights at night. The multicopter drone was flown in close proximity to a tethered sonde carrying the same sensors and located at a similar altitude. The measurements of temperature, pressure, and dewpoint temperature at each of the sensor siting locations were compared with the measurements from the tethered sonde, where the latter observations were

assumed to represent ground truth. The errors were defined as the difference between the drone sensor measurements and the tethered sonde measurements.

The results from the observational experiments indicate that when sampling temperature during the day using a sensor unshielded from incoming solar radiation, measurement errors range from  $-0.83 \text{ K} \leq T \leq +0.61 \text{ K}$  to  $-0.91 \text{ K} \leq T \leq +1.88 \text{ K}$  at a 95% confidence level. When making measurements at night without incoming solar radiation impacts, the temperature error is reduced to  $-0.31 \text{ K} \leq T \leq +0.82 \text{ K}$ . However, at night, there is still a warm mean bias in temperature due to the heat generated by the battery and avionics onboard the drone. If one is measuring temperature gradients where the difference between point measurements is of interest rather than single point temperature measurements, the expected 95% confidence interval (CI) for daytime temperature gradient errors after filtering the data range from  $-0.57 \text{ K} \leq T \leq +0.63 \text{ K}$  to  $-1.08 \text{ K} \leq T \leq +1.12 \text{ K}$ , depending on sensor location.

Our analysis of dewpoint temperature indicates that solar radiative error impacts the dewpoint temperature measurements made onboard the drone because the reported accuracies vary when stratified by solar radiation. The largest error in dewpoint temperature was found to be  $\pm 2.75 \text{ K}$ , except for the sensor position below the two propellers and the position directly over a battery where the largest 95% CI was  $-1.5 \text{ K} \leq T_d \leq +5.4 \text{ K}$ . The error when sampling a dewpoint *gradient* had a 95% CI of approximately  $\pm 2.00 \text{ K}$ , regardless of sensor position. Although the errors associated with measuring pressure were investigated in this study, they were found to depend on the ambient wind speed. Future work should therefore examine this dependence if errors in the pressure measurements are to be better identified.

Our results place a much narrower CI on thermodynamic measurements made from drones than those presented by Barbieri et al. (2019). This is most likely because we were focused on

the results from one drone platform rather than an ensemble of different drones. In field campaigns where multiple drones of different types are to be deployed, understanding the differences in drone-induced errors between platforms would be critical. The results presented here suggest that the error bounds for drone thermodynamic measurements can be greatly reduced by placing the sensor in certain positions and conducting many error characterization flights for each drone platform used.

Future work should consider examining the impact of sensor shielding on measurement errors, the measurement errors for different types of drone platforms, and the pressure errors in stronger wind conditions than those examined here. Our analysis of the nighttime flights conducted in order to eliminate the impacts associated with solar radiative error suggest that shielding may not entirely eliminate errors in temperature measurements because heat from the drone batteries and avionics can bias the measurements. The biases in shielded sensors should therefore be investigated before shielding is employed in future campaigns. Additionally, errors associated with measurements onboard a smaller drone platform may not be identical to the errors on our larger platform because different drone platforms produce varying amounts of heat. Finally, this research provides characterizations of measurement errors based on sensor siting locations that are useful to already-completed field campaigns. We suggest that in future campaigns employing drones for thermodynamic measurements, thermodynamic sensors should be sited as far away from the main body of the drone (and hence the batteries and avionics) as possible and should be shielded from the impacts of insolation.

## 2.6. Tables and Figures

Table 2.1: Specifications of the iMet XQ sensor as reported by International Met Systems (International Met Systems 2018).

Variable	Technology	iMet Reported Accuracy	iMet Reported Resolution	iMet Reported Response Time
Temperature	Glass Bead Thermistor	$\pm 0.3$ K	0.01 K	2 s
Pressure	Piezoresistive	$\pm 1.5$ hPa	0.02 hPa	10 ms
Relative Humidity	Capacitive	$\pm 5\%$	0.7%	5 s with $1 \text{ m s}^{-1}$ flow

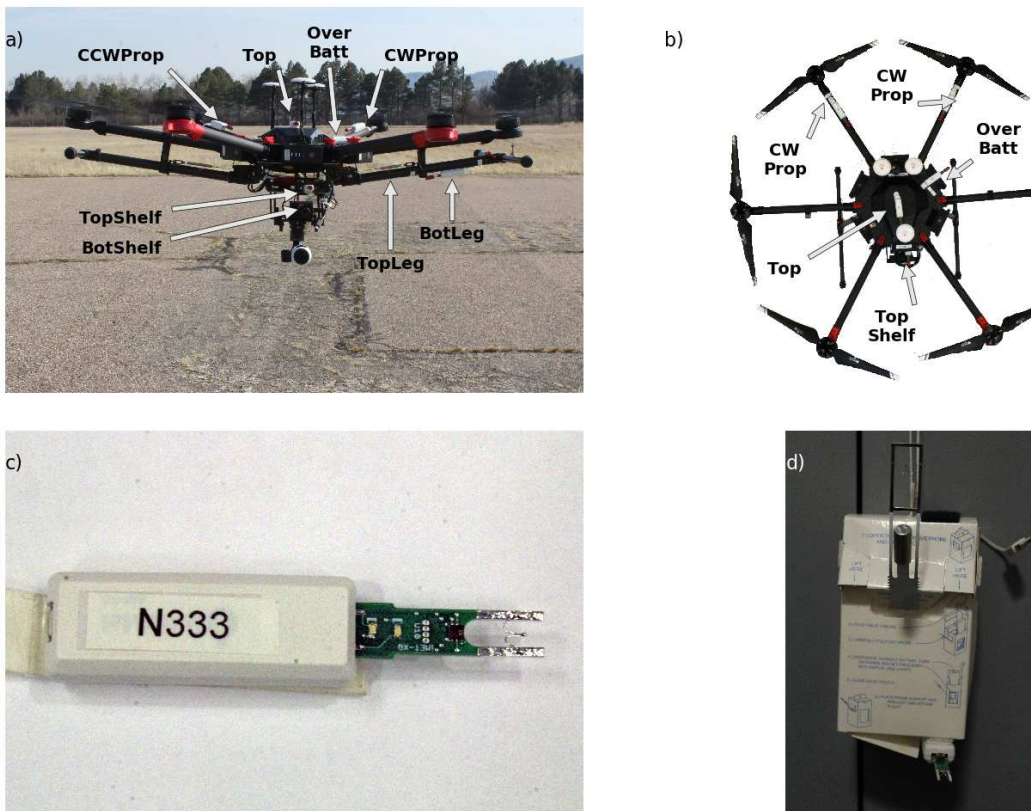


Figure 2.1: (a) Front-view picture of the DJI Matrice 600 Pro drone in flight with the legs folded up. The 8 sensor positions are labeled. (b) Top-down photo of the drone with the legs down; the

positions of all visible sensors are labeled. (c) Photograph of an iMet XQ sensor. (d) Photograph of the iMet-1 radiosonde with an iMet XQ sensor attached to the bottom.

### Christman Field Average Weather during Flights

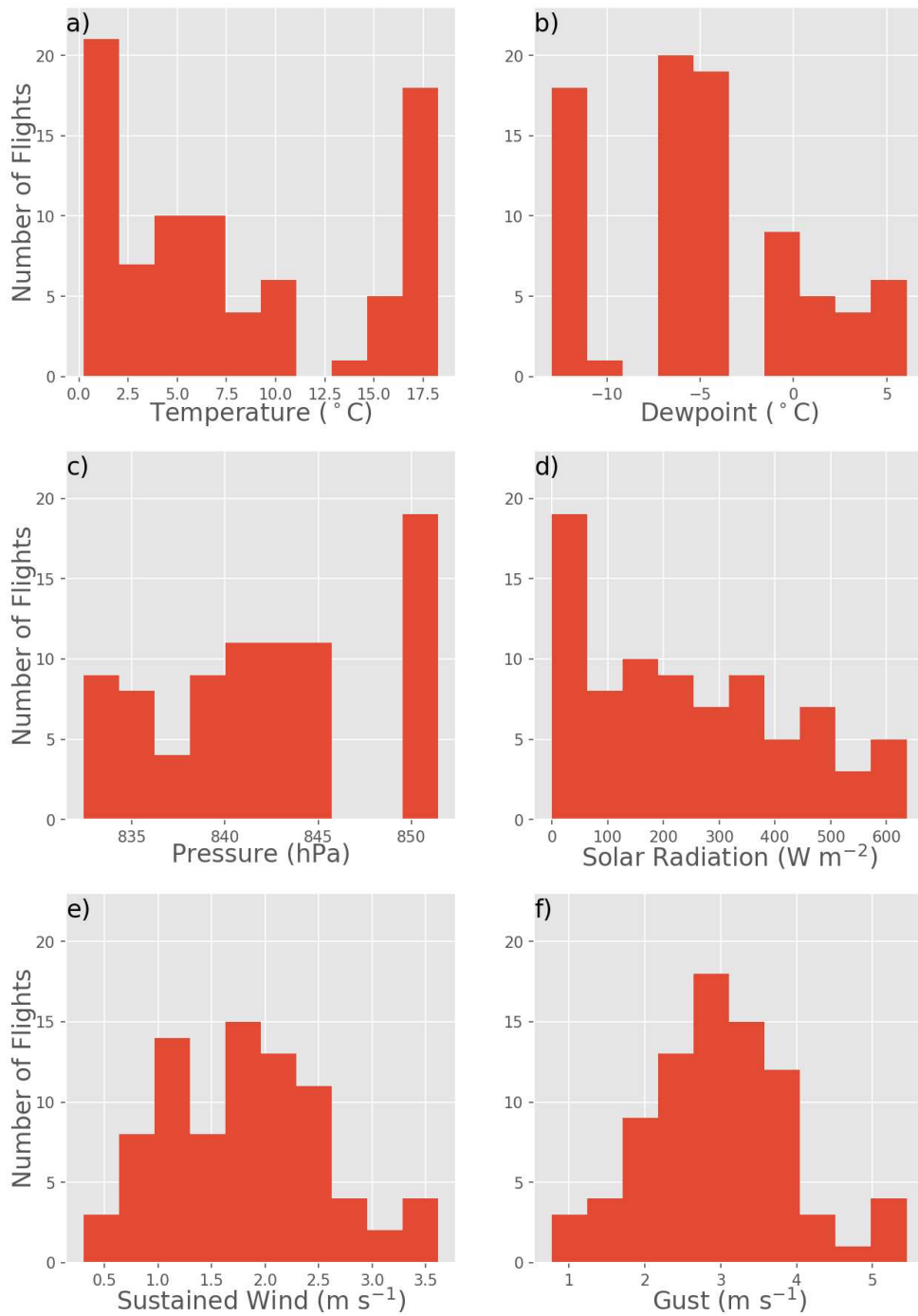


Figure 2.2: Histograms of conditions, averaged over the duration of each flight, observed by the surface weather station during all flights. Shown are surface (a) temperature, (b) dewpoint temperature, (c) pressure, (d) solar radiation, (e) sustained wind speed, and (f) wind gust.

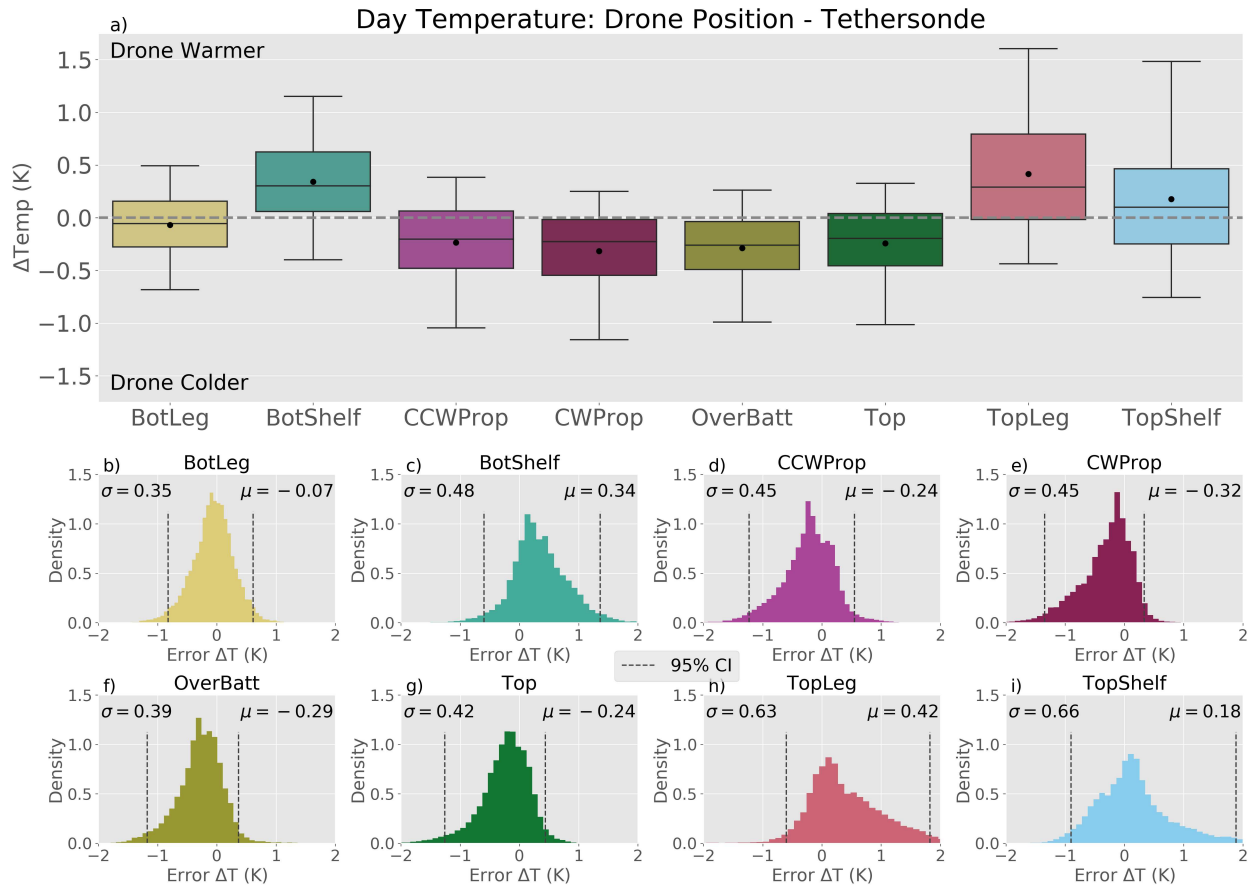


Figure 2.3: (a) Box plots of the drone sensor temperature minus the tethersonde sensor temperature, i.e. the “errors” (positive values indicate that the drone is warmer than the tethersonde), for all daytime flights. The box outlines denote the 25th, 50th, and 75th percentiles, whiskers extend to the 5th and 95th percentiles, and the dots indicate the distribution means. (b-i) Density histograms of the daytime flight temperature errors for each individual drone sensor as labeled on each panel. The 2.5<sup>th</sup> and 97.5<sup>th</sup> percentiles are marked with dashed vertical black lines to indicate the 95% confidence interval. The error standard deviation ( $\sigma$ ) and mean error ( $\mu$ ) are labeled at the top of each panel.

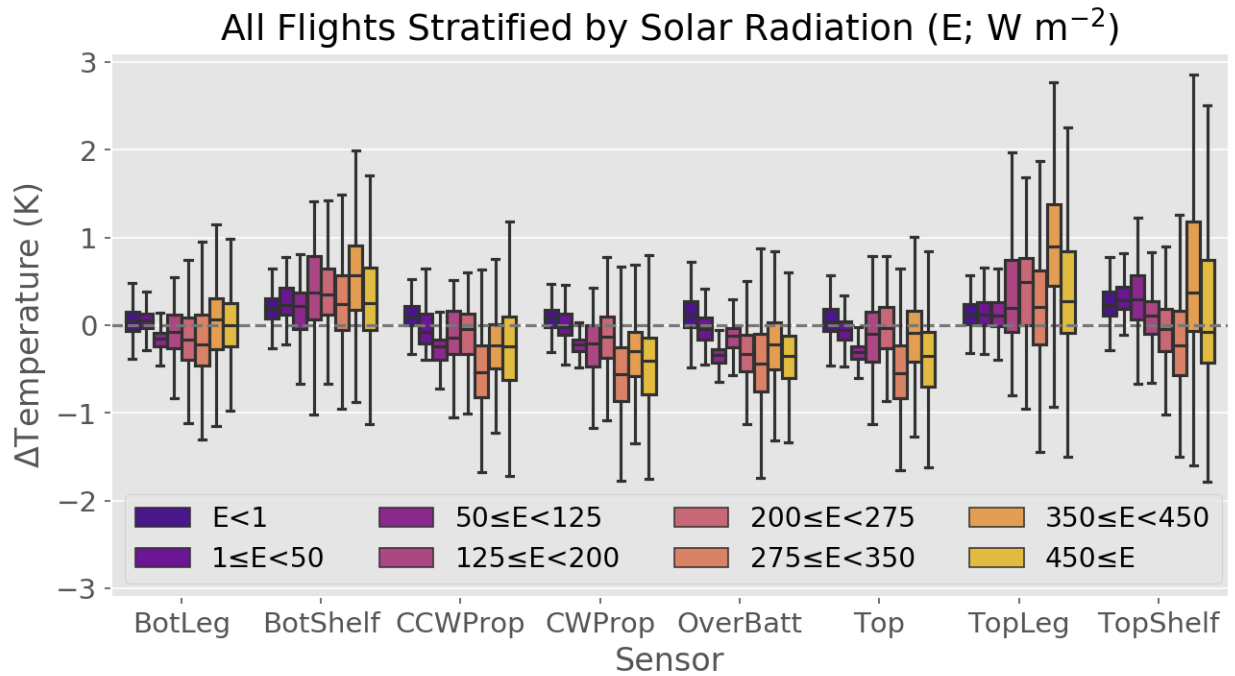


Figure 2.4: As in Figure 2.3, except that for each sensor position, the data is stratified by solar radiation,  $E$  ( $W m^{-2}$ ), observed by the surface weather station.

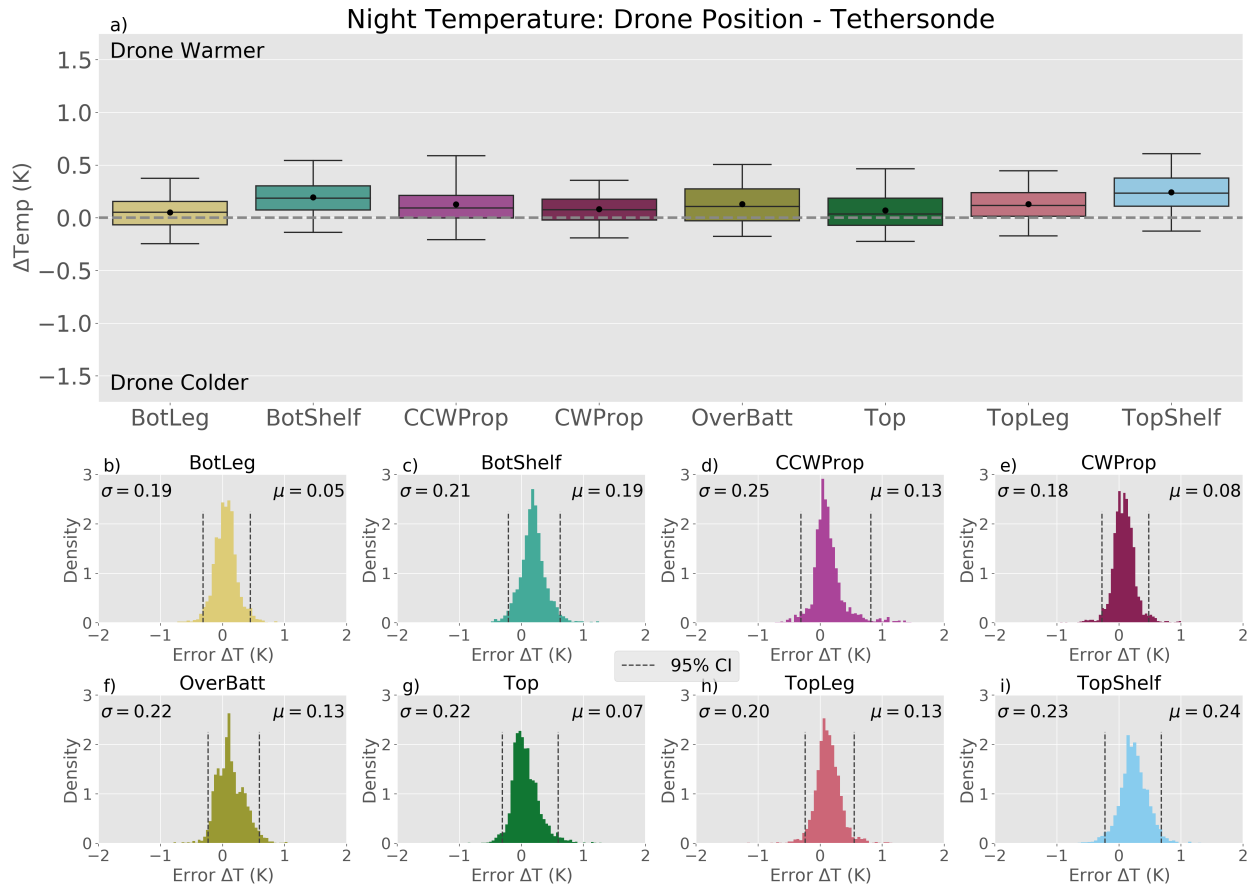


Figure 2.5: As in Figure 2.3, but for temperature errors during the nighttime flights only.

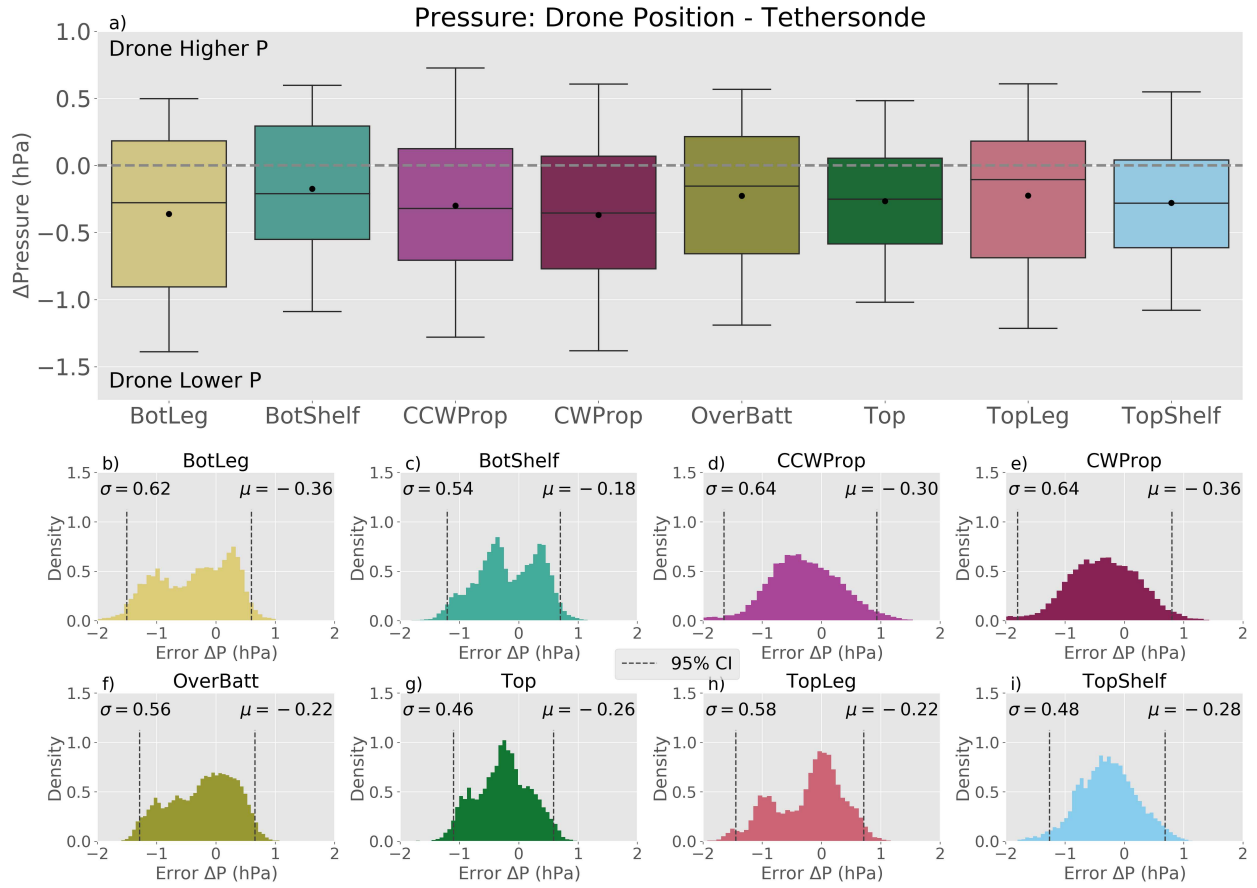


Figure 2.6: As in Figure 2.3, but for pressure errors during all (i.e. daytime and nighttime) flights.

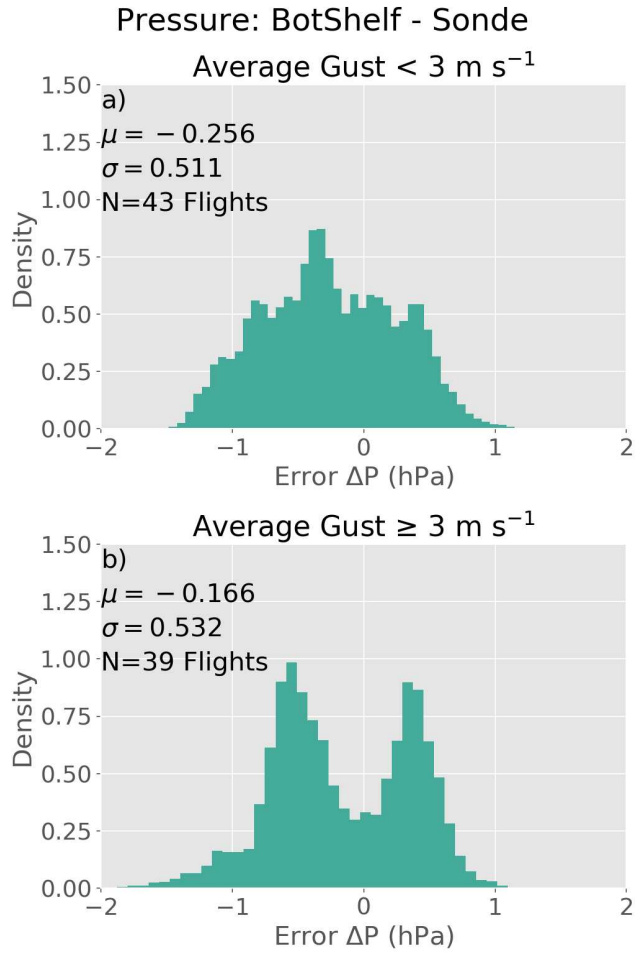


Figure 2.7: a) As in Figure 2.6c, but only including flights where the surface weather station reported an average gust of < 3 m s<sup>-1</sup> during the flight; b) Similar to (a), but for an average gust of ≥ 3 m s<sup>-1</sup>.

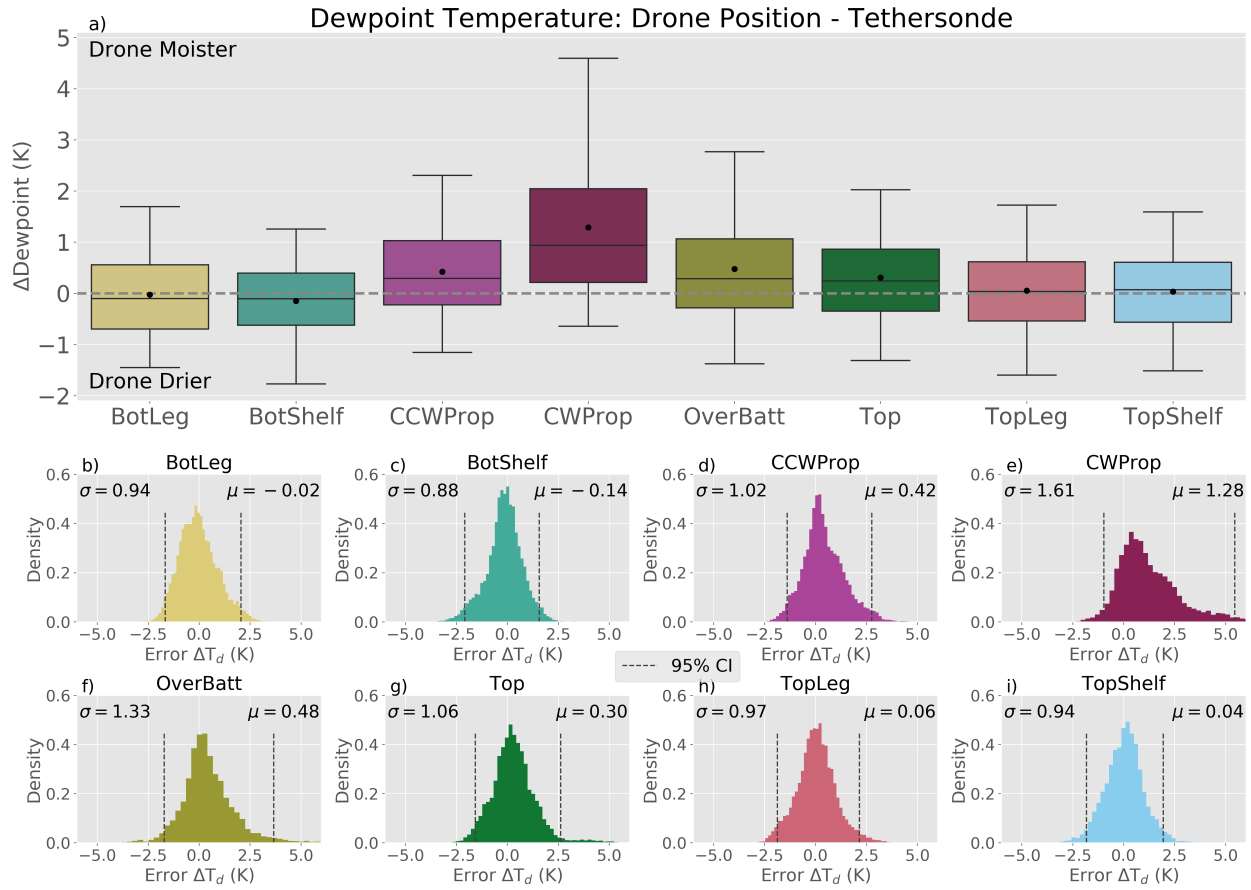


Figure 2.8: As in Figure 2.3, but for dewpoint temperature errors for all flights.

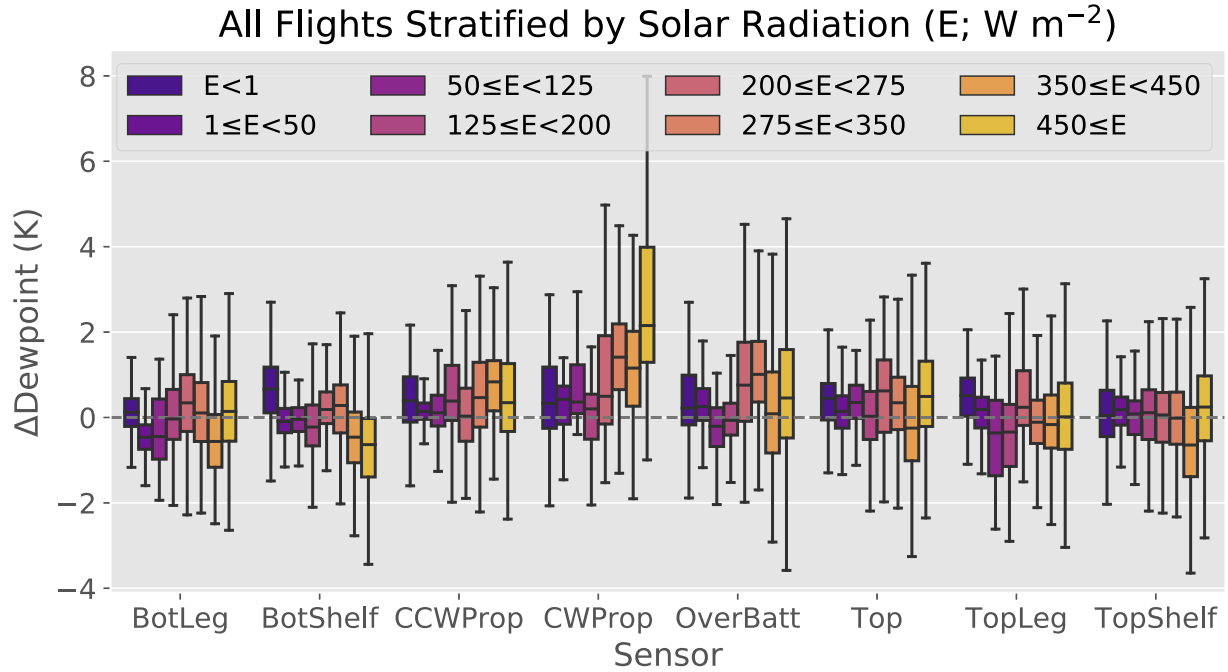


Figure 2.9: As in Figure 2.4, but for dewpoint temperature errors.

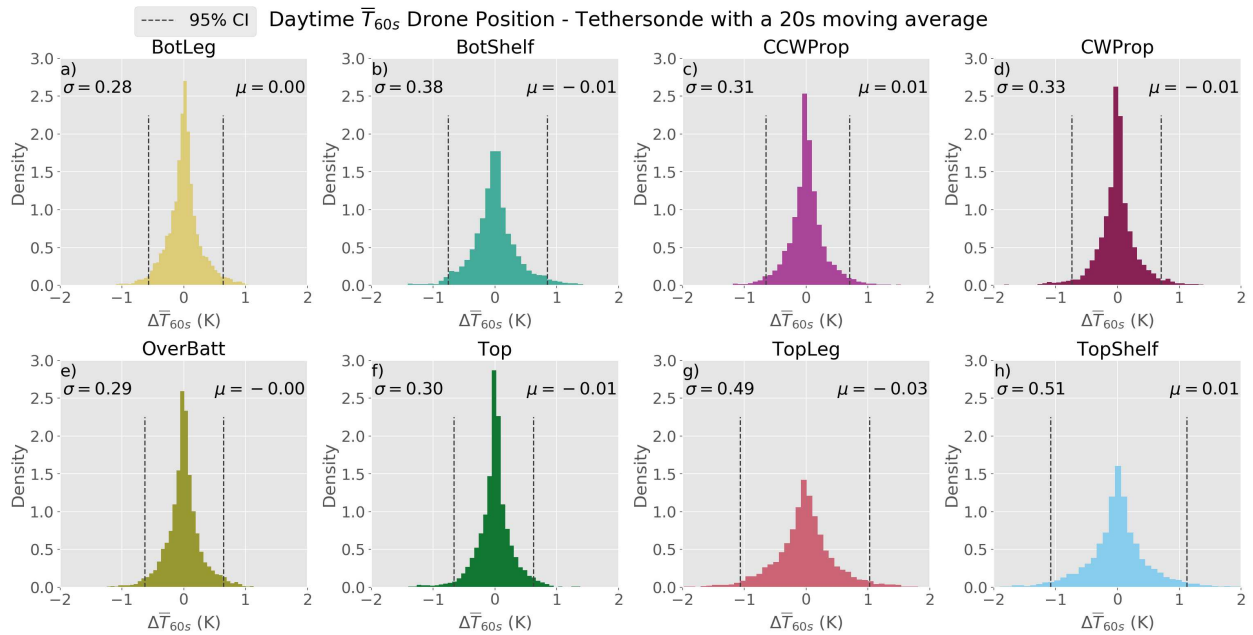


Figure 2.10: As in Figure 2.3b-i, but showing the quantity  $\bar{T}_{60s}$ , as defined in the text, for all daytime flights.

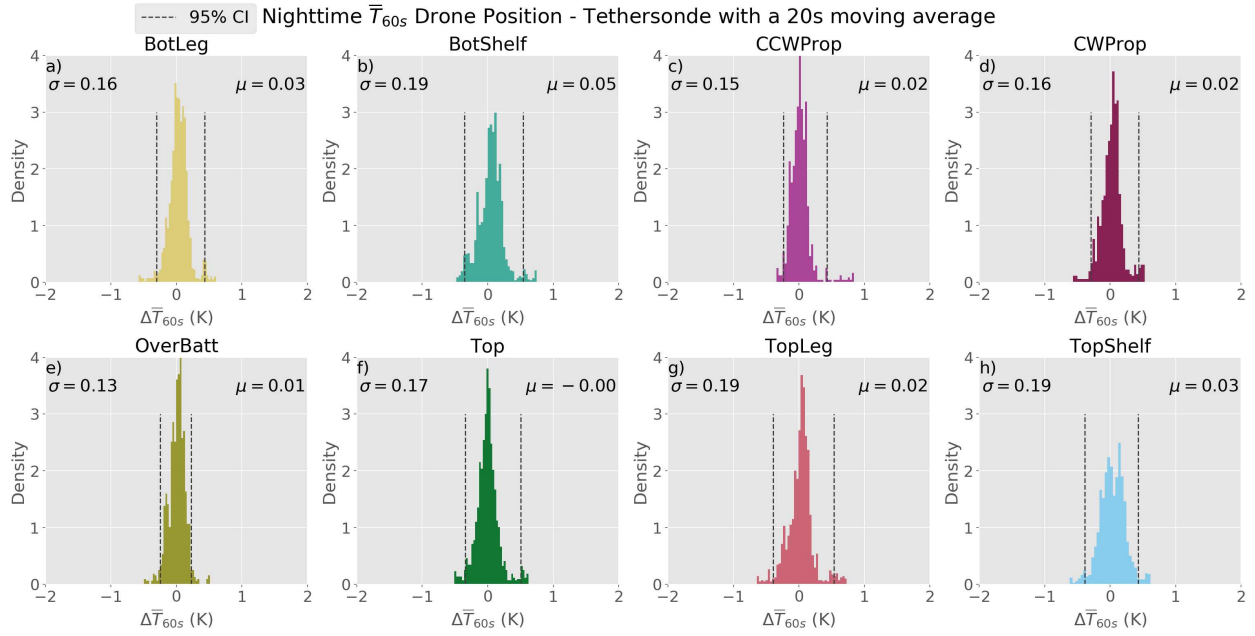


Figure 2.11: As in Figure 2.10, but for  $\bar{T}_{60s}$  during the nighttime flights only.

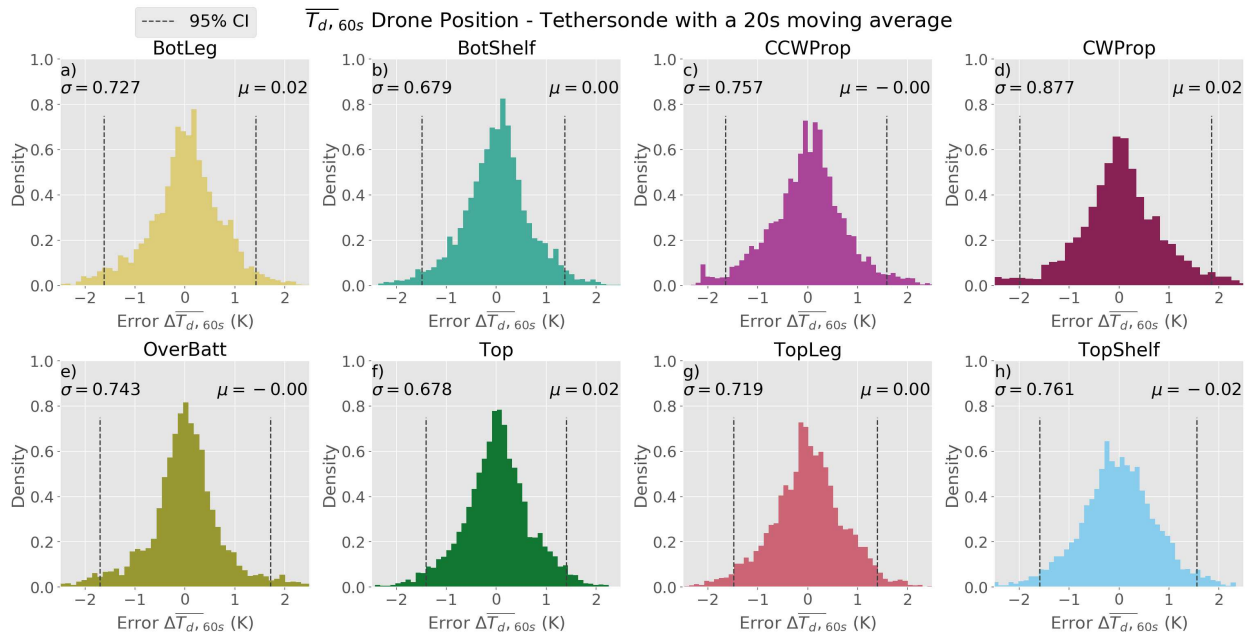


Figure 2.12: As in Figure 2.10, but for  $\bar{T}_{d,60s}$ , where  $T_d$  is dewpoint temperature.

## CHAPTER 3: *TOBAC* V1.5: INTRODUCING FAST 3D TRACKING AND OTHER ENHANCEMENTS FOR IDENTIFYING METEOROLOGICAL PHENOMENA

### 3.1. Introduction

Recently, there has been a great deal of interest in robust, large-scale objective identification and tracking of clouds and other meteorological features (e.g., Heus and Seifert, 2013; Hu et al., 2019; Núñez Ocasio et al., 2020). As the atmosphere is not a static system, diffusive, advective, dynamic and thermodynamic processes ensure that atmospheric phenomena of interest are nearly always either in motion or in a moving frame of reference, which is indicative of the utility of tracking frameworks for atmospheric data in general. Clouds are one such phenomenon for which tracking is useful. Clouds are near-ubiquitous features in the Earth's atmosphere and play critical roles not only in tropospheric heat and moisture transport, but also with respect to scattering of solar radiation and absorption/emission of infrared radiation in the context of the global climate. Convective clouds and cloud systems can range in size from tens of meters to hundreds of km; exist for as short as a few minutes and as long as days; exhibit a wide variety of morphological characteristics; and undergo complex lifecycles that have a growing initiation stage, a quasi-steady-state mature stage, and a collapsing decay stage (Cotton et al., 2011). All of these elements make clouds prime candidates for objective analysis techniques, and because of this, clouds have been successfully tracked in a variety of applications (e.g., Sokolowsky et al. 2022; Leung and van den Heever 2022; Chapters 4, 5). Clouds are far from the only meteorological phenomena where robust tracking tools are useful. For example, tracking on quantities such as aerosol concentration (e.g. Bukowski and van den Heever, 2021) and trace gas concentrations and masses (e.g. Zhang et al., 2022) is of enormous

use to atmospheric chemists, climate scientists, and others studying movement of such quantities within the atmosphere. Convective cold pools, which are density currents that manifest via the evaporation of convective precipitation, can be identified and tracked using atmospheric thermodynamic and dynamic quantities such as temperature or temperature proxies (e.g. potential temperature), water vapor concentrations, and near-surface wind fields (e.g. Tompkins, 2001; Feng et al., 2015; Drager and van den Heever, 2017; Drager et al., 2020). Atmospheric radiative quantities, such as outgoing longwave radiation (OLR), have clear uses in cloud objective identification (e.g. Gill and Rasmusson, 1983; Weickmann, 1983; Jones et al. 2022), but can also be leveraged to detect and track processes such as sea ice evolution (e.g. Singarayer et al., 2006). If such tools are made general enough, even people working outside the realm of atmospheric science can benefit from them, such as ornithologists or entomologists interested in bird and bug seasonal migration, respectively (e.g. Crewe et al., 2020; Knight et al., 2019). At present, however, only one such tool can address this myriad of uses: the Tracking and Object-based Analysis of Clouds (*tobac*; Heikenfeld et al., 2019), a Python package based in objective analysis principles that uses artificial intelligence to identify, discretize, and track objects and fields of interest.

The most powerful and unique feature of *tobac* is its variable- and grid-agnostic nature—i.e., it can be used with virtually any gridded input dataset and variable, meteorological or not. *tobac* was initially developed for use with clouds and associated meteorological data (Heikenfeld et al. 2019), and has been used for these purposes, such as tracking warm-season deep convective systems and Mesoscale Convective Systems (MCSs) via satellite-observed infrared brightness temperature (e.g. Li et al., 2021; Kukulies et al., 2021, respectively). However, due to this unique variable agnosticity, *tobac* has also been used for other applications: for example, tracking of

haboobs via dust concentration (e.g. Bukowski and van den Heever, 2021). *tobac* both draws from and expands upon the procedures developed in earlier cloud identification and tracking tools, and we have detailed some of the history of tracking tools in the atmospheric sciences below.

First and perhaps foremost, tracking has historically required a great deal of human input and attention due to a lack of computationally efficient methods for the location, assessment, and connection of different features in time. One such early method, the Thunderstorm Identification, Tracking, Analysis, and Nowcasting tool (TITAN; Dixon and Weiner, 1993), is a well-designed and powerful approach for the detection and tracking of thunderstorms, and while it does incorporate computational analysis of data, it is heavily based in physical principles (i.e., it requires specific datasets/variables and can only be used to track certain things) and manual assessment of output due to computational limitations at the time. As discussed in Dawe and Austin (2012), earlier studies involving tracking of clouds (e.g. Zhao and Austin, 2005a, b; Heus et al., 2009) required scientists to contribute a great degree of manual/visual selection to the clouds they considered in their studies. This is not only time-consuming to an extent that is impossible to scale for large datasets, but also introduces subjectivity to an analysis that should ideally be objective. Some later publications (e.g. Plant, 2009; Dawe and Austin, 2012; Heus and Seifert, 2013) have more general criteria allowing for automated selection, but exhibit computational or scientific limitations due to their design. Dawe and Austin (2012) tracked clouds as a combination of 3D liquid water content and buoyancy in 3D space, but required computationally expensive determinations of 4D spatiotemporal connectivity and had specific definitions for different cloud components, limiting use on a variety of different cloud types. Heus and Seifert (2013) simultaneously expanded on and improved the tractability of the

approach of Dawe and Austin by connecting thermals, cloud envelopes, and precipitation shafts, but reduced the amount of memory needed by projecting these fields into 2 spatial dimensions and using the vertical dimension as a contiguity check between feature columns. However, both Dawe and Austin's (2012) and Heis and Seifert's (2013) methods were designed to be used in LES output fields of shallow cumulus with a vertical extent of less than 4 km, limiting the applicability of these methods with cloud systems that exhibit more vertical structure (e.g., layered clouds, deep convection or slantwise convection) and other datasets that have similarly complex 3D morphology. Gropp and Davenport (2021) recently developed a powerful tracking tool for supercell thunderstorms that was effectively demonstrated at a 3-hourly time resolution (coarser than the requirements of many tracking tools) but is limited by its specific case use and cannot be easily generalized. *tobac* utilizes many of the strengths of these preexisting tools while broadening science applications and optimizing procedures to result in a more general and powerful analysis tool.

Despite the utility of *tobac* and the strengths of this tool over earlier such packages, the increasing resolution of models and identification of new use cases (such as in LES modelling) have made it clear that the code base requires enhancement from both a scientific and procedural point of view. Necessary updates to *tobac*'s scientific capabilities are the inclusion of the third spatial (vertical) dimension in feature detection and tracking and internal tools allowing for spectral smoothing of data. More procedural improvements which would also further the utility of this package are increases in computational efficiency, ingestion of multiple data sources on different grids (e.g., performing feature detection on one grid and segmentation on a separate grid), and treatments for model periodic boundary conditions (PBCs).

Our goal in this publication is to present each of these new improvements that have been released as part of *tobac* v1.5. In Section 3.2, we discuss the strengths and weaknesses of *tobac* v1.2, while Section 3.3 details the scientific improvements. Section 3.4 presents the procedural enhancements, and Section 3.5 provides a summary of our changes to *tobac*, concluding thoughts on *tobac* v1.5, and some planned changes which will be included in future releases.

### **3.2. *tobac* v1.2 overview**

Before elaborating on the new capabilities which have been included in *tobac* v1.5, we begin with a general overview of the design and capabilities of the original *tobac* library, denoted v1.2. *tobac* was first developed through a multi-institutional collaboration (Heikenfeld et al., 2019) in order to provide a code base for “tracking and analysing individual clouds in different types of datasets”. This package consists of three primary components: *feature detection*, or the objective identification of features from minima or maxima in gridded data; *segmentation*, or the discretization of the same or different gridded data based on previously detected features; and *tracking*, or the linking of detected features to one another through time. Segmentation and tracking operate independently of each other, but both require feature detection to have been performed on a data field of interest. These procedures can be performed on any gridded data field of interest, though for *tobac* v1.2, it must exist in two (feature detection, segmentation, and tracking) or three (segmentation only) spatial dimensions, requiring some form of data dimensionality reduction for feature detection and tracking when data grids are in 3D. These key elements, demonstrated on a field of radar reflectivity data, can be seen in Figure 3.1. The fine details of how these components were constructed is detailed in Heikenfeld et al. (2019), but we discuss the generalities and how *tobac* can be applied to different use cases within this section.

Feature detection in *tobac* is performed by first establishing one or more data thresholds which gridded data values must exceed in order to be considered for placing features. Contiguous regions of gridded data meeting these criteria, as well as additional criteria such as a user-set minimum size, are saved as unique single-point identifiers (which can be set by users to either be geometric centroids, weighted-difference positions, or extrema within the data) with their horizontal positions in each spatial dimension. If multiple thresholds are used, features detected at a higher-magnitude threshold that exist within a lower-magnitude region of features supersede and replace the feature(s) detected at the lower-magnitude threshold (e.g. Heikenfeld et al., 2019, their Figure 2). This multi-threshold capability allows for the identification of greater-magnitude data existing within a lower-magnitude data region without losing the sensitivity to lower-magnitude data. For example, using multiple thresholds on a modelled vertical velocity field enables the detection of deep convective updrafts within a broader, weaker updraft region as well as isolated, weak boundary layer thermals. An illustration of feature detection being performed on gridded NEXRAD radar reflectivity data obtained during the CSU Convective Cloud Outflows and UpDrafts Experiment (C<sup>3</sup>LOUD-Ex; van den Heever et al. 2021) can be seen in Figure 3.1a-b. In this figure, convective storms in a grouping near Cheyenne, WY (Figure 3.1a) are identified using a radar reflectivity threshold of 30 dBZ. Each of these storms is labelled as a single-point feature, marked in Figure 3.1b. With the identification of such features, the additional components of *tobac* – segmentation and tracking – can be fully utilized.

The segmentation approach within *tobac* v1.2 begins with a previously identified set of *tobac* features. Where the feature detection procedure reduces contiguous regions of data to single points, segmentation discretizes a full volume or surface area associated with each of these

features. For both 2D and 3D segmentation, feature positions are used to place seeds that grow outwards to identify an area or volume associated with a feature, using the `skimage.segmentation.watershed` function (van der Walt et al., 2014). This allows for the discretization of data regions pertaining to each feature, even when multiple features exist within the same contiguous data region. In 2D watershedding, this procedure simply operates in two dimensions, but for 3D watershedding, the entire vertical column where our 2D feature is located has markers placed in it, except where data points do not exceed the segmentation data threshold. In circumstances where data fields are layered, staggered, discontinuous in height, or otherwise irregular through the vertical dimension, this may lead to some data fields being erroneously segmented together, but such data are often identifiable through quality control of *tobac* output. The discretized field, or “segmentation mask”, for each timestep is saved as an array. Segmentation fields produced on 2D radar reflectivity data from 2D radar reflectivity features are shown in Figure 1c. These regions illustrate the wider reflectivity fields outside of the convective cores that are associated with each of the detected features, likely precipitation regions raining out from the larger clouds being driven by the convective cores.

Finally, the tracking procedure within *tobac v1.2* also requires a previously existing set of *tobac* features. These features are then used with the Python Trackpy library (Allan et al., 2021) to predictively link connected features in time. The presence of this tool within the *tobac* package introduces time evolution to the phenomenon identification that feature detection does and feature-associated area/volume produced by segmentation. An example of *tobac* cell tracking from our previously referenced radar data features is presented in Figure 3.1. Here, the movement of these identified systems in previous radar scans are denoted by the red lines trailing

from each feature point, and analyzing the information provided by this temporal evolution can be highly useful in convective storm lifecycle studies and other such temporally dependent foci.

Despite the clear objectivity, utility, and power contained within this tool, *tobac* v1.2 had several important limitations from both a scientific and procedural standpoint, as touched on in the introduction. The limitation of feature detection and tracking to 2D, as well as the column-based approach to 3D segmentation using 2D features, means that data fields which do not reduce cleanly into 2 dimensions (e.g., environments with strong vertical wind shear or layered clouds; deep convective clouds with multiple discontinuous vertical regions producing condensate; tilted convective storms; and intrusions of aerosol layers composed of different species at different altitudes) might produce untrustworthy or confusing results when analysed using *tobac* v1.2. The included data processing tools are also limited, with no bandpass or spectral filter techniques included in the *tobac* v1.2 package to smooth or isolate data in noisy fields. From a computational perspective, the original implementation was also not well optimized (taking weeks or more to process large datasets), requiring substantial increases in computational efficiency for tractable usage with large datasets. Using detected features to segment data that exists on a different grid is also challenging with this version of *tobac*, as it requires a great deal of user processing to remap data to different grids. Finally, *tobac* v1.2 also lacked the ability to recognize and treat features, segmentation fields, and tracks on data with PBCs, a common characteristic in idealized numerical models. All of these needs motivated the improvements that are discussed in the following two sections.

### 3.3. *tobac* v1.5 – Scientific Improvements

#### a. 3D Tracking

One of the most scientifically consequential improvements to *tobac* made as a part of v1.5 is the addition of the vertical dimension to feature detection and tracking, as well as an overhaul of 3D segmentation. Due to the structure of *tobac*, each of these changes required different modifications to the core modules contained within the code base.

For feature detection, much of the overall code logic remains unchanged, but is expanded to include the additional spatial dimension. The feature detection functions are now capable of determining whether their input data exist in two or three spatial dimensions, after which they branch accordingly within the code. When 3D data are input, contiguity and spacing of regions within this data are now assessed in all three spatial dimensions versus just the horizontal dimensions. Further, the code also supports both uniform and non-uniform vertical grid spacing, allowing for use with modelling and observational data exhibiting either of these common grid structures. Data fields with a 3D input now output two additional data points, ‘vdim’ and ‘altitude’, which are absent from 2D output. Including these additional data can be used for an abundance of analyses that depend on vertical information, e.g., defining the vertical structure of updrafts and downdrafts within convective clouds; identifying intrusions of concentrated aerosol layers; and highlighting vertical layers of elevated environmental stability, to name a few.

In addition to the wider variety of scientific use cases that vertical information enables, these code changes also lead to substantial differences in feature detection output between 3D data and their counterparts reduced to 2D, such as that seen in Figure 3.2. Here, a model vertical velocity field is used for feature detection of updrafts at 1, 3, 5, and 10 m/s thresholds, with the 2D reduction being a plan view of the column maximum value. Figure 3.2a illustrates how much

of the vertical structure of a 10 m/s feature in the data (white dots within the coloured isosurfaces) is captured by our new method, and shows via comparison to Figure 3.2b that 3D features' horizontal positions may differ from their 2D-projected counterparts when the vertical dimension is included in feature detection and positioning. While 2D feature detection is less computationally expensive than 3D and may be a faster solution that produces comparable results, users may also find that 2D projections of 3D data can lead to erroneous results, such as that demonstrated in Figure 3.3. Here, a cumulus cloud and cirrus cloud existing within a sheared environment are traveling in opposite horizontal directions, with the cumulus cloud also moving upwards in time. Figure 3.3a-c depict the time evolution of this scene when 3D motion and detection are considered by *tobac* v1.5: not only are these two discrete clouds recognized, identified, and tracked correctly in time, but the vertical displacement of the cumulus cloud is also apparent in its track. Conversely, Figure 3.3d-f depict how *tobac* v1.2 is able to identify the clouds in the initial scene, but fails to track the cumulus cloud due to the cirrus cloud hiding it from view in Figure 3.3e due to the two-dimensional framework. This leads to the cirrus cloud being correctly tracked through time, while tracking of the cumulus cloud is nonexistent, its height evolution is missed, and the failure to detect it as a feature in Figure 3.3e leads to it being considered a separate, completely new tracked feature in Figure 3.3. Thus, a possible error arising from collapsing 3D data to 2D is the disappearance of 3D features.

Unlike with feature detection, the segmentation routine in *tobac* v1.2 already has some capabilities for 3D data processing, as discussed in the previous section. The column-based 3D segmentation approach – where the entire vertical column at a feature location is seeded with markers for watershedding (the segmented regions are identified growing outward from the seeds) - works reasonably well for 2D features when the 3D field being segmented does not

exhibit much vertical stratification or wind shear. However, seeding the full column is clearly not an ideal approach when we have the feature's vertical position, as seen in 3D-detected features. As such, we have introduced a new "box seeding" method which, instead of a full column, seeds a box of user-defined size in each dimension centred at the 3D location of the feature. This eliminates the issues ensuing from seeding an entire column, while also ensuring that features which are close in 2D space but exhibit a great deal of separation in the vertical do not unduly influence each other's segmentation masks.

A further example of the new 3D segmentation procedure using LES model data is seen in Figure 3.4: Figure 3.4a shows the segmentation mask volume produced via column seeding, while Figure 3.4b's segmentation mask was produced by box seeding covering 5x5x5 cells. Figure 3.4a's segmentation mask clearly exhibits anomalous cells extending up and down from the main volume, including a disconnected region of cells about 1 km above the rest of the mask, which are unphysical and do not manifest in the box-seeded mask seen in Figure 3.4b. Quality control by users, such as visual inspection of segmentation masks, can help to mitigate this issue. However, this is a laborious process, and since minimizing user effort for objective analysis is one of the key motivators for the development of *tobac* and other comparable tools, use of the box seeding approach here is clearly the superior approach when users have the choice to do so. This benefits the science itself by making analyses more consistent and less influenced by user subjectivity and qualitative interpretation, and also permits layered feature detection and segmentation.

Finally, the 3D modifications to tracking are more comparable to those seen for feature detection than segmentation but include similarly powerful advances to both of these components. Since tracking in *tobac* is largely processed using Trackpy functions, we leveraged

the preexisting Trackpy framework to perform 3D tracking, keeping results both internally consistent and enabling the use of the same general methodology, regardless of whether the user is tracking on 2D or 3D data. Further, our implementation of 3D tracking in *tobac* v1.5 allows users to track on data in 3D with irregularly spaced vertical grids (e.g., stretched model grids) without requiring the user to re-grid the data. Figure 3.5 illustrates the use of 3D tracking on NEXRAD radar reflectivity data, showing the movement (red line) of the detected feature in both horizontal (Figure 3.5a-c) and vertical space (Figure 3.5d-f) on a feature that is tilted with height. Identifying the centers of such features and discretizing associated data fields are also much more realistic with 3D feature detection and box seeding, respectively. As tracking brings temporal evolution into feature analyses, incorporating the vertical dimension further expands these capabilities by allowing users to assess the change in vertical position over time instead of just the horizontal projected position. For use cases where the features of interest are known to exhibit vertical movement as part of their evolution – such as the growth and decay of convective clouds; the development of cold pools and hail cores in thunderstorms; and mechanical lofting of aerosols such as dust or pollen – the importance of including this dimension is essential in feature assessments over their life cycles.

### *b. Spectral Filtering*

While *tobac* v1.2 already included some methods for smoothing of data, when examining some features of interest certain observational and model fields may still be too noisy to detect features of interest. For example, if one is interested in identifying and tracking atmospheric rivers using a high-resolution dataset, individual convective clouds should be smoothed out. In order to allow users to examine their features of interest without requiring preprocessing of data outside of *tobac*, a new spectral filtering tool has been incorporated into *tobac* as part of the v1.5

update. This tool is designed to facilitate the identification of meteorological phenomena at specific spatial scales (e.g. the MJO, equatorial waves, atmospheric rivers, mesoscale vortices, etc), and to remove sub-mesoscale noise in high-resolution data when the user is interested only in larger spatial scale features. It works by first performing a discrete cosine transform (DCT) on 2D atmospheric fields, representing them in spectral space as a sum of cosine functions with different frequencies (Denis et al. 2008). The resulting spectral coefficients correspond to normalized wavenumbers that can be converted to actual wavelengths, which are then used in the construction of a bandpass filter that has the same shape as these spectral coefficients in wavelength/wavenumber space. Multiplying this bandpass filter with the spectral coefficients removes wavelengths outside of the user-specified band, which can then be converted back to the original domain via inverse DCT. A visualisation of atmospheric data and the spectral elements used for filtering are demonstrated in Figure 3.6. Figure 3.6a displays the initial 2D input field (here, a WRF relative vorticity dataset), Figure 3.6b illustrates the transformation of the data in Figure 3.6a to spectral space, and Figure 3.6c-d show the construction of 1D and 2D bandpass filters for wavelengths between 400 and 1000 km. The results from applying such filtering to an ERA5 vertically integrated water transport dataset and a WRF relative vorticity dataset are shown in Figure 3.7. Figure 3.7a and c illustrate the original, pre-filtered fields of ERA5 and WRF data, respectively, while Figure 3.7b and d illustrate the same corresponding fields after utilization of the filter. It is clear from Figure 3.7b and d that the application of the spectral filtering smooths the dataset and allows for easier identification of only large-scale relative vorticity features. Inclusion of this tool in *tobac* v1.5 quite clearly expands the package's utility while reducing the amount of extra work needed for end users to pre-process data of interest.

This technique has previously been used to identify mesoscale vortices in convective permitting climate simulations (e.g., Kukulies et al. 2022, in review).

Overall, the 3D implementation and the spectral filtering tool add a great deal of scientific power to *tobac* by expanding on the types and dimensionality of contiguous structures that it can identify within datasets, allowing the tool to be used with more dynamically evolving phenomena, and providing an additional level of filtering to isolate atmospheric phenomena of interest. However, even more improvement of *tobac* can be achieved with the addition of procedural changes such as code optimization, homogenization of grids for different data, and treatment of PBCs. These procedural adaptations are discussed at length in the following section.

### **3.4. *tobac* v1.5 – Procedural Improvements**

#### *a. Code Optimization*

Several inefficiencies were identified across the body of code, and subsequently, alterations were made to each module to enhance their overall computational speed. Making these changes led to speedups on the order of 100x for feature detection and 1,000,000x or more for tracking. The scaling of these modules' speeds as a function of the number of features, a proxy for data size and complexity, between *tobac* v1.2 and v1.5 can be seen in Figure 3.8, with feature detection in Figure 3.8a and tracking in Figure 3.8b. To provide a single example of what this means when using *tobac* on a moderately sized dataset (3000 x 5000 points, 288 timesteps), performing feature detection on a full day of GOES-16 IR data only takes about a minute of computing time now, where it originally took around an hour with *tobac* v1.2 when holding the computer system used constant. This has implications for the tractability of using *tobac* v1.5 with larger datasets: analyses on especially large datasets (10s-100s of TB) that would take weeks to

perform with *tobac v1.2* now only take hours to days, which expedites the research that can be conducted with this tool.

### *b. Remapping Data on Different Grids*

Beyond recognizing that the efficiency of *tobac* needed to be improved to make certain analyses tractable, we also understood that researchers working with data from different sources often have a need to combine these datasets in some way. This process can be greatly complicated by observing platform nuances such as viewing angle and field of view; temporal frequency and spatial resolution; and the dynamic range of the data. Issues such as differing fields of view and spatial resolution have particularly strong implications for the uses of objective analysis tools like *tobac* due to the projection of data onto different spatial grids. Within the framework of *tobac*, we have introduced a new data processing tool which allows for the combination of datasets (both models, both observational, and even a mix of the two) so that *tobac* can be more easily used with a broader variety of data. One case for the use of this tool is in observational analysis of convection via radar and satellite datasets, which we demonstrate in Figure 3.9. Features detected from NEXRAD reflectivity data exceeding a 30 dBZ threshold are shown in Figure 3.9a. These features are then used as markers to segment a GOES-16 satellite-observed brightness temperature dataset, pictured in Figure 3.9b. The satellite brightness temperature data have been remapped to the same grid as the radar data prior to performing the segmentation process, so that features are correctly located within the segmentation field of interest. Ultimately, the segmentation outlines shown in Figure 3.9b depict the anvils corresponding to each radar reflectivity feature, except for the top-right feature marked by the grey dot in Figure 3.9b, which is a convective core that does not yet have an associated anvil.

### *c. PBC Treatments*

As noted in the introduction, idealized numerical models often utilize PBCs in order to isolate simulations from external forcings and reduce the influence of the lateral model boundaries on the simulation behaviour. With PBCs, phenomena flowing out of one end of the model boundary simply re-enter the domain at the opposite boundary for that dimension. However, v1.2 of *tobac* did not have any capabilities for recognizing the continuity of features, segmentation masks, or cell tracks which crossed or were split into multiple parts by boundaries, and the code base required these improvements for use with model configurations including PBCs in one or both lateral dimensions.

Most of the changes needed for PBC treatments in feature detection lie within the identification of contiguous regions separated by an artificial boundary and the positioning of features which exist across both sides of a boundary. In the original v1.2 procedure, a failure to recognize when contiguous fields are split by artificial model boundaries leads to an erroneous multiplication of detected features at these boundaries, which further cascades into unphysical segmentation fields and cell tracks. A depiction of PBC feature detection with *tobac* v1.2 and *tobac* v1.5 being performed on an LES model 2D column maximum vertical velocity field can be seen in Figure 3.10. Figure 3.10a shows the overall data field (with values less than 0.5 m/s masked in grey), and Figure 3.10b visualizes the initial field of labelled regions identified at a 0.5 m/s threshold prior to utilizing our PBC treatment. Figure 3.10b contains a total of 6 different regions due to the multiple boundary crosses exhibited by this vertical velocity field and would produce 6 different features if a PBC treatment was not applied, despite it being plainly apparent that this field should be a single unified region. After performing our PBC treatment which overwrites the labelled fields, the resulting unified label can be seen in Figure 3.10c, which

would be correctly identified as the single feature it actually is. Utilizing the PBC treatment in the zonal direction also facilitates the use of *tobac* with some global model and observational datasets, and represents the first steps towards enabling global tracking. The PBC treatment for segmentation largely follows the same principles as that for feature detection, except it requires adjustments, rather than complete unifications, to be performed when segmentation masks collide at a model boundary. Beyond these, the PBC procedures for feature detection and segmentation are quite similar.

The tracking procedure for PBCs differs from that for both feature detection and segmentation due to the key purpose of the PBC treatment being to link cell tracks that already exist. Provided that one has performed the PBC treatment within feature detection, propagating features will be crossing boundaries in a smooth manner without the introduction of spurious features. An example of the PBC tracking approach can be seen in Figure 3.11: Figure 3.11a displays the erroneous recognition of two distinct cell tracks from an evolving feature crossing the periodic boundary, while Figure 3.11b shows the correct identification of a single cell track with the PBC tracking approach. This new capability enables a much more robust assessment of cloud lifecycles and other such temporal processes in models with PBCs that would otherwise produce a disjoint or garbled picture with non-PBC tracking. As discussed above with relation to feature detection, this PBC code is an important step towards the addition of global feature detection, segmentation, and tracking into *tobac*. At present, cylindrical (zonal) global tracking (which can be used on GPM data, for example) is enabled within this framework, but features living near or crossing over the poles are still an issue that must be addressed in future versions of this package.

### 3.5. Summary and Conclusions

Our overall goals for the improvements to *tobac* detailed within this manuscript were to enhance the package's scientific capabilities and utility, improve its efficiency, and incorporate new tools for data processing and more complex analyses. The inclusion of these changes, as well as the previously existing flexibility of *tobac* and its variable- and grid-agnostic (i.e., capable of working on any gridded dataset) nature, make *tobac* simultaneously one of the most powerful and malleable objective analysis tools that presently exist in our field.

From a scientific point of view, the inclusion of the vertical dimension allows for identification, discretization, and tracking of far more complex meteorological structures than *tobac* v1.2 could perform. It also allows users to better capture the spatiotemporal evolution of clustered phenomena that are difficult to isolate in 2D projections of 3D data. The included spectral filtering tool also improves the scientific utility of *tobac* by providing a method for users to isolate specific frequencies of interest in the data they are using, precluding the need for external data processing or the use of datasets that have already been smoothed.

The procedural enhancements made to *tobac* as a part of v1.5 also lead to a vast expansion in the capabilities of this package. First and arguably foremost, the computational efficiency improvements, ranging from 100x to over 1,000,000x speedup depending on the module being used and the nature of the data, allow users to conduct analyses in far less time than was possible before. Such efficiency improvements allow users to leverage higher resolution data and overall larger datasets than *tobac* could reasonably manage previously. The data regridding procedures that are now included also enable the combined use of multiple different datasets existing on different grids. Such uses include tracking convective cores on radar and identifying anvil regions with satellite data, and modelling the mechanical lofting of

dust in haboob events to compare to satellite observations of the overall dust outflow. The new spectral filtering tool also expands the types of different data that users can include for their analyses – for example, detecting and tracking of African Easterly Waves that are obscured by noise in satellite wind field observations. Finally, adding the capability to recognize and robustly address PBCs has also widened the utility of *tobac* by enabling its use with these common idealized model setups.

Although we have made a number of thorough modifications to the *tobac* code base as a part of v1.5, future updates are already in the works as part of the next major release, *tobac* v2, and an active, international community of developers continue to maintain its code base. While much of the future improvements are still under discussion, some of the key elements that are planned for the next major release include integration with the TiNT is not TITAN (TiNT; Raut et al., 2021) tracking package, and a transition away from *tobac*'s current memory-intensive data structures to data structures that allow for out-of-memory computation instead. The overarching vision for *tobac* v2 is, at present, to continue development and enable better support for Big Data use cases.

### 3.6. Figures

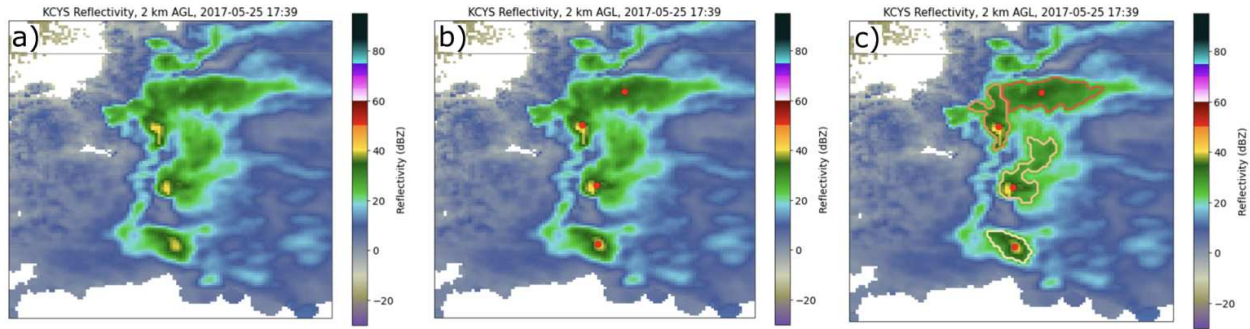


Figure 3.1: Demonstration of *tobac* feature detection and segmentation of NEXRAD radar reflectivity data from the Cheyenne, WY radar on 25 May 2017 during the C<sup>3</sup>LOUD-Ex field campaign (van den Heever et al., 2021). Panel (a) shows the actual radar data, panel (b) displays the objectively identified radar reflectivity features for a threshold of 30 dBZ as red dots, and panel (c) shows the reflectivity segmentation regions associated with the features as differently colored outlines.

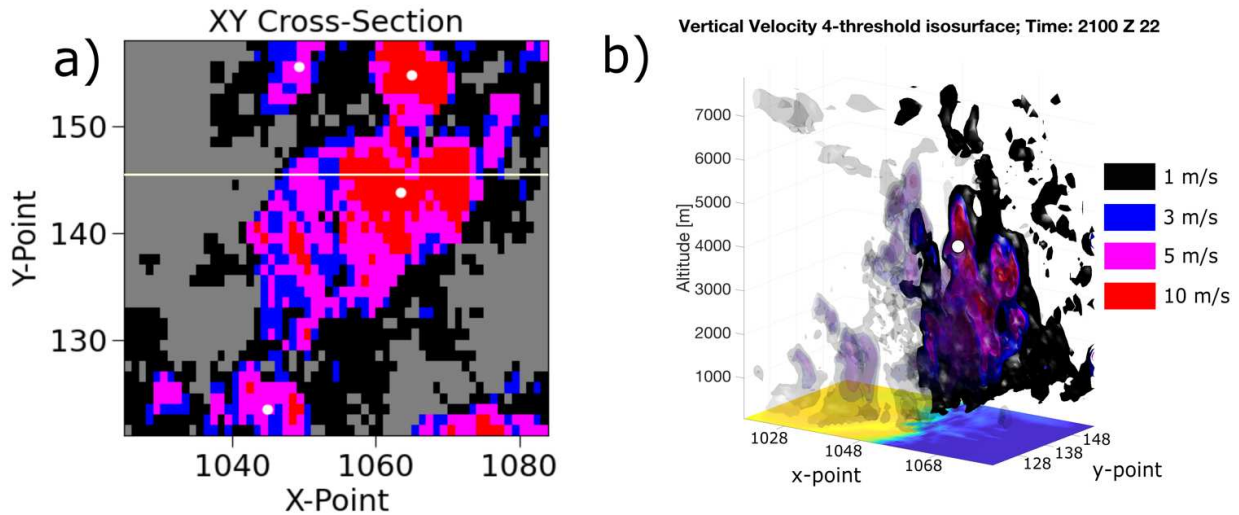


Figure 3.2: An illustration comparing cross-sections of 2D and 3D updraft four-threshold feature detection on the same model 3D vertical velocity field. Panel (a) shows the projection of column maximum vertical velocity and the multiple features contained in this area, while panel (b) shows a cutaway 3D isosurface plot of a 3D updraft detected at the 10 m/s threshold covering the same area as panel (a). Black, blue, magenta, and red shading indicate pixels exceeding the 1 m/s, 3 m/s, 5 m/s, and 10 m/s thresholds, the white dots illustrate feature positions within each cross-section, and the white line in panel (a) represents the location of the front-left cutaway in panel (b), ahead of which (in y-point space) transparent isosurfaces are used to reveal the complex inner structure of the updraft via the opaque isosurfaces.

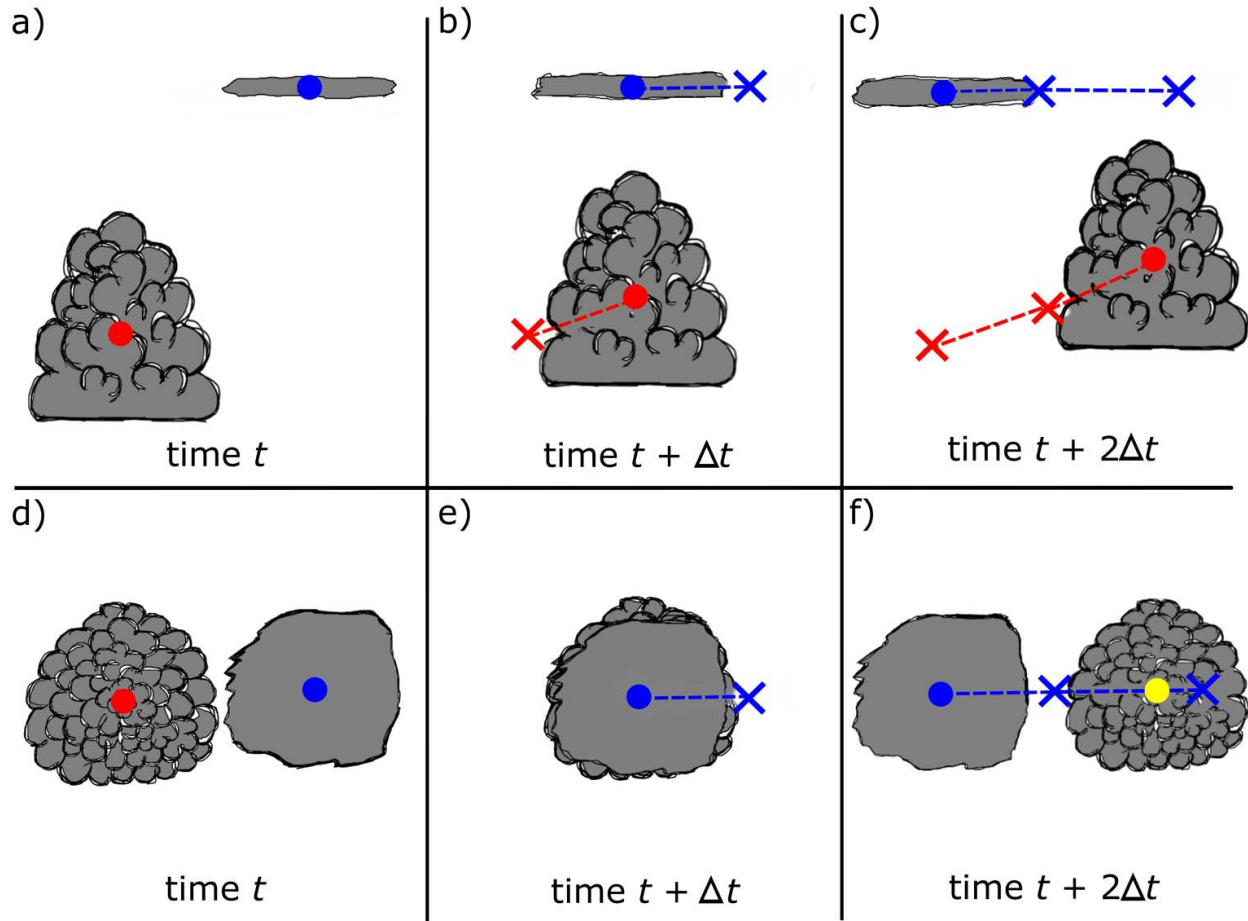


Figure 3.3: A depiction of *tobac* v1.5 (top row, vertical cross section) and *tobac* v1.2 (bottom row, plan view) feature detection and tracking for a scenario with upper-level cirrus moving over cumulus cloud developing in a sheared environment. Each column's panels are depictions from the same time. The *tobac* v1.2 approach pictured in the bottom row fails to capture the temporal evolution and vertical propagation of the cumulus cloud due to the overlying cirrus, and even incorrectly recognizes the cumulus in panel (f) as a completely new feature and track from its earlier stage in panel (d), while the *tobac* v1.5 approach (top) correctly identifies both the cumulus and cirrus clouds as independent features and tracks their vertical positions over time. The colored circles denote different features at their present times in each panel, with the colored X's indicating their position at previous times and the dotted lines representing the corresponding tracks. The symbol  $t$  here denotes a generic starting time, while  $\Delta t$  denotes the timestep from scene to scene.

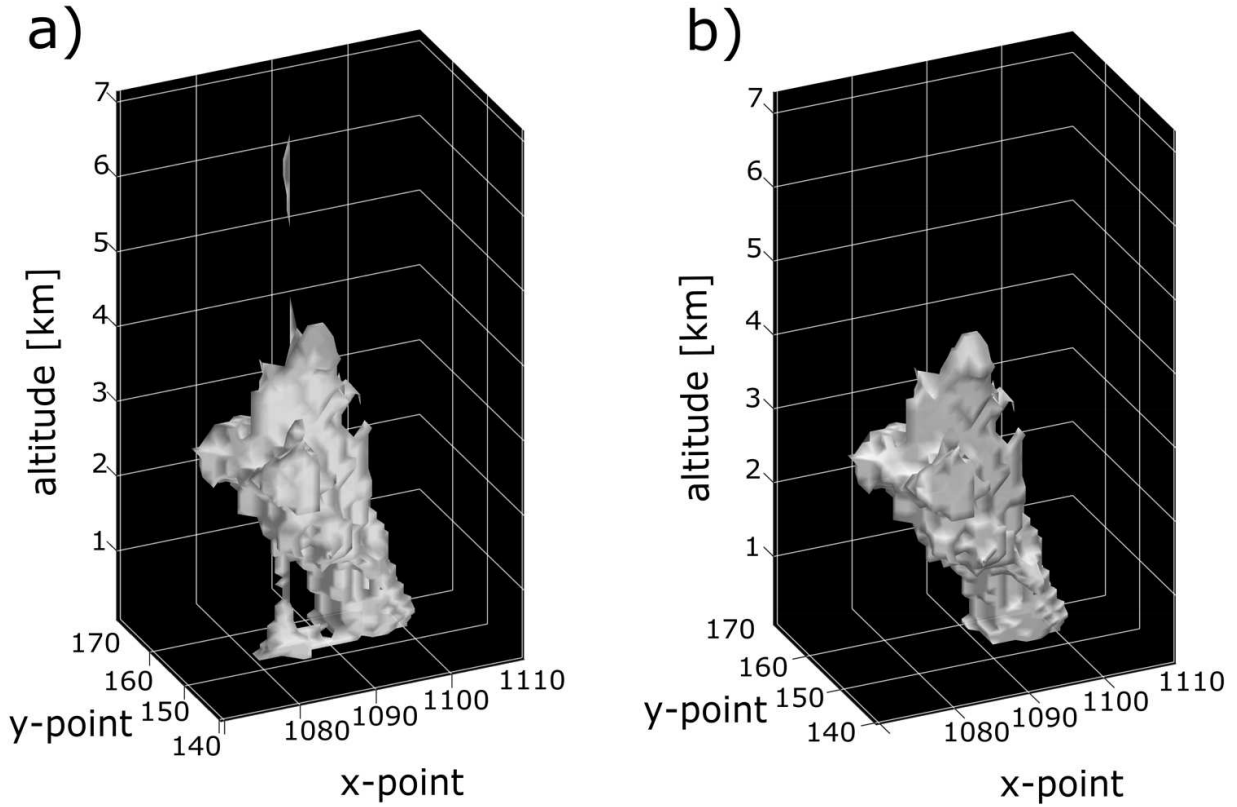


Figure 3.4: Demonstration of 3D segmentation using (a) the original “column” versus (b) the “box” seeding method, showing the differences in output produced by the different methods. 3D feature detection was performed on LES numerical model vertical velocity data from the Regional Atmospheric Modeling System (RAMS) v.6.2.14, with segmentation being performed on the corresponding model total condensate field. Segmentation in panel (b) used a uniform box seed size of 5 in x, y, and z.

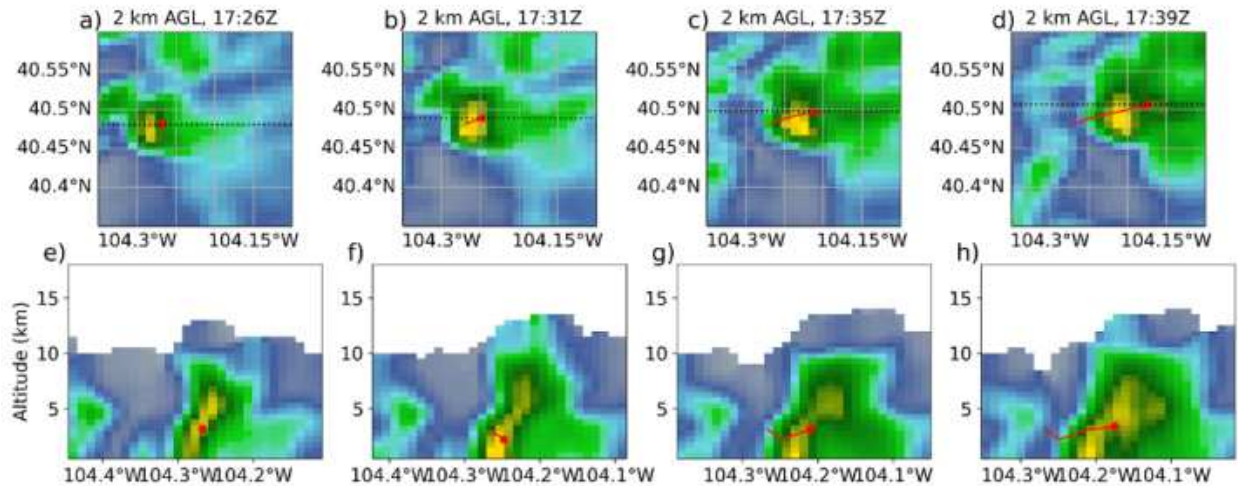


Figure 3.5: Demonstration of 3D tracking in *tobac* on NEXRAD radar reflectivity data. The top row shows the plan view in latitude-longitude space, while the bottom row consists of latitude-altitude cross sections corresponding to each of the times presented in the plan view above – thus, (a) and (e); (b) and (f); (c) and (g); and (d) and (h) are all pairs. The red dot shows the present feature location, while the red line trailing behind it shows the detected track.

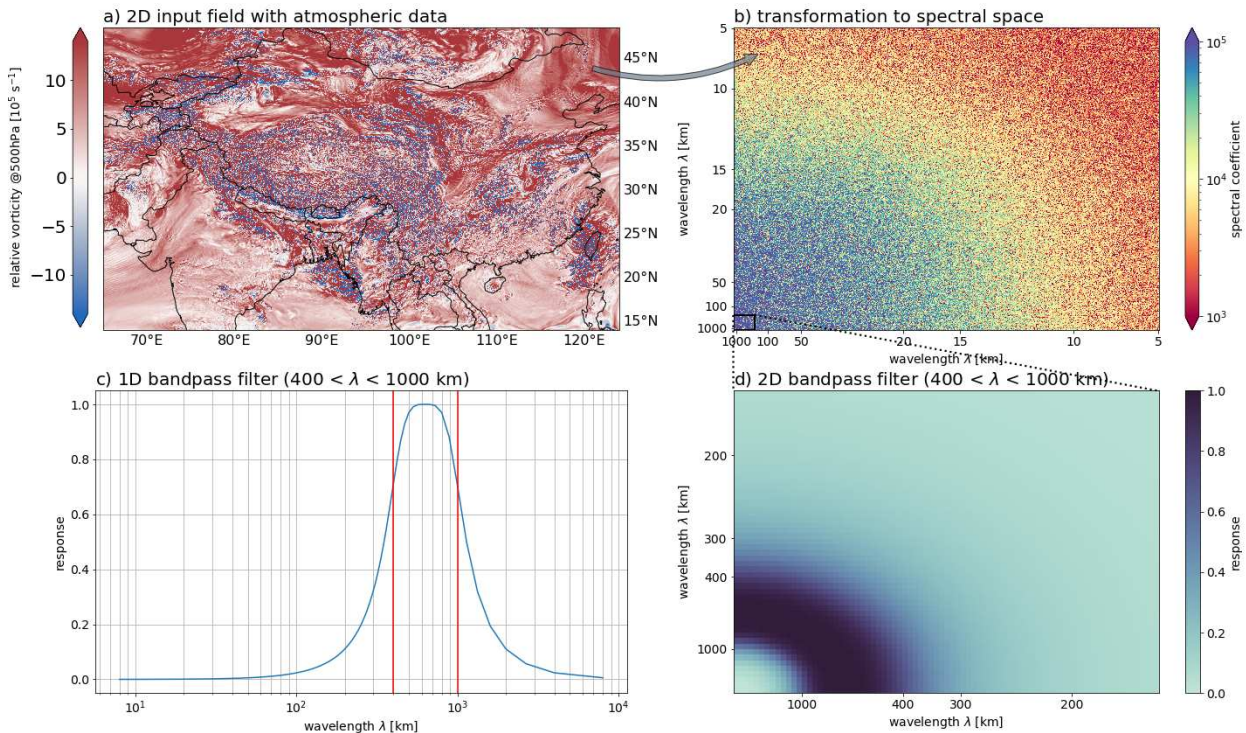


Figure 3.6: Visualization of spectral decomposition of atmospheric input fields and construction of a bandpass filter that can be specified by the user and is used to filter the input data. a) 2D input field with atmospheric data at one time step, here: hourly relative vorticity at 500 hPa [ $10^5 \text{ s}^{-1}$ ] of a 4km WRF simulation over South East Asia. b) The same data after the DCT, represented by spectral coefficients as a function of wavelengths in x and y direction. c) 1D bandpass filter response curve. d) 2D bandpass filter response as a function of wavelength in x and y directions.

Response of constructed bandpass filter as a function of wavelength. The two red lines indicate the cut-off wavelengths that can be specified by the user (here: 400 and 1000 km). d) Same bandpass filter but in 2D spectral domain with same shape as b) but zoomed in to show the filter response for wavelengths between 400 and 1000 km.

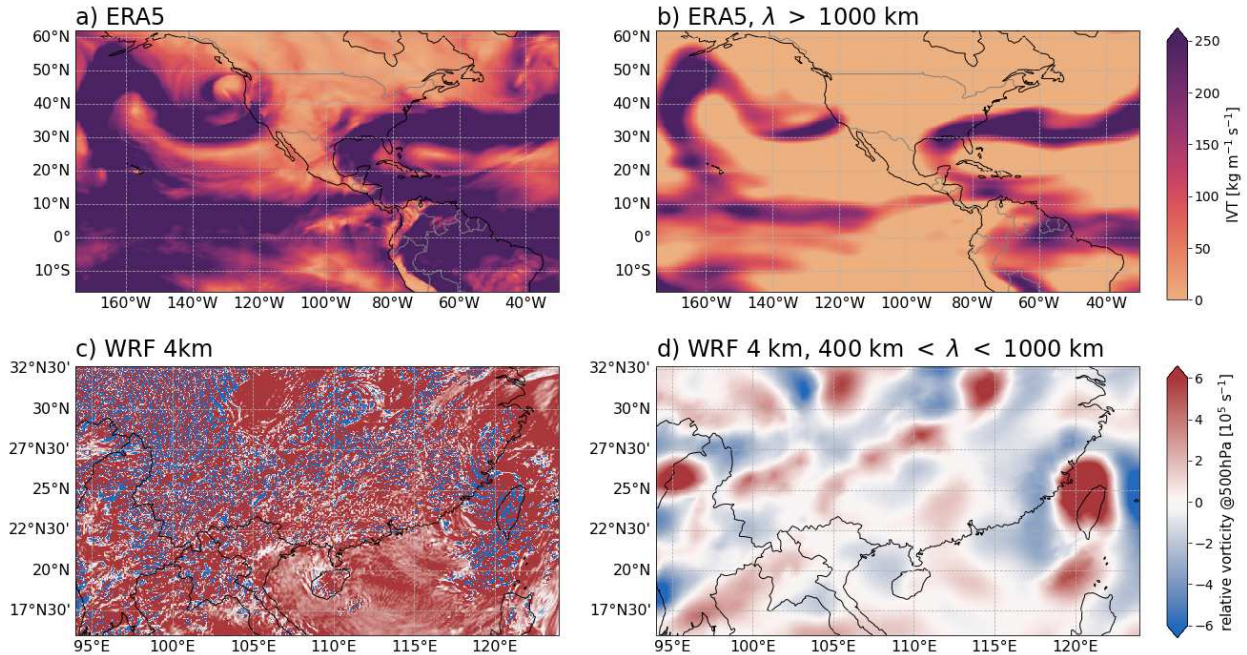


Figure 3.7: Examples for hourly atmospheric input fields (a, c) and their corresponding spectrally filtered fields (b, d). a) Vertically integrated water vapor transport (IVT) [ $\text{kg m}^{-1} \text{s}^{-1}$ ] from ERA5 at 2021-01-27 10:00:00 UTC showing an atmospheric river over the San Francisco Bay area b) Same as in a) but spectrally filtered for wavelengths  $> 1000$  km, c) Relative vorticity at 500 hPa [ $10^5 \text{ s}^{-2}$ ] from a WRF simulation with 4km grid spacing over Southeast Asia for 2008-07-18 05:00:00 UTC (when Typhoon Kalmaegi hit Taiwan) d) Same as in c) but spectrally filtered for wavelengths between 400 and 1000 km. Note that the typhoon over Taiwan only becomes visible in the vorticity field after the filtering has been applied, because the original vorticity field is dominated by sub-mesoscale noise.

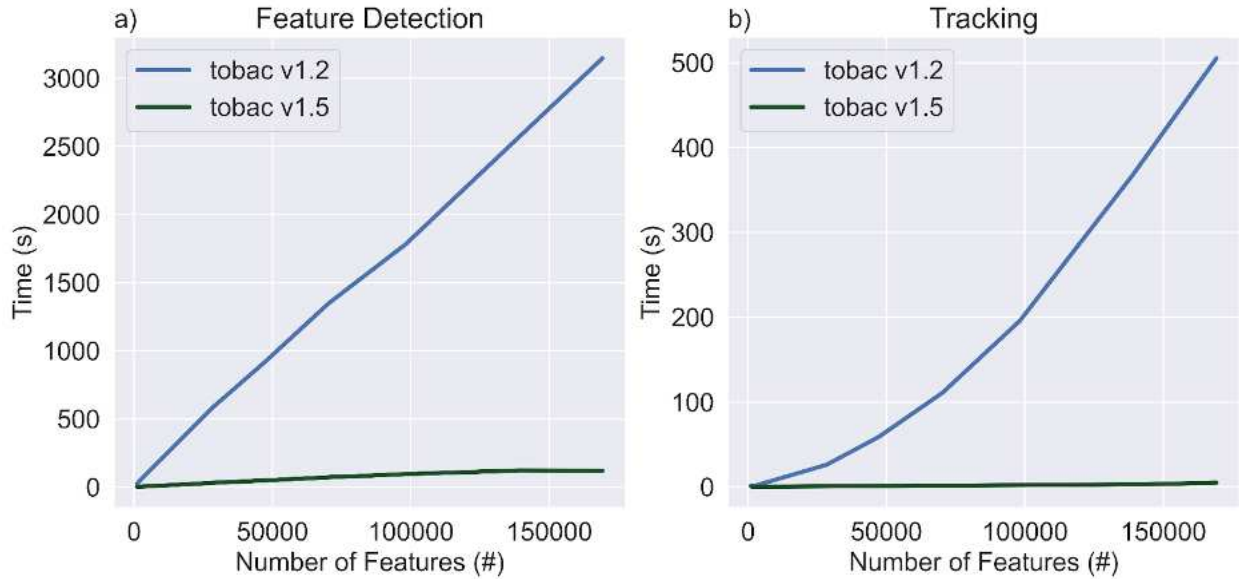


Figure 3.8: A benchmark comparison of *tobac* speed between version 1.2 (Heikenfeld et al. 2019) and version 1.5, demonstrating the increase in speed using a full day of GOES-16 Channel 10 IR imagery from 12 June 2021 on a) feature detection at 230 K, with number of features on the abscissa and time taken to run feature detection on the ordinate, and b) as in a, but for tracking.

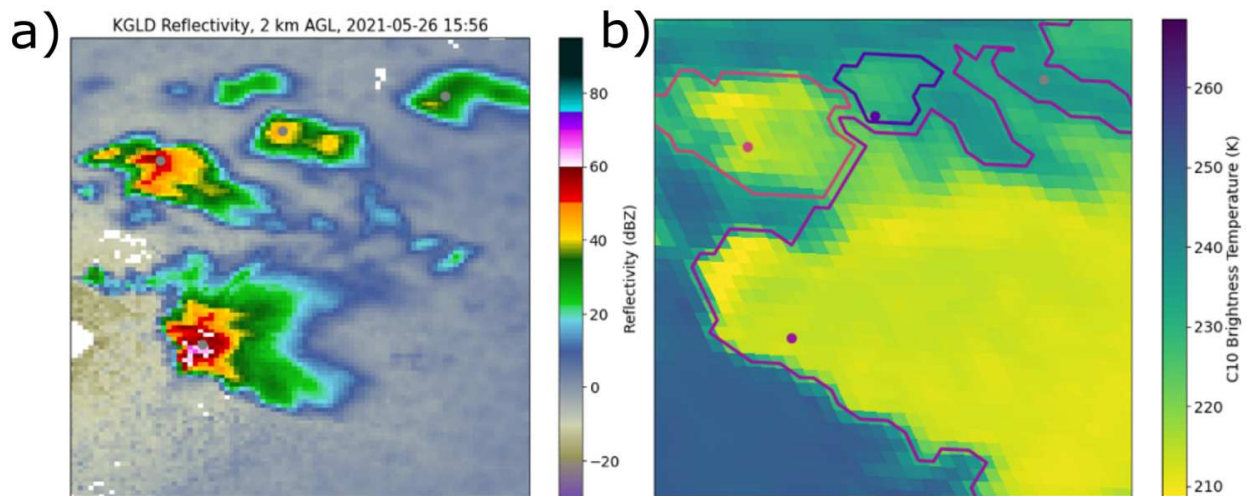


Figure 3.9: A depiction of the output from the new procedure for differently gridded data included in *tobac* v1.5. Panel (a) shows NEXRAD radar reflectivity in dBZ from the Goodland, KS site at 15:56 UTC on 26 May 2021, as well as the associated features detected at a 30 dBZ threshold marked by grey dots which represent different convective cores. Panel (b) shows GOES-16 satellite observed brightness temperature in K (initially on a different grid from the radar data), as well as the segmentation masks associated with each of these features as differently coloured outlines. The segmentation outlines shown in panel (b) are produced after regriding the satellite data to the same grid as the radar data and depict the upper-level cirrus shields associated with the different convective cores seen in the radar data.

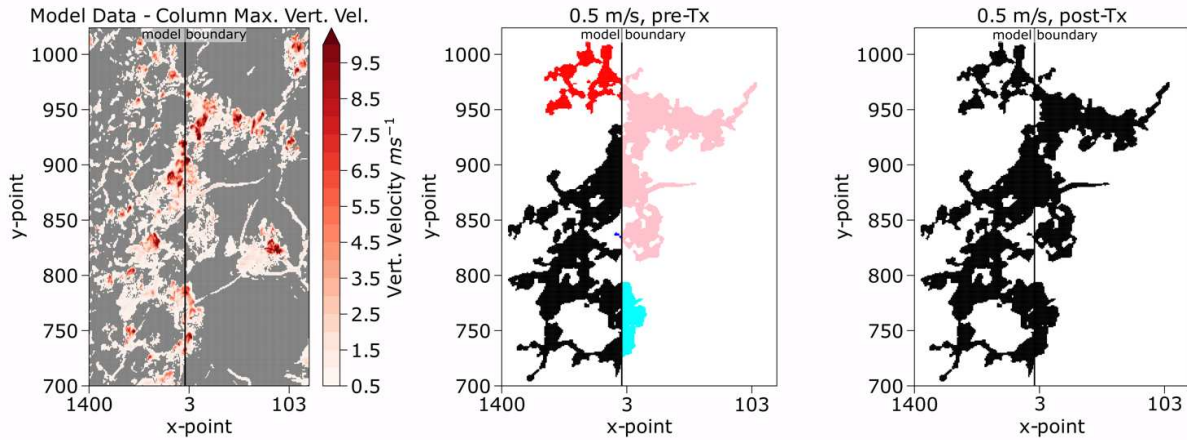


Figure 3.10: Illustration of PBC treatment algorithm for feature detection. Panel (a) shows the original column-maximum vertical velocity field (values less than  $0.5 \text{ m s}^{-1}$  masked); (b) depicts the six individual feature detection labels produced at a  $0.5 \text{ m s}^{-1}$  threshold without the PBC treatment; and (c) presents the correct unified label post-treatment for PBCs.

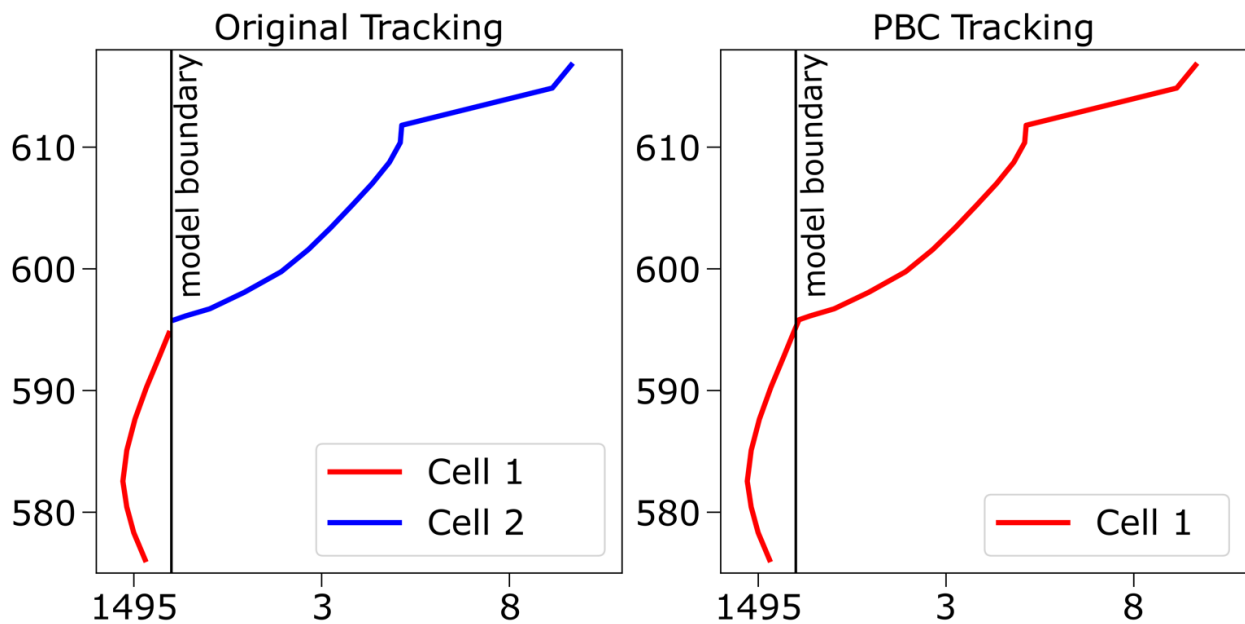


Figure 3.11: A depiction of 2D *tobac* tracking with and without accounting for PBCs. Panel (a) shows the two discrete cells that would be identified by *tobac* v1.2 when a feature crosses a boundary; panel (b) illustrates the single, unified cell that is produced with the PBC tracking procedure.

## **CHAPTER 4: DYNAMIC AND THERMODYNAMIC ENVIRONMENTAL MODULATION OF TROPICAL CONGESTUS AND CUMULONIMBUS IN THE MARITIME CONTINENT**

### **4.1. Introduction**

The Maritime Continent (MC) has long been identified as a region vital to the global energy and water balance (Riehl and Malkus 1958; Ramage 1968). The role of the MC in the climate system is, in turn, influenced by cumulus, congestus, and cumulonimbus clouds, the three modes comprising tropical convection (Johnson et al. 1999). Because of the important role of the MC in the climate system and its wide variety of convective morphologies, it is an excellent natural laboratory to study convective cloud processes. Here we focus on congestus and towering cumulonimbus, or together Congestus and Cumulonimbus Clouds (CCCs), as they are crucial for vertically transporting momentum, energy, water, trace gases, and aerosol particles between the boundary layer and upper troposphere (Riehl and Malkus 1958; Ramage 1968; Dickerson et al. 1987; Su et al. 2006; Barth et al. 2015). CCCs are also vital contributors to the atmospheric radiative balance through anvil radiative forcing (Slingo and Slingo 1988), are critical to driving the large-scale atmospheric circulation (Riehl and Malkus 1958), and influence inter- and intraseasonal oscillations (Riley et al. 2011; Zuluaga and Houze 2013; Riley Dellaripa et al. 2018; Toms et al. 2020a,b). Storm environments, including their thermodynamic, dynamic (e.g., shear and convergence), and aerosol properties, may have significant impacts on elements of CCC lifecycle, e.g., development, maintenance, and dissipation (e.g., Austin 1947; Bhat et al. 1996; Holloway and Neelin 2009; Masunaga 2013; Bergemann and Jakob 2016; Posselt et al. 2019). However, the relationship between CCC properties and their formation environments is still not well-understood. Indeed, convective parameterizations in global and regional climate

models have often struggled to accurately represent the interactions between CCCs and their environment, particularly within the MC (Neale and Slingo 2003; Jourdain et al. 2013).

The overarching goal of this research is to investigate the influence that local initial environmental characteristics have on the properties and lifetimes of tropical CCCs. Previous work has examined the sensitivity of CCC properties in the tropics to environmental characteristics through both observational (Holloway and Neelin 2009, 2010; Tobin et al. 2012; Kumar et al. 2014; de Oliveira and Oyama 2015; Schiro et al. 2016; Louf et al. 2019) and numerical modeling studies (Grabowski and Moncreiff 2004; Jensen and Del Genio 2006; Takemi 2007a,b, 2014, 2015; Hannah 2017; Posselt et al. 2019; Storer and Posselt 2019; Grant et al. 2020; Toms et al. 2020b; Chen et al. 2021). Each of these studies has related several properties of CCCs, such as cloud top height or precipitation rate, to environmental characteristics, such as Convective Available Potential Energy (CAPE), vertical wind shear, and humidity.

Prior observational approaches have typically allowed for the simultaneous sampling of many convective cloud modes and assessing the large-scale environments supporting their formation. For example, Louf et al. (2019) used a long-duration ground-based radar dataset to examine the response of monsoonal convective clouds to changes in the bulk environment, and found that rainfall is sensitive to CAPE, Convective INhibition (CIN), humidity, and large-scale ascent. However, while Louf et al. (2019) examined large-scale environmental controls that are instructive for climate models, they did not sample the local environments responsible for the initiation, organization, and evolution of individual CCC entities. Similar limitations are also present in other observational work focused on this problem (Holloway and Neelin 2009, 2010; Tobin et al. 2012; Kumar et al. 2014; de Oliveira and Oyama 2015; Schiro et al. 2016), and are a

natural result of the resolution and associated shortfalls of remote sensors in characterizing local thermodynamic and dynamic environments of CCCs.

Numerical modeling studies, on the other hand, can sample the initial environments responsible for individual cloud systems. Such modeling studies have typically examined a single storm or collections of storms while systematically varying the local environmental conditions such as CAPE, humidity, vertical wind shear and aerosols (Grabowski and Moncreiff 2004; Grabowski 2006; Jensen and Del Genio 2006; Takemi 2007a,b, 2010; Kirkpatrick et al. 2011; van den Heever et al. 2011; Storer and van den Heever 2013; Takemi 2014; Hannah 2017; Posselt et al. 2019; Storer and Posselt 2019; Grant et al. 2020; Park et al. 2020). However, even when previous studies have applied realistic perturbations, they have not necessarily spanned the full range of observed convective environments and morphologies, nor have they taken into account the relationships between large-scale and local conditions in influencing CCC lifecycle.

There has been some work combining the strength of the observational approach—the ability to sample storms in the natural environment—with numerical models, which allow formation environments and storm properties to be sampled throughout the domain at high resolution (Takemi 2015; Toms et al. 2020b). However, both of these studies focused on the role of the *large-scale* environments alone, such as the Boreal Summer Intraseasonal Oscillation influences on CCC properties (and vice-versa in the case of Toms et al. 2020b), rather than on the role played by the local initial environment within the context of the large-scale environment. Few, if any, existing studies have examined how *local* initial environmental characteristics influence CCC properties throughout CCC lifetimes. This is particularly important when trying to determine why the storm strength, storm organization and storm orientations of various CCCs vary when contained within the same large-scale environment.

To elucidate robust relationships between local environmental characteristics and storm properties, we need a statistically significant sample of convective clouds developing under a wide range of realistic environments and environmental perturbations. Here we employ an approach in which the simulation is initialized using observational conditions and the local cloud environments are allowed to develop naturally and heterogeneously, as with observational studies. This approach enables an assessment of the relationship between individual CCC storm properties and their *local* initial environment characteristics. We make use of a high-resolution, large-domain simulation that is allowed to evolve over a long time period, resulting in millions of CCCs, each formed by different local initial environments. Each simulated CCC in the model output is identified and tracked in time using a convective tracking algorithm. We then determine both the initial environmental characteristics and the temporally evolving CCC properties for each simulated CCC.

This research quantifies the initial thermodynamic and dynamic environmental influences on the following properties of CCCs: (a) convective intensity (updraft strength and precipitation rates); (b) storm organization (cloud adjacency); and (c) storm morphology (linear or non-linear). The definitions and requirements for these properties are further clarified in Section 4.3. Throughout this paper we will refer to these three aspects of CCCs as the *storm properties*. The immense dataset of simulated CCCs in their naturally evolving simulated environments allows for the creation of a robust statistical profile of the relationship between initial environmental characteristics and CCC properties over their lifetimes.

## **4.2. Numerical Model and Experiment Setup**

The Regional Atmospheric Modeling System (RAMS; Cotton et al. 2003; Saleeby and van den Heever 2013) version 6.2.14 was employed to conduct the numerical experiments. RAMS

has been widely used to model tropical deep convection and has been shown to produce a realistic depiction of these tropical convective properties (van den Heever et al. 2011; McGee and van den Heever 2014; Storer and Posselt 2019; Toms et al. 2020a,b; Grant et al. 2020). We performed a month-long simulation over a domain of 1800 x 1950 km at a horizontal grid spacing of 1km and vertical grid spacing of 100 to 300m, with frequent temporal output ( $\Delta t_{output}=5$  mins). This large-domain, high-resolution, long-duration simulation produced robust statistics of CCC lifecycle for nearly two hundred thousand individually resolved CCCs. Full model simulation and parameterization configuration information is provided in Table 4.1, but some of the more critical parameters are now described in more detail. The model simulation period extended from 15 August 2019 to 20 September 2019 and was approximately spatially and temporally coincident with the Southwest Monsoon period of the NASA Cloud, Aerosol and Monsoon Processes Philippines Experiment (CAMP<sup>2</sup>Ex; Reid et al. 2022) field campaign. CAMP<sup>2</sup>Ex made extensive observations of clouds, convection, and environments around the Philippines. The potential for future comparisons of this modeled dataset with the observations made in the field was one of the primary reasons for selecting this period and geographic region. Our model grid was centered on the Philippine Archipelago (Figure 4.1a), and a wide range of convective morphology, typical of the MC, was captured in these simulations (Figure 4.1b,c).

To ensure the large-scale environments in our simulation were representative of those in the MC region, we nudged the lateral boundaries with the ERA-5 reanalysis dataset (Hersbach et al. 2020). As we did not nudge the center of the domain, we do expect some drift from the observations in time on the mesoscale. Initial assessments of the model output show that the modes of convection produced closely match those typically found in this environment (Figure

4.1b), and that the large-scale and synoptic-scale features realistically transited the domain during the simulation (not shown). A similar result was found in Toms et al. (2020b).

### 4.3 CCC Identification and Tracking

We employed a modified version of the Tracking and Object-Based Analysis of Clouds (*tobac*) algorithm v1.2 (Heikenfeld et al. 2019; Chapter 3) to track 200,000 CCCs, including the storm properties and the surrounding environmental characteristics at 5-minute intervals throughout the CCC lifecycle. *tobac* is a comprehensive framework capable of identifying cloud features and volumes and tracking clouds over time.

#### *a. Tracking Step 1: CCC Feature Identification*

To track CCCs and calculate their properties, we first began by identifying two-dimensional cloud features. We used the mid-level (3-8 km) maximum updrafts (hereafter  $W_{\max}$ ) to identify convective features. A minimum  $W_{\max}$  of  $1 \text{ m s}^{-1}$  was used as our threshold for tracking CCCs. This threshold is lower than that of the continental cloud study of Heikenfeld et al. (2019) as tropical marine convection typically has weaker mid-level updrafts (Zipser and Lemone 1980).

Figure 4.2a and b demonstrate the ability of *tobac*'s feature identification algorithm to simultaneously identify hundreds of updrafts and updraft clusters, respectively, across the simulation domain at each point in time. The selection of a single feature point from a 2D field of vertical velocity by *tobac* is detailed in Heikenfeld et al. (2019), and an example of this for isolated convection is demonstrated in Figure 4.2c. Each updraft in these examples had only one identified feature, namely the the maximum updraft velocity, as indicated by the dots. From this, each CCC's  $W_{\max}$  was logged. Our feature identification required storms to have a positive  $W_{\max}$ . This requirement did, at times, result in some dissipating CCCs not being identified and tracked.

However, as the developing and mature phases of the CCCs were identified using this technique, their initial environments can be derived, and most of their lifecycle is trackable. This approach differs from those that rely on precipitation for storm identification and/or tracking in which the early storm lifecycle is often missed due to the time it takes to produce precipitation.

*b. Tracking Step 2: Full-cloud volume segmentation*

As CCCs are 3D phenomena, using only a single point or column measurement to identify each CCC would unrealistically depict storm properties and processes. Instead, we used *tobac*'s segmentation component, which utilizes a 3D watershedding algorithm to associate cloudy grid points with the updraft feature detected in Step 1. In keeping with Heikenfeld et al. (2019), the watershedding algorithm used the 3D total condensate field with a minimum threshold of 0.5 g kg<sup>-1</sup> to determine what we classify as cloudy and non-cloudy points.

Figure 4.2d depicts an example produced by this algorithm at a single vertical level at a single time. In this figure, the updraft features (dots; identical to those in the other panels of Figure 4.2) are shown within each of their separately detected cloud segments (various contoured colors in the background). Rather than being limited to a simple radius or column around the singular detected feature point (maximum midlevel updraft velocity in this case), the entire cloud volume was determined for each CCC from which cloud statistics were then calculated.

*c. Tracking Step 3: CCC Tracking*

Each of the feature detection (Tracking Step 1) and segmentation steps (Tracking Step 2) was performed at every output time of the simulation (i.e., every 5 min). To track the identified features, we used the *trackpy* (Allan et al. 2021) integration in *tobac* (Heikenfeld et al. 2019). Storm splitting and merging were treated as follows. Features that merged at time  $t + \Delta t_{\text{output}}$  were linked to the feature at time  $t$  that had the direction of travel most similar to the initial feature.

Similarly, for storms that split, the feature at time  $t + \Delta t_{\text{output}}$  closest to the predicted position was linked to the original feature at time  $t$ , and the feature further away from the predicted track was identified as a new feature. Storm tracking was performed throughout the analysis period of 30 days.

Some of the initially tracked storms were removed as part of a quality control process. First, we eliminated all tracked CCCs from the database that were within the lateral boundary nudging zone at any point in their lifetime. Next, we removed tracked storms that initiated or passed over land to prevent terrain effects from complicating the analysis of what are primarily maritime convective storms. This resulted in a database of storms comprised entirely of a maritime lifecycle. Finally, we deleted all tracked storms with lifetimes less than 15 minutes, as we would expect the minimum storm lifetime for deep convection in the maritime continent to be at least 20 minutes (Toms et al. 2020b). We saw no substantive difference in our results (other than the number of storms tracked) when mandating a 10 or 20-minute maximum storm time, and thus the selection of this threshold does not appear to impact the results. After these quality control steps were performed, our tracked CCC database consisted of 182,149 tracked convective storms.

#### *d. Determining CCC Properties*

We next characterized the CCC properties of interest (i.e., intensity, organization, and morphology) for each CCC in our database. Although many metrics could be used to quantify CCC properties, we selected a specific metric to facilitate the automated identification. For example, the term “intensity” can have many different definitions depending on the context, including updraft strength (Zipser and Lutz 1994), lightning flash rate (Fuchs et al. 2015), the height of specific radar reflectivities (Zipser et al. 2006), or precipitation rates (Cecil et al. 2005).

We selected both updraft strength and precipitation rates as metrics for CCC intensity. We used the maximum mid-level (3 to 8 km) vertical velocity over the tracked lifetime of the CCC for the updraft intensity. This is the same quantity used by *tobac* to identify features and is therefore intimately tied to our tracking. An example of characterizing CCC updraft intensity is included in Figure 4.2a and c, which show tracked *tobac* features colored by their maximum midlevel updraft. For storm precipitation intensity, we used the maximum precipitation rate of the CCC at the surface over its tracked lifetime. Calculating the total integrated precipitation amount for each individual storm was not possible because *tobac* relies on an updraft of at least 1 m/s to track the storm feature. As such, precipitation that falls during a storm's dissipating phase (in which updrafts may be weak to non-existent) will not be counted in the total. To calculate the precipitation rate for a single CCC, we sampled only those points included in *tobac*'s segmentation on the model level nearest the surface and stored the maximum precipitation rate from all points within this segmented area over the lifecycle of the CCC. As *tobac* did not necessarily capture the end of each CCC lifecycle, we may not have captured the strongest precipitation rates if they occurred in the dissipating phase.

For storm organization, we chose to classify any two CCCs as organized if their *tobac*-determined cloud segmentations were adjacent at any vertical level at any time during their lifetime. Similar distance-based metrics for determining convective organization have been previously used in the literature (Tobin et al. 2012; White et al. 2018). White et al. (2018)'s approach to describing convective organization is conceptually similar to what we use here, labeling individual convective cores as part of a larger organized system if they have adjacent clouds.

Figure 4.2d demonstrates how this algorithm identifies organized storms. The background shading of this plot indicates various segmentation areas, with each different color representing a different CCC segmented area at 2 km AGL. Overlaid on the segmentation horizontal cross-section are identified CCC features, whose locations match those in Figure 4.2c, but are colored by their organizational status. The three CCCs identified by points colored green are considered part of the same storm system (i.e., Cluster 1) and are therefore organized, and the two CCCs that are colored blue are considered part of their own, also clustered, system (i.e., Cluster 2), whereas each of the features colored black are considered separate Isolated CCCs. It is worth noting that the segmented area denoted by the grey feature in the center of the domain is not touching the brown segmented area, despite the fact that they are identified as part of the same convective cluster. While they are not touching at this level, the two segmentations do touch at several other levels higher up in the atmosphere (not shown), demonstrating that this approach works in a 3D perspective. If a CCC was identified as part of a storm cluster at any point in its lifetime, it was labeled as a Clustered storm point, whereas only tracked storms that were never part of a larger system were labeled as Isolated. The result of applying this algorithm is shown in Figure 4.2b, where the colored points are considered Clustered and the black points Isolated.

Finally, we used linearity to quantify the morphology property of CCCs. Only those CCCs that were already classified as organized were considered. Linearity was quantified by the aspect ratio of the minimum bounding rectangle, where the latter was defined as the smallest rectangle that can encompass all detected CCCs that were part of a single organized complex at any one time. This objective requirement is somewhat similar to the subjective definitions of linearity present in the existing literature in which linearity in the convective elements is required

rather than in the entire cloud field (Parker and Johnson 2000, Gallus et al. 2008). If the minimum bounding rectangle had an aspect ratio of at least 3:1, meaning its two longer sides were at least three times as long as its two shorter sides, the storm morphology was considered Linear at that time; otherwise, we classified it as Nonlinear. Although our selection of the 3:1 ratio was somewhat arbitrary, we tested ratios between 1.5:1 and 10:1 and found the trends to be insensitive to these specifications. As storm clusters change over time, they may move from a Linear to a Nonlinear morphology or vice versa. We required that a storm be Nonlinear or Linear for at least 75% of its lifetime for it to be classified as such.

*e. Determining CCC Environmental Properties*

All of the storm properties need to be related to unique CCC formation environments in order for us to answer our science question. To determine the CCC formation environments we began by identifying the point at which the CCCs are first tracked by *tobac*. At this point, the storm already had a  $W_{\max}$  of at least  $1 \text{ m s}^{-1}$ , meaning that the environment is not necessarily exactly representative of the storm's initial formative environment. Instead, we sampled the environment 5 minutes (i.e., one  $\Delta t_{\text{output}}$ ) before the first CCC updraft is detected (i.e., 5 minutes before the storm has an updraft of at least  $1 \text{ m s}^{-1}$ ). As we do not have any previous tracking information before the CCC is first detected, we must determine a spatial point or set of points to sample the prior environment. Here, we choose to sample the environment by taking the mean of the environment falling within a circle of 5km radius around the point of first updraft identification. All of the points with a total condensate amount  $>0.1 \text{ g kg}^{-1}$  are excluded to ensure that we are sampling the cloud-free environment, and a minimum of 5 cloud-free points per level was required to calculate a valid environment. Our results were not sensitive to the radius threshold when tested between 5 and 15 km surrounding the point or the temporal

threshold, and when tested between 5 and 15 minutes before initial storm identification. The initial environments were calculated in this manner for each individual CCC in the database.

Throughout this work, we also employed scalar environmental parameters that were derived from the mean vertical environmental profiles discussed above. Convective Available Potential Energy (CAPE, here using surface-based CAPE) and precipitable water were calculated by the MetPy v1.0 library (May et al. 2020). The vertical wind shear values were determined by first calculating the mean wind profile for each CCC as described above and then calculating the vertical wind shear as a vector magnitude shear (e.g.,  $\sqrt{(u_{z\ km} - u_{sfc})^2 + (v_{z\ km} - v_{sfc})^2}$  for the 0-Z km vertical wind shear, where Z can be any altitude). Where wind shear is reported separately as directional and speed shear, these are calculated for directional as (using 0-1 km as an example)  $|\circ_{1km} - \circ_{sfc}|$ , where  $\circ$  represents the wind direction in degrees, and for speed shear as  $|\vec{V}_{1km}| - |\vec{V}_{sfc}|$ , where  $|\vec{V}|$  represents the wind speed in  $\text{m s}^{-1}$  (Markowski and Richardson 2006). Means and standard deviations of these scalar storm environment parameters were computed by determining the scalar parameter for each individual initial environment and then calculating the arithmetic mean or standard deviation. Owing to the large dataset of CCCs used here, the environment calculations were performed using the *jug* python library (Coelho 2017). Where statistical significance is discussed, we employ the student's t-test at an  $\alpha = 0.01$  to determine whether two means were statistically significantly different.

Maximum values of the CCC properties (e.g., maximum cloud top height) are assessed by determining the maximum value throughout a single CCC tracked lifetime unless otherwise noted. Vertical microphysical profiles are calculated for each CCC and time by taking the mean vertical profile within the CCC using the *tobac*-derived segmentation data. Each CCC is assigned a time-averaged mean vertical profile for each of the eight microphysical mixing ratios. The

overall means are calculated by taking the arithmetic mean of all CCC time-averaged mean vertical profiles in the bin of interest. Vertical velocity Contoured Frequency by Altitude Diagrams (CFADs; Yuter and Houze 1995) are calculated based on the total frequency of vertical velocities over all CCCs in the bin using a bin width of  $0.2 \text{ m s}^{-1}$ , and discarding the vertical velocities between  $-0.2$  and  $0.2 \text{ m s}^{-1}$ .

#### **4.4. Results**

Various bulk characteristics of our full tracking dataset of 182,149 CCCs are summarized in Figure 4.3. The number of CCCs varied over time with changing synoptic conditions (Figure 4.3a). The strength and depth of the CCCs also varied. Figure 4.3b shows a histogram of the maximum vertical velocity over the CCC's lifetime. Although there is no comprehensive observational dataset of updraft vertical velocities over this region, the range of storm maximum vertical velocity simulated in our deep convective storms is largely in line with other numerical simulations of tropical deep convection (van den Heever et al. 2011; Hannah 2017; Posselt et al. 2019; Storer and Posselt 2019; Grant et al. 2020).

Our suite of tracked storms also varies in the maximum cloud top height reached by the CCCs over their lifetime (Figure 4.3c). As we require the presence of an updraft between 3-8 km, our tracked maximum cloud top height distribution begins above 3 km AGL (Figure 4.3c). The distribution is bimodal, with peaks around 6 km and 15 km AGL, and a relative minimum between 8-13 km AGL. The bimodality indicates that we are capturing terminal congestus, whose cloud tops are typically found around just above the freezing level inversion ( $\sim 5$  km in the tropical summer MC; Johnson et al. 1999) and towering cumulonimbus, which continue past the freezing level, typically topping out around the equilibrium level.

#### *a. Convective Environments associated with Storm Intensity*

Our science question first asks about the impacts of the environment on storm intensity. To this end, we have stratified our tracked database of CCCs into three bins for each of the vertical velocity and precipitation metrics we are using to define intensity. First, for vertical velocity, we divide the dataset into velocity bins and define  $St\_W$  (CCCs with  $W_{\max} \geq 10 \text{ m s}^{-1}$ ),  $Md\_W$  (CCCs with  $10 > W_{\max} \geq 5 \text{ m s}^{-1}$ ), and  $Wk\_W$  (CCCs with  $5 > W_{\max} \geq 1 \text{ m s}^{-1}$ ). For precipitation intensity, we have stratified the dataset based on percentiles of the maximum precipitation rate sampled:  $St\_PCP$  ( $\geq 66^{\text{th}}$  percentile),  $Md\_PCP$  ( $66^{\text{th}}$  to  $33^{\text{rd}}$  percentile), and  $Wk\_PCP$  ( $\leq 33^{\text{rd}}$  percentile). It is important to note that the storm updraft intensity bins and the precipitation intensity bins are not the same, and that CCCs in the  $St\_W$  bin are not necessarily the same as those in the  $St\_PCP$  bin and vice versa, i.e., the strongest storms dynamically do not necessarily produce the heaviest precipitation, and the heaviest precipitation is not necessarily produced by the strongest dynamical storms. A further exploration of the overlap between the precipitation and vertical velocity bins is discussed in Section 4.4.a.2.

##### *4.4.a.1 Storm Updraft Intensity*

The three bins of updraft intensity approximately represent two of the classifications of moderate-to-deep convection cloud top height (Johnson et al. 1999) in the MC: cumulonimbus (i.e., the  $St\_W$  and most  $Md\_W$  CCCs) and terminal cumulus congestus (i.e., the  $Wk\_W$  CCCs; Figure 4.4a). The  $St\_W$  CCCs nearly all have maximum cloud tops substantially higher than the freezing level inversion ( $\sim 5 \text{ km AGL}$ ), whereas the  $Wk\_W$  CCCs almost all have cloud tops around or below the freezing level. In keeping with previous findings (LeMone et al. 1998; Johnson et al. 1999; Luo et al. 2009; Sheffield et al. 2015), this suggests that the latent heat of glaciation is an important contributor to the vast majority of  $Md\_W$  and  $St\_W$  CCCs throughout

the MC. Figure 4.4b shows the mean hydrometeor vertical profiles by vertical velocity and indicates that there is more latent heating from condensation, freezing, and deposition (as indicated by the larger ice and liquid hydrometeor average mixing ratios) in *St\_W* CCCs than in the *Md\_W* and *Wk\_W* CCCs. While the total amount of both ice and liquid monotonically increases with increasing storm  $W_{\max}$ , the ratio of ice to total condensate stays approximately the same in all three vertical velocity bins. It is noteworthy that in the areas above the freezing level (~6 km), the sample sizes for *Wk\_W* are relatively small as few of these CCCs reach this cloud top height. The differences between in-cloud properties that are coincident with the three  $W_{\max}$  bins help to explain why  $W_{\max}$  varies, but these properties are all modulated by initial environments, which we now explore.

Diversity in cloud properties, especially around some congestus remaining terminal and some continuing to develop into cumulonimbus suggest that there are environmental factors influencing the storm lifecycle. Figure 4.5 demonstrates the mean difference between the initial thermodynamic environments in the three storm  $W_{\max}$  bins. The *St\_W* environments are on average both warmer and moister than both the *Md\_W* and *Wk\_W* CCCs at the surface (as demonstrated by the plotted change in temperature versus the *Wk\_W* bin), and are colder aloft (i.e., above 550 hPa; Figure 4.5a). While the *St\_W* and *Md\_W* CCCs are generally moister than the *Wk\_W* CCCs below 250 hPa, this trend is not monotonic, as *Md\_W* CCCs are overall moister than *St\_W* CCCs above 700 hPa (Figure 4.5c). Given that the trend in column integrated moisture is monotonic, with the *St\_W* CCCs having higher precipitable water on average than *Md\_W* CCCs (Figure 4.6b; Table 4.2), the enhanced moisture near the surface in *St\_W* is enough to compensate for its relatively lower moisture above 700 hPa. It is possible that this overall increase in moisture above 700 hPa in the *Md\_W* CCCs relative to the *St\_W* CCCs could be a

signal that *St\_W* CCCs are more robust to dry layers aloft, whereas the *Md\_W* CCCs are more sensitive to such layers, requiring more moisture throughout the initial column to survive.

The differences in temperature and low-level moisture result in a statistically significant increase in mean CAPE in the *St\_W* (mean CAPE 1802.8 J kg<sup>-1</sup>) versus *Md\_W* (1550.9 J kg<sup>-1</sup>) and *Wk\_W* (1489.7 J kg<sup>-1</sup>) CCCs (Table 4.2; Figure 4.6a). While larger CAPE values will inherently lead to an increase in vertical velocity, CAPE is not the sole discriminator in CCC strength. In fact, the *Md\_W* and *Wk\_W* storm mean CAPE values are quite similar (Table 4.2; Figure 4.6a). This suggests that relatively high CAPE is a necessary but not sufficient condition for strong CCC updraft velocities in the MC.

As higher CAPE alone is not the discriminator between CCC updraft intensity, it is necessary to explore other environmental controls. Above the surface, the moisture content of the air will also impact the updraft velocity through entrainment and subsequent mixing. Some of these impacts can be seen in Figure 4.6b and Figure 4.7b-c. *St\_W* CCC initial environments have similar column moisture to their *Md\_W* counterparts, but more column moisture on average (Figure 4.6b; Table 4.2) than their *Wk\_W* counterparts. Thus, the *Md\_W* CCCs have significantly less CAPE but similar PW to the *St\_W* CCCs, and similar CAPE but more PW than the *Wk\_W* CCCs, suggesting that the PW plays a more significant role than CAPE in determining storm intensity. Even in high CAPE (>2000 J kg<sup>-1</sup>) situations, if the environment is drier (<63 mm precipitable water), it is more likely that a *Wk\_W* CCC will form rather than a *St\_W* CCC (Figure 4.7b). Further, we can see from Figure 4.6b that half of all *St\_W* CCCs had initial precipitable water values above 64 mm, with three quarters of them above 63 mm. CCCs with stronger  $W_{\max}$  require more moist environments in the lower levels (i.e., lower than 650 hPa) because when relatively dry environmental air is entrained into the storm, condensation and deposition rates

decrease resulting in less latent heating and reduced buoyancy. Furthermore, moist air is more buoyant than dry air. That said, sufficiently moist environments appear to be necessary but not sufficient conditions for the formation of intense CCCs; without the necessary CAPE (i.e., below  $\sim 1500 \text{ J kg}^{-1}$ ), it is more likely that a *Wk\_W* storm forms than a *St\_W* storm for all PW amounts (Figure 4.7b).

CAPE and precipitable water both describe the thermodynamic state of the air entrained into growing CCCs, but does not directly describe the dynamical state. Deep layer vertical wind shear, to first order, increases entrainment (Hannah 2017; Peters et al. 2020). The impact of deep layer vertical wind shear is evident in Figure 4.6e-f, where it can be seen that increases in the average environmental 0-5 km and 2-7 km vector magnitude wind shear are associated with weaker storm updraft velocities. However, this trend reverses when considering the impacts of the 0-1 km and 0-3 km shear (Figure 4.6c-d). We speculate that this may be because weak and moderate storms that are more sheared in the lower levels never fully develop and instead either remain below the 3 km height threshold for detection or never develop into cumulus clouds to begin with.

The interplay between CAPE and shear can be further seen in Figure 4.7a, which shows the relationship between lower level (0-3 km) wind shear and CAPE. Although strong values of wind shear ( $> 10 \text{ m s}^{-1}$ ) are less common, for sufficient CAPE, *St\_W* CCCs are more likely at stronger lower-level wind shear values. The distribution within the CAPE-shear phase space closely mirrors that of the CAPE-PW phase space, albeit with more *Wk\_W* CCCs than *St\_W* CCCs in the high CAPE/high shear zone (top right). When examining precipitable water and 0-3 km wind shear simultaneously (Figure 4.7c), we see a less coherent relationship, with low shear and low precipitable water resulting in more frequent *Wk\_W* CCCs. This further reinforces that,

as long as wind shear is not so strong that it is causing initial convection to terminate due to excessive entrainment, it is not as strong a control of vertical velocity as the initial CAPE and precipitable water. The strong dependence of CCC vertical velocity on CAPE and precipitable water and the relatively weak dependence on wind shear has also been previously reported (Posselt et al. 2019; Storer and Posselt 2019). However, these previous studies primarily focused on the role played by each environmental factor independently (Posselt et al. 2019) or on small perturbations (Storer and Posselt 2019), whereas here we show the co-dependence of these parameters across a wide range of values. In summary, these results demonstrate that both high CAPE and precipitable water are individually necessary but not sufficient to produce the strongest third of CCCs in our simulations.

#### 4.4.a.2 Storm Precipitation Intensity

We now focus on CCC precipitation rate by examining how the precipitation bins map onto the vertical velocity bins and vice-versa (Table 4.3). Globally, storms with the strongest updraft velocities are not necessarily those that are the biggest precipitation producers (Zipser et al. 2006; Hamada et al. 2015). In this case, at least 50% of the storms in each of the precipitation bins are in their corresponding vertical velocity bin (e.g., >50% of  $St\_PCP$  CCCs are  $St\_W$  CCCs) as can be seen along the top- left to bottom-right diagonals of Table 4.3. However, that said, there are a number of CCCs whose precipitation intensity doesn't match with their vertical velocity and vice versa. Only 67.6% of the  $St\_PCP$  CCCs are also  $St\_W$  CCCs (top part of Table 4.3). Some of this is due to the fact that there are more  $St\_PCP$  CCCs than  $St\_W$  CCCs owing to how the bins were constructed, but even when removing this effect and looking at the number of  $St\_W$  CCCs that are also  $St\_PCP$  CCCs, we see that 18.1% of  $St\_W$  CCCs produce moderate amounts of precipitation ( $Md\_PCP$  CCCs), as opposed to the heaviest precipitation rates

(*St\_PCP*). This suggests that there may be other important environmental controls on precipitation intensity that divides strong dynamical storms (*St\_W* CCCs) into heavy and less heavy precipitation producers.

The role of CAPE, PW and vertical wind shear in determining the precipitation rates is shown in Figure 4.8. It is evident from this figure that the precipitation rate depends somewhat on CAPE (Figure 4.8a). However, unlike the  $W_{\max}$  stratification, the *St\_PCP* CCCs have nearly the same CAPE ( $1691.5 \text{ J kg}^{-1}$ ) as the *Md\_PCP* CCCs ( $1651.7 \text{ J kg}^{-1}$ ), but there is a significant difference between the CAPE of *St\_PCP* CCCs and *Wk\_PCP* ( $1501.8 \text{ J kg}^{-1}$ ) CCCs. This is in contrast to the relationship between CAPE and the vertical velocity bins. Stronger vertical velocities (i.e., those in *St\_W*) are supported by colder environments aloft (Figure 4.5a), resulting in higher overall CAPE, whereas the strongest precipitating storms are supported by warmer environments throughout the column (Figure 4.5b).

Many of the lowest precipitation rate CCCs are also the weakest  $W_{\max}$  CCCs (76.6%; Table 4.3). There is a clear statistically significant difference in the PW between the strongest and weakest rain producers. At all levels below 250 hPa, the mean *St\_PCP* initial dew point temperature is between 0.1 and 0.5 K greater than the *Wk\_PCP* initial environment (Figure 4.5b). The relationship between precipitation rate and PW can also be seen in Figure 4.9b-c. With sufficient CAPE ( $>1000 \text{ J kg}^{-1}$ ), the difference between the initial environments of *St\_PCP* CCCs and *Wk\_PCP* CCCs is based on precipitable water, with a threshold of  $\sim 64 \text{ mm}$  precipitable water and sufficient CAPE ( $>1000 \text{ J kg}^{-1}$ ) required to reach the strongest precipitation rates.

The relationship between increasing precipitation rate and low-level wind shear are similar to the relationship between low-level wind shear and increasing  $W_{\max}$  (Table 4.2; Figure

4.8c-f). At low levels (i.e., 0-1 km shear), wind shear monotonically increases with increasing precipitation rate (Figure 4.6c). However, similar to  $W_{\max}$ , the mid-level shear (i.e., 0-3, 0-5, and 2-7 km; Figure 4.6d-f) precipitation relationship is more complex. In each of these cases, the *Md\_PCP* CCCs have the lowest mean mid-level shear of the three bins (Table 4.2). Further, we see a similar interplay between 0-3 km shear and the thermodynamic variables (Figure 4.9a and c) as in the  $W_{\max}$  bins (Figure 4.7a and c), with enhanced shear resulting in more frequent *St\_PCP* CCCs at lower CAPE and precipitable water values. We speculate that this too is because of changes to entrainment. *Md\_PCP* CCCs have the driest initial environments in the mid-levels (i.e., 700-300 hPa; Figure 4.5d), so their relatively lower shear is necessary to reduce overall entrainment of this very dry air. *Wk\_PCP* CCCs are necessarily precipitating at a lower rate partially due to the relatively higher entrainment caused by the stronger shear.

#### *b. Stratifying by convective organization*

Examining the results of the storm organization stratification, we see that there are many more *Clustered* systems than *Isolated* systems (Table 4.4). It is also obvious that *Isolated* storms generally have lower cloud top heights and smaller total hydrometeor mixing ratios than *Clustered* storms (Figure 4.10a-b; above 15 km there are few *Isolated* storms, so the average ice mixing ratios here are driven by those outliers). Further, we see that *Isolated* storms have more frequent positive vertical velocities below the melting level inversion (Figure 4.10c). This raises two primary questions: 1) Why do *Isolated* storms reach the upper levels less frequently? and 2) What then is the difference in *Clustered* and *Isolated* storm initial environments?

It is evident from Figure 4.11 that *Isolated* CCCs are characterized by initial environments that have higher CAPE, lower PW and lower vertical wind shear than their *Organized* counterparts. Alternatively, *Organized* CCCs have initial environments of lower

CAPE, higher PW and greater vertical wind shear than their *Isolated* counterparts. The increase in CAPE, coupled with the overall decrease in cloud top height in *Isolated* storms compared with *Clustered* CCCs, suggests that for *Isolated* storms to reach the mid-levels, they need greater buoyancy to survive the impacts of the entrainment of the drier environmental air. *Clustered* CCCs, by definition, have adjacent clouds and hence are generally better protected from lateral entrainment of dry air than *Isolated* CCCs (Becker et al. 2018). As CCCs grow vertically, their growth can also be limited by cloud-top entrainment, which will have a much more profound impact on *Isolated* CCCs than on *Clustered* CCCs owing to the much drier column (Figure 4.5e). Examining both lateral and cloud-top entrainment, *Isolated* CCC growth is more easily slowed or stopped by entraining this relatively drier air, resulting in lower cloud top heights overall despite stronger atmospheric instability.

While the cloud adjacency and resulting changes to entrainment explain the difference in cloud top heights between the two CCC types, this doesn't explain why *Isolated* CCCs stay isolated. Lower precipitable water is certainly a contributor, as initiating convection is more difficult in a relatively drier environment. However, there are also significant differences in wind shear, with *Organized* storms having larger wind shear (Figure 4.11c-f; Table 4.4). This is largely in keeping with our understanding of the role of wind shear in organizing convection (Klemp and Wilhelmson 1978; Weisman and Klemp 1982; LeMone et al. 1998; Johnson et al. 2005). The *Isolated* CCCs are found only to occur in environments characterized by weaker vertical wind shear. The enhanced entrainment associated with stronger vertical wind shear and drier overall environment appears to prevent the development of *Isolated* CCCs.

### *c. Organized Storm Linearity*

Long linear squall lines are a persistent feature in the MC (see, e.g., the squall line feature near 7.5N, 118E in Figure 4.1b, c; LeMone et al. 1984; Takahashi and Keenan 2004; Reid et al., 2015; Hassim et al. 2016; Vincent and Lane 2016). Of course, not all *Clustered* convection examined in the previous section are linear. Many *Clustered* systems are nonlinear or more circular in nature (see, e.g., the large convective feature at 15N, 127E in Figure 4.1b; Miller and Fritsch 1991; Inoue et al. 2008).

As Figure 4.12 demonstrates, *Linear* CCCs share many similar characteristics with their *Nonlinear* counterparts. *Linear* storms have, on average, slightly stronger updrafts than *Nonlinear* storms (Figure 4.12c), with ~76% of *Linear* CCCs falling within the *St\_W* or *Md\_W* intensity categories compared with ~72% of *Nonlinear* CCCs. However, it is notable that while *Linear* CCCs primarily have stronger vertical velocities in the lower portions of the storm, especially below the freezing level, that the *Nonlinear* organized systems more frequently have stronger updraft velocities well above the freezing level (Figure 4.12c). Looking at Figure 4.12b, one can see that the average ice and liquid hydrometeor mixing ratios are similar between the two storm morphologies, with *Linear* CCCs having slightly higher mixing ratios than *Nonlinear* CCCs, especially below the freezing level, likely driven by the slightly stronger vertical velocities. Overall, the in-cloud properties between the two CCC types are similar, other than the obvious difference in overall system morphology.

Changes in storm system linearity appear to be driven by changes in the initial environment. *Linear* storm environments have warmer temperatures near the surface and colder temperatures above ~650 hPa and are significantly drier throughout most of the atmospheric column (Figure 4.5d). As such, *Linear* systems are characterized by environments with larger

average CAPE and more limited precipitable water (Figure 4.13a-b). It is likely that this larger average CAPE in the *Linear* CCCs is the primary driver of the increased lower-level vertical velocities compared with the *Nonlinear* CCCs.

Vertical wind shear is also statistically significantly different between the two storm system types for all but 2-7 km shear, with nonlinear storm systems having larger vertical wind shear magnitudes throughout the low to mid-levels (Figure 4.13c-f, Table 4.4). We see this dependence on weaker shear promoting *Linear* storms at all precipitable water values (Figure 4.14c), indicated by the stark horizontal divide along  $7.5 \text{ m s}^{-1}$  of the 0-3km shear figure. The relationship between CAPE and lower-level wind shear is somewhat more complex (Figure 4.14a). At low CAPE values (i.e.,  $<1000 \text{ J kg}^{-1}$ ), *Nonlinear* CCCs are less frequent even at lower wind shear. As CAPE increases, *Linear* CCCs become more frequent and are more frequent with increasing wind shear through  $7.5 \text{ m s}^{-1}$  of 0-3 km shear.

The wind shear described so far has been vector magnitude wind shear, which includes the impacts of both directional and speed shear. When separating out directional and speed shear, we see that for almost all of the levels of shear calculated here that the average *Nonlinear* directional and speed shear are both higher than the average *Linear* shear, with directional wind shear being more different than speed shear between most *Linear* and *Nonlinear* CCCs (Figure 4.15). The 2-7 km speed shear is, however, slightly greater in the *Linear* CCC environments than in the *Nonlinear* environments (Figure 4.15h). In all shears analyzed (except for 2-7 km speed shear), we see a larger standard deviation in shear in *Nonlinear* than *Linear* systems (Figure 4.15; Table 4.4).

The enhanced *Nonlinear* CCCs with increasing wind shear is a somewhat surprising result, as in existing literature it has been shown that *Linear* systems are typically correlated

with stronger vertical wind shear (LeMone et al. 1998; Johnson et al. 2005; Grant et al. 2018). It is worth noting that both the *Linear* CCCs and *Nonlinear* CCCs in this study are considered “organized convection” by our definition, where by “organized” we mean that each CCC is touching another CCC; the only difference is whether cells are organized linearly or nonlinearly. As we demonstrated in Section 4.4b, organized CCCs have increased initial environmental wind shear versus their isolated counterparts, reinforcing the role of wind shear in organizing convection, be it linear or non-linear.

A complete process-level study would be required to entirely understand the relationship between wind shear and linearity, but we will briefly speculate here on the cause. Wind shear, especially directional wind shear, appears to be the primary difference between the *Linear* and *Nonlinear* CCCs observed here. Such wind shear modulates the momentum transport through convective systems. Changes to the momentum transport could result in changes to the downdrafts and therefore the location of new convective initiation. Further, as has been widely demonstrated (Mapes 1993; Shige and Satomura 2001; Lane and Moncrieff 2015; Grant et al. 2018), gravity waves are also important regulators of tropical convection, especially organized convection. In a high directional shear environment, these gravity waves could be sheared apart or could be moving in multiple distinct directions, enhancing convection in a nonlinear fashion.

#### **4.5. Summary and Discussion**

In this study, we have examined how the storm properties of intensity, organization, and linearity of Maritime Continent deep convective cloud (CCC) features are governed by their initial thermodynamic and dynamic environments. A high-resolution long-duration numerical model simulation, together with a tracking and segmentation package, were employed to produce a dataset of the lifecycles of nearly two hundred thousand individual CCCs and their associated

initial environments in the Maritime Continent (MC) summer. This novel methodological approach enabled detailed storm-by-storm sampling of both the storm initial environments and storm properties in a large-scale, realistic MC environment over a month-long duration.

Using this dataset of CCC properties and formation environments, we have been able to draw the following conclusions:

1. Large CAPE and large PW are *both* necessary conditions for the development of strong vertical velocities within the CCCs in the Maritime Continent. Even with extremely high CAPE (e.g.,  $>2500 \text{ J kg}^{-1}$ ), relatively high (approximately 63 mm) precipitable water is necessary for the formation of strong updraft velocities (Section 4.4.a.1).
2. Many (80.9%) of the CCCs with the strongest vertical velocities produce the strongest precipitation rates, but only 67% of the strongest precipitating CCCs have the strongest updraft velocities. The primary differentiator between strongly precipitating CCCs and weakly precipitating CCCs is precipitable water, with CAPE playing an important, albeit lesser, role. (Section 4.4.a.2)
3. CCC organization is primarily driven by vertical wind shear, with organized CCCs having stronger wind shear. While Isolated CCCs have stronger vertical velocities below the freezing level, they have significantly lower cloud tops. We hypothesize that such cells are more exposed to environmental entrainment relative to organized CCCs. (Section 4.4b)
4. Linear CCCs have significantly weaker vertical wind shear than nonlinear CCCs in both the low- (0-1 km, 0-3 km) and mid-levels (0-5 km, 2-7 km). This relationship holds true whether examining the shear as a vector magnitude value or when separating out directional and speed shear (except for 2-7 km speed shear, which is slightly larger in

linear CCCs on average than nonlinear CCCs). We speculate that the cause of this surprising result is because of changes to momentum transport or gravity waves with certain orientations of the shear vector, although a full process-level study would be necessary to confirm this speculation. (Section 4.4c)

These four conclusions have a number of implications for future research and operations. Entrainment appears to play an important role in CCC intensity, organization, and linearity. Higher-resolution simulations that more robustly represent the impacts of entrainment should be completed to fully understand this dependence, as a 1 km horizontal grid spacing is not sufficient to resolve all of the turbulent eddies that are responsible for lateral entrainment. Further, higher temporal resolution observations of CCCs should also be pursued to quantify the effects of entrainment on various storm modes.

Our results around wind shear, notably that linear systems have lower average wind shear than nonlinear systems, are surprising. The sensitivity of mid-latitude organized systems to shear has been well demonstrated, with increasing wind shear generally resulting in more linear systems as long as the cold pools are sufficiently strong (Rotunno et al. 1988; Weisman and Rotunno 2004). Results in the tropics have been more mixed, with linear systems having a wide variability in the environmental vertical wind shear (Houze and Cheng 1977; LeMone et al. 1998; Grant et al. 2018). Follow up studies should be completed to fully understand the relationship between wind shear and organized linear systems, organized nonlinear systems, and isolated systems in the tropics. Wind shear clearly plays an important role in organization and linearity, but process-level studies will be necessary to elucidate the wind shear-linearity relationship discovered here.

While we have covered the environmental sensitivity to dynamics and thermodynamics, this analysis has not considered the role of another important environmental parameter, that of aerosol. In the simulation examined in this work, we keep aerosol type and loading constant throughout the simulation. In the natural world, especially in the MC, aerosol concentrations and type can vary significantly (Atwood et al. 2017), and has long been understood to play an important role in changing cloud properties and lifetimes (Twomey 1977; Albrecht 1989). Future work should examine how these cloud and precipitation properties change with aerosol conditions, as well as the covariance with dynamic and thermodynamic conditions.

## 4.6. Tables and Figures

Table 4.1: Model Features and Experiment Setup Parameters

Model Parameter	Description
Grid	$\Delta x=1\text{km}$ , 1950x1800 grid points (1950 km x 1800 km); $\Delta z = 50\text{ m}$ stretched to 300m over 100 vertical levels at a stretch ratio of 1.03
Radiation	Harrington (1997) 2-stream radiation; aerosol radiative effects on
Microphysics	RAMS double-moment bin emulating microphysics (Saleeby and van den Heever 2013)
Aerosol	Static aerosol profile (i.e., no advection, sources, or sinks) of sulfate-type; $600\text{ kg}^{-1}$ at the surface; radiatively and microphysically active
Turbulence Scheme	Smagorinsky (1963) with vertical diffusions based on Hill (1974)
Surface Scheme	LEAF-3 (Lee 1992; Walko et al. 2000)
Initial and Boundary Conditions	Open radiative lateral boundaries (Klemp and Wilhelmson 1978) nudged using ERA-5 Reanalysis hourly data; nudging at the lateral and top boundaries at a 900 s timescale; no central domain nudging
SSTs	Reynolds et al. (2007) daily SST data
Timestep and Duration	Timestep of 2.5s; model simulation run from 00Z 15 August 2019 to 00Z 21 September 2019. Data from 00Z 15

	August to 00Z 22 August are discarded from the analysis to allow for a model spinup period.
Output	5 minute data output

Table 4.2: Environmental statistics for each  $W_{\max}$  bin (left half) and Precipitation Rate bin (right half). Each variable (other than count) is shown as the mean  $\pm$  the standard deviation.

	<b>St_W</b>	<b>Md_W</b>	<b>Wk_W</b>	<b>St_PCP</b>	<b>Md_PCP</b>	<b>Wk_PCP</b>
<b>Number</b>	48500	65329	68320	58050	56085	55558
<b>CAPE (J kg<sup>-1</sup>)</b>	1802.8 $\pm$ 744.5	1550.9 $\pm$ 768.4	1489.7 $\pm$ 802.5	1691.5 $\pm$ 721.5	1651.7 $\pm$ 762.7	1501.8 $\pm$ 822.1
<b>Precipitable Water (mm)</b>	64.4 $\pm$ 3.4	64.2 $\pm$ 3.7	63.1 $\pm$ 4.7	64.7 $\pm$ 3.6	63.7 $\pm$ 4.0	63.4 $\pm$ 4.1
<b>0-1km Shear (m s<sup>-1</sup>)</b>	5.1 $\pm$ 3.0	4.7 $\pm$ 3.0	4.6 $\pm$ 3.1	5.1 $\pm$ 3.1	4.5 $\pm$ 2.9	4.5 $\pm$ 3.0
<b>0-3km Shear (m s<sup>-1</sup>)</b>	6.2 $\pm$ 3.5	5.6 $\pm$ 3.4	5.6 $\pm$ 3.4	6.2 $\pm$ 3.6	5.4 $\pm$ 3.2	5.6 $\pm$ 3.4
<b>0-5km Shear (m s<sup>-1</sup>)</b>	7.0 $\pm$ 3.8	7.1 $\pm$ 3.8	7.4 $\pm$ 3.9	7.3 $\pm$ 3.9	6.9 $\pm$ 3.7	7.3 $\pm$ 3.9
<b>2-7km Shear (m s<sup>-1</sup>)</b>	7.2 $\pm$ 4.0	7.7 $\pm$ 4.0	8.0 $\pm$ 4.0	7.6 $\pm$ 4.0	7.5 $\pm$ 3.9	7.7 $\pm$ 3.9

Table 4.3: (Top half of the table): Percentages of cells in each precipitation bin that are in each  $W_{\max}$  bin (i.e.,  $\frac{\# \text{ in precipitation and } W_{\max} \text{ bin}}{\text{Total \# in precipitation bin}}$ ); (Bottom half of the table): Percentages in cells in each  $W_{\max}$  bin that are in each precipitation bin (i.e.,  $\frac{\# \text{ in precipitation and } W_{\max} \text{ bin}}{\text{Total \# in } W_{\max} \text{ bin}}$ ).

<b>Percentage of precipitation rate CCC in each <math>W_{\max}</math> bin</b>	<b><i>St_W</i></b>	<b><i>Md_W</i></b>	<b><i>Wk_W</i></b>
<b><i>St_PCP</i></b>	67.6%	31.0%	1.42%
<b><i>Md_PCP</i></b>	15.6%	61.9%	22.5%
<b><i>Wk_PCP</i></b>	0.837%	22.5%	76.6%
<b>Percentage of <math>W_{\max}</math> CCCs in each precipitation bin</b>	<b><i>St_W</i></b>	<b><i>Md_W</i></b>	<b><i>Wk_W</i></b>
<b><i>St_PCP</i></b>	80.9%	27.4%	1.18%

<i>Md_PCP</i>	18.1%	53.1%	18.2%
<i>Wk_PCP</i>	0.972%	19.3%	61.9%

Table 4.4: As for Table Table 4.2, but for clustered, isolated, linear, and nonlinear cells.

	<b>Clustered</b>	<b>Isolated</b>	<b>Linear</b>	<b>Nonlinear</b>
<b>Number</b>	148088	34061	36133	54565
<b>CAPE (J kg<sup>-1</sup>)</b>	1478.9 ± 782.6	1852.7 ± 731.8	1428.5 ± 755.9	1271.7 ± 798.2
<b>Precipitable Water (mm)</b>	64.5 ± 3.7	62.0 ± 4.5	64.9 ± 3.6	65.4 ± 3.6
<b>0-1km Shear (m s<sup>-1</sup>)</b>	5.0 ± 3.1	4.1 ± 2.8	5.0 ± 3.0	5.8 ± 3.5
<b>0-3km Shear (m s<sup>-1</sup>)</b>	6.0 ± 3.5	5.1 ± 3.1	5.7 ± 3.3	7.0 ± 4.0
<b>0-5km Shear (m s<sup>-1</sup>)</b>	7.4 ± 4.0	6.5 ± 3.4	7.1 ± 3.8	8.6 ± 4.4
<b>2-7km Shear (m s<sup>-1</sup>)</b>	7.8 ± 4.1	7.5 ± 3.8	7.7 ± 4.2	8.2 ± 4.2

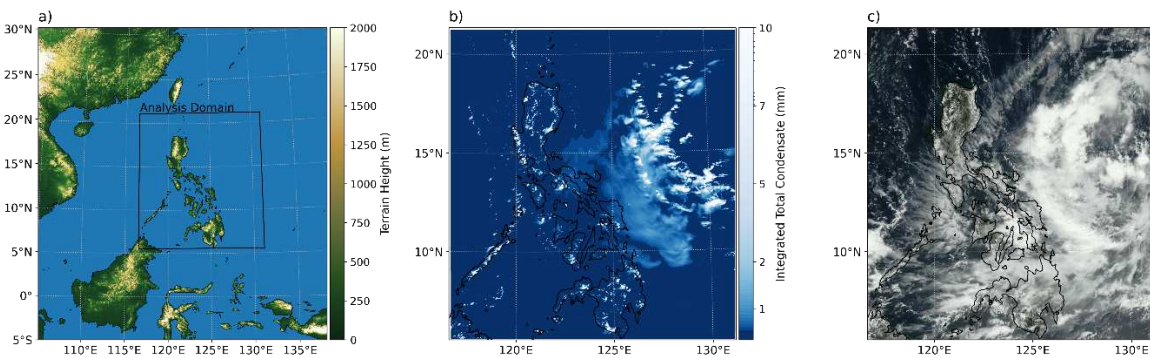


Figure 4.1: (a) The location, area, and topography of the large-domain, long-duration, high-resolution numerical simulations conducted for this study. Shading indicates the topographical relief, and the black box shows the simulation domain. (b) A wide wide variety of convective modes, morphology, and scales is captured in this simulation as demonstrated by this image at 04Z 26 August 2019. Shading indicates the integrated total condensate (mm). (c) The simulation is capturing the same modes of convection as observed, demonstrated by this Advanced Himawari Imager truecolor image from 04Z 26 August 2019, the same time as the model snapshot in (b).

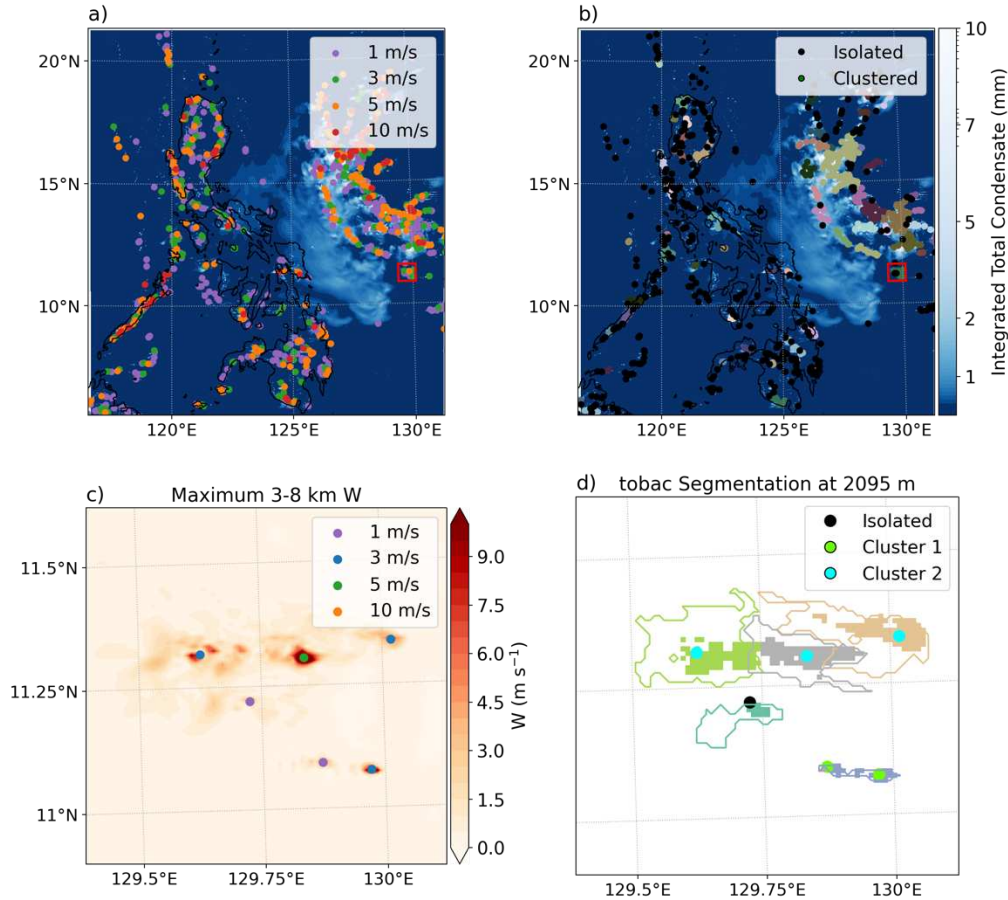


Figure 4.2: Examples demonstrating the feature identification, segmentation, and tracking algorithms of *tobac*. (a) As in Figure 1b, but with *tobac*-identified storm features colored by maximum updraft velocity. The red box indicates the area featured in (c) and (d); (b) as in (a), but with *tobac*-identified features colored by storm cluster, where isolated storms are colored using black, and all other colors indicate storms that are clustered with at least one other point; (c) the maximum midlevel vertical velocity (i.e.,  $W_{\max}$ ) (red and blue shading) and the features as identified by *tobac* (dots colored by  $W_{\max}$ ) in the region highlighted in (a); (d) an example of the segmentation analyzed by *tobac*, where the contours indicate regions in this 2D slice identified as individual segmented CCCs, with each color representing a different discrete CCC (shaded). Overlaid on this (colored contour lines) are the overall maximum extent of each of the features throughout the column. The overlaid dots indicate the location of identified *tobac* features and are in the same locations as in (c), but they are colored by their convective cluster, with the green dots indicating one cluster (identified as cluster 1 as a demonstration), the blue dots indicating a different cluster (cluster 2), and black dots identifying *Isolated* CCCs. The five points labeled as either cluster 1 or cluster 2 are all *Organized* CCCs.

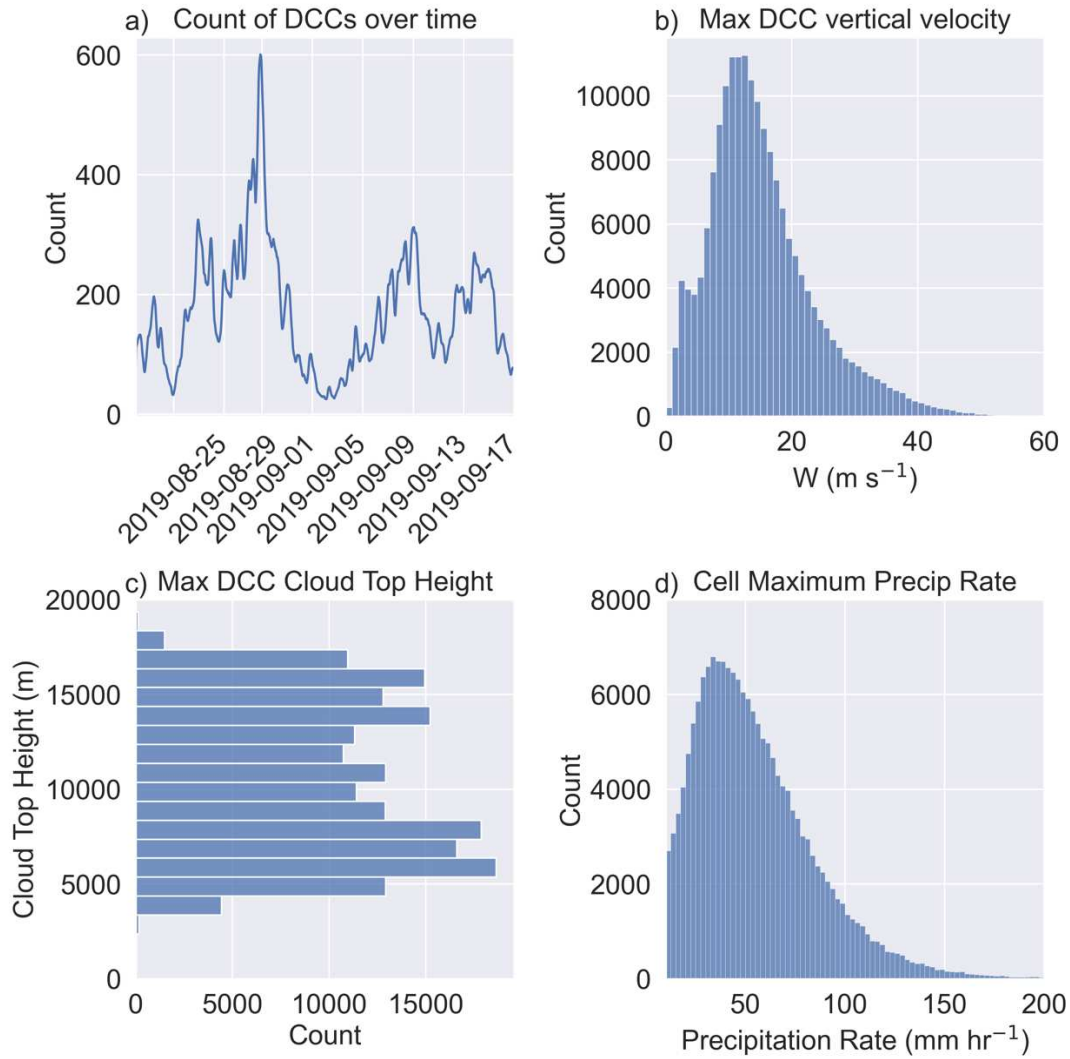


Figure 4.3: Bulk CCC characteristics for the duration of the simulation: (a) the number of CCCs per time period, with a moving average window of 6 hours; (b) histogram of CCC maximum  $W$  ( $\text{m s}^{-1}$ ) over time, binned into  $1 \text{ m s}^{-1}$  bins; (c) histogram of maximum CCC cloud top height (m) over time, binned into 1 km bins; (d) histogram of CCC maximum precipitation rate ( $\text{mm hr}^{-1}$ ) for all tracked, precipitating CCCs, binned into  $2.5 \text{ mm hr}^{-1}$  bins

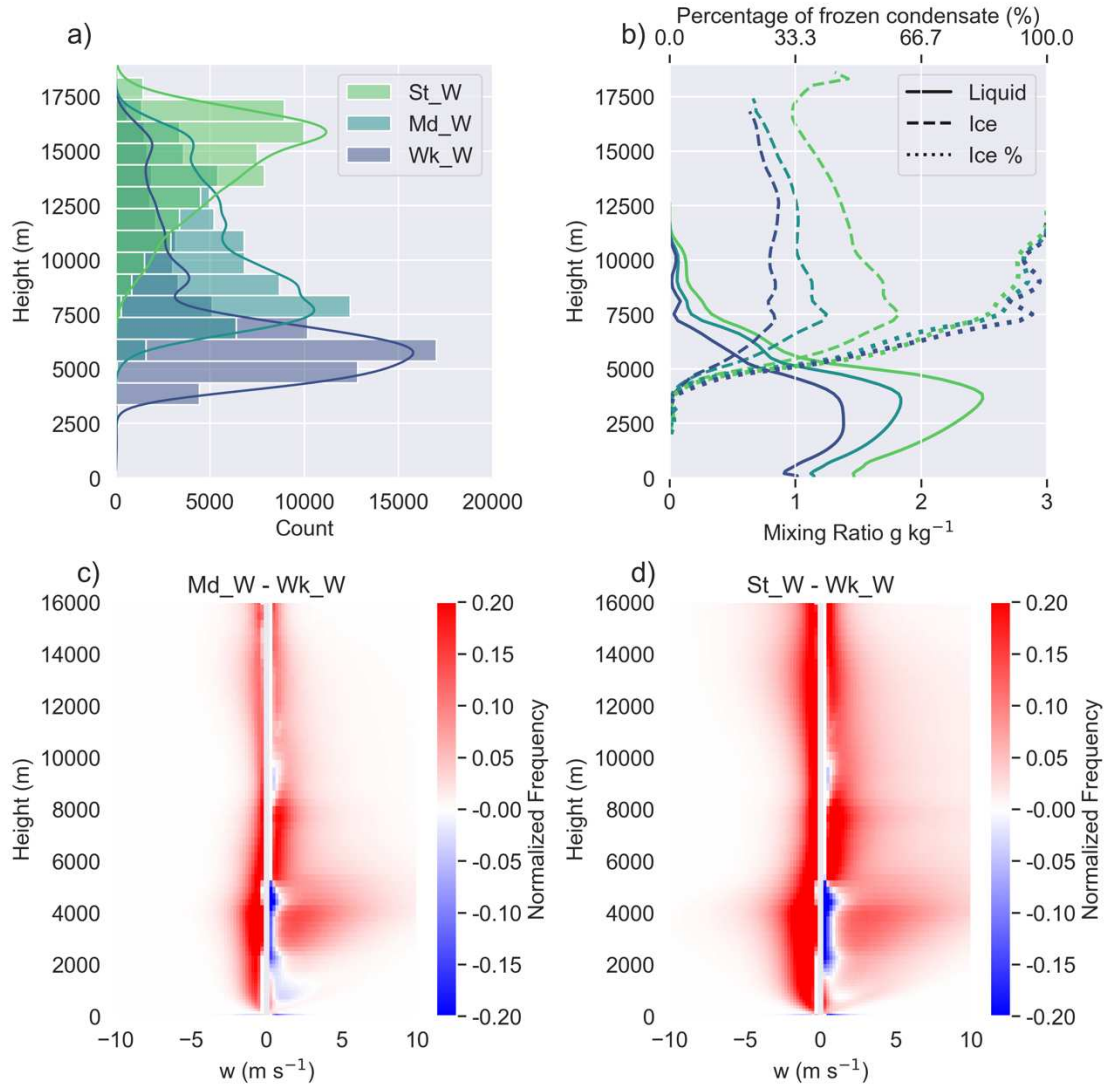


Figure 4.4: Cloud statistics stratified by storm  $W_{\max}$  intensity. (a) Cloud top height histogram (bars) and kernel density estimate (i.e., a calculated estimation of the underlying probability density function which can be thought of as a smoothed histogram; Silverman 1986) (lines); (b) mean vertical profile of liquid (solid lines) and ice (dashed lines) mixing ratios and the ratio of ice mixing ratio to total condensate (dotted lines; top axis). In (a-b), the data are colored by their  $W_{\max}$  bins as defined in the text:  $St\_W$  (light green),  $Md\_W$  (teal), and  $Wk\_W$  (dark blue). (c) vertical velocity CFAD difference between  $Md\_W$  and  $Wk\_W$ ; (d) as in (c), but for the difference between  $St\_W$  and  $Wk\_W$ .

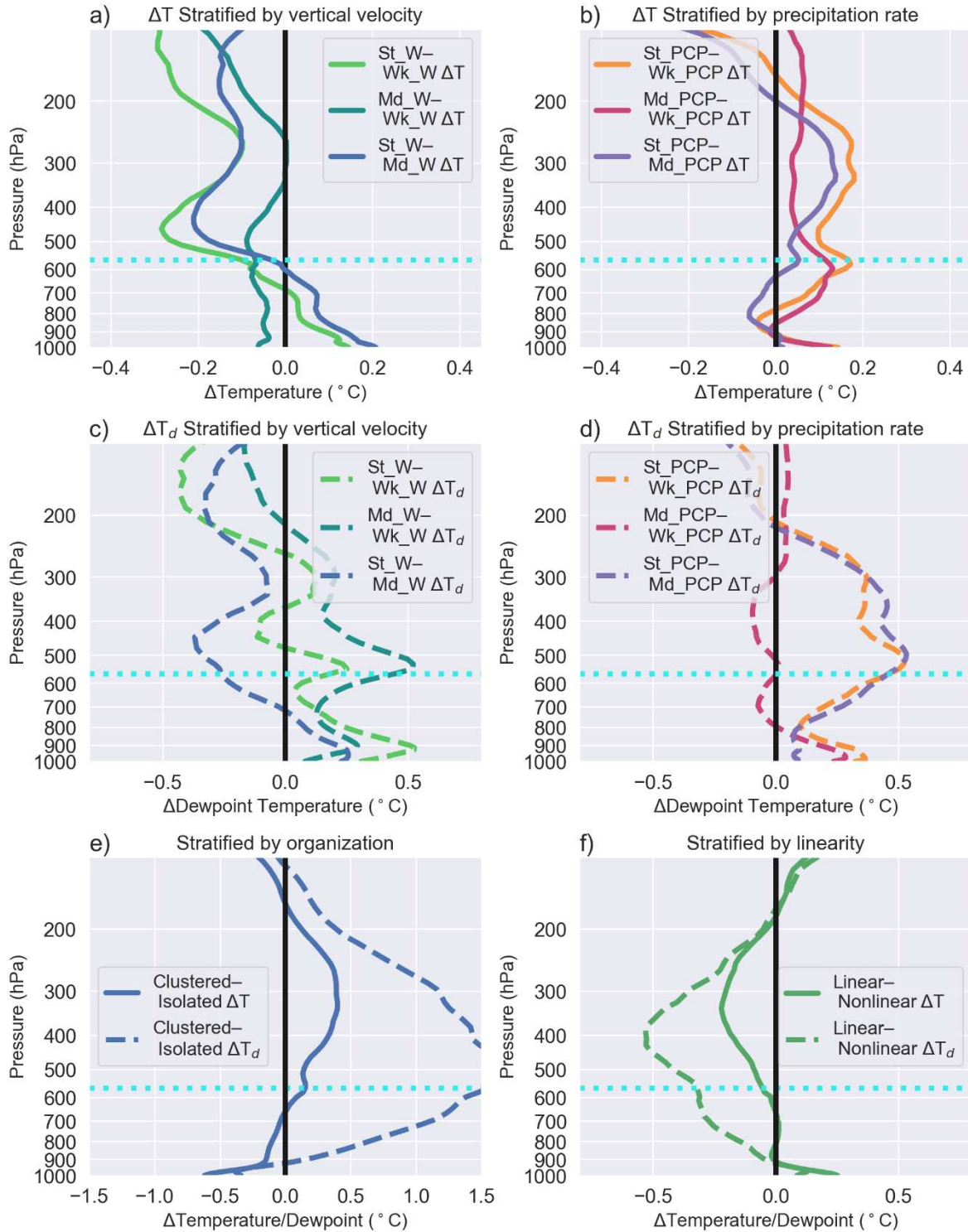


Figure 4.5: CCC initial thermodynamic environments: mean change in temperature ( $\Delta T$ ; solid lines in a, b, e, and f) and dewpoint ( $\Delta T_d$ ; dashed lines in c, d, e, and f) stratified by each of our four CCC properties, where the change is as described in the legend. In all plots, the blue dotted line at approximately 575 hPa indicates the approximate freezing level, and the black vertical line indicates the 0 line from the abscissa. (a) Vertical velocity environmental temperature

stratification:  $Wk\_W$  subtracted from  $St\_W$  (light green) and  $Md\_W$  (dark green);  $Md\_W$  subtracted from  $St\_W$  (blue). (b) Precipitation rate temperature stratification:  $Wk\_PCP$  subtracted from  $St\_PCP$  (orange) and  $Md\_PCP$  (red);  $Md\_PCP$  subtracted from  $St\_PCP$  (purple). (c,d) As in (a,b), but for dewpoint temperature. (e) Organization stratification: *Isolated* subtracted from *Clustered*, including both temperature (solid lines) and dewpoint temperature (dashed lines). (f) as in (e), but for the linearity stratification: *Nonlinear* subtracted from *Linear*.

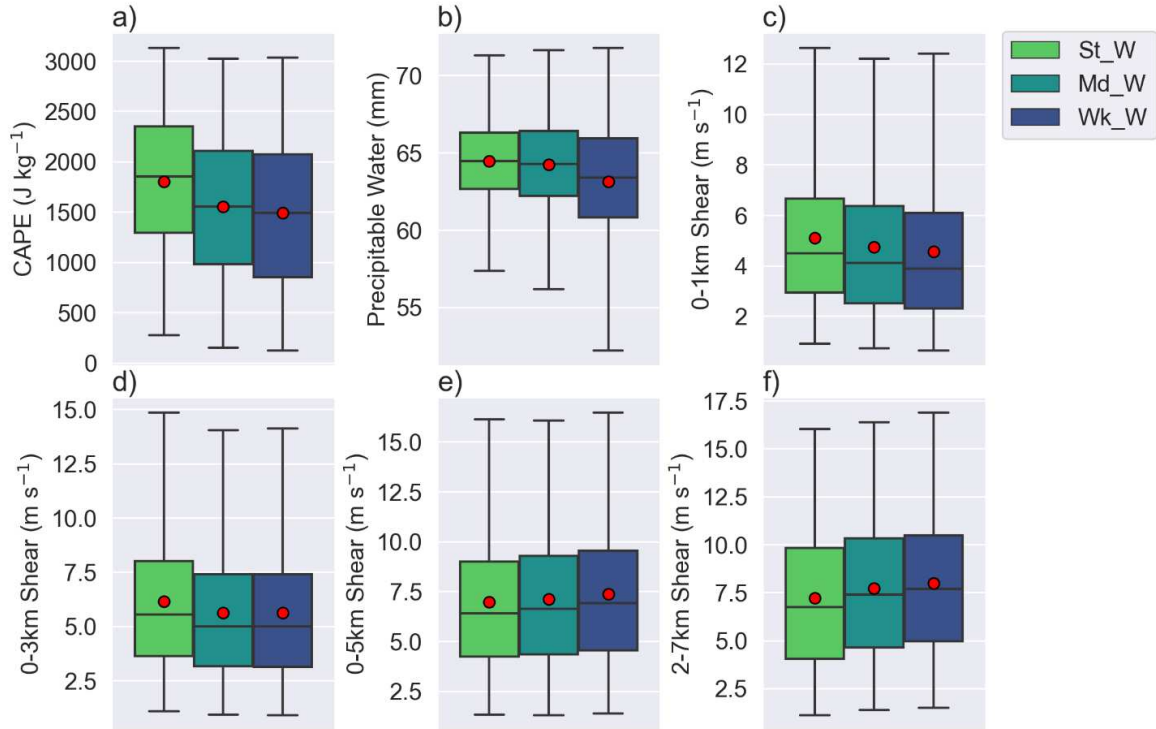


Figure 4.6: Cell environments stratified by cell  $W_{\max}$  bin, where the bin colors are as in Figure 4. Shown are box plots of the distribution for the three  $W_{\max}$  bins where the mean is denoted by a red dot; the median by the horizontal line through the box; the edges of the box denote the quartiles, and the whiskers extend to the 2.5<sup>th</sup> and 97.5<sup>th</sup> percentiles; for (a) CAPE ( $\text{J kg}^{-1}$ ) (b) Precipitable Water (mm); (c) vertical wind shear from 0 to 1 km ( $\text{m s}^{-1}$ ); (d) vertical wind shear from 0 to 3 km ( $\text{m s}^{-1}$ ); (e) vertical wind shear from 0 to 5 km ( $\text{m s}^{-1}$ ); and (f) vertical wind shear from 2 to 5 km ( $\text{m s}^{-1}$ ).

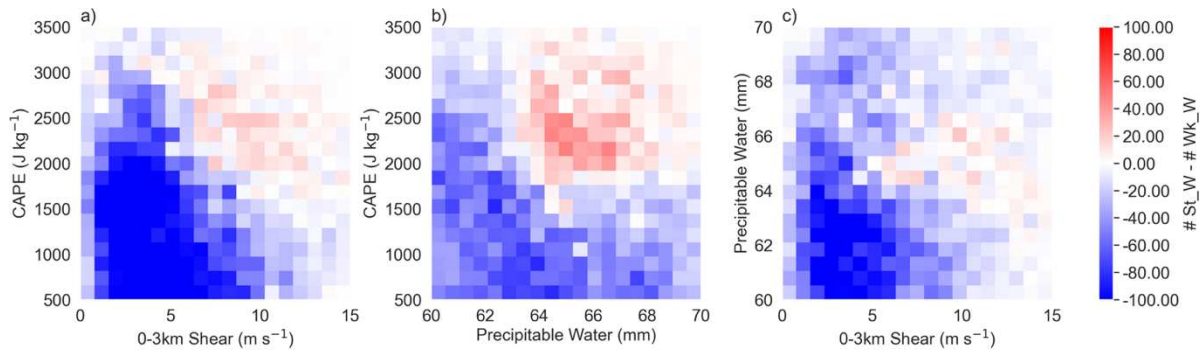


Figure 4.7: 2-D histograms showing the absolute difference in frequency of  $St\_W$  cells and  $Wk\_W$  CCCs as a function of different environmental characteristics, where blue colors indicate more  $Wk\_W$  storms and red colors indicate more  $St\_W$  storms. (a) CAPE is on the ordinate and vertical wind shear from 0 to 3 km is on the abscissa; (b) as in a, but precipitable water is on the abscissa; and (c) as in a, but precipitable water is on the ordinate and vertical wind shear from 0 to 3 km is on the abscissa.

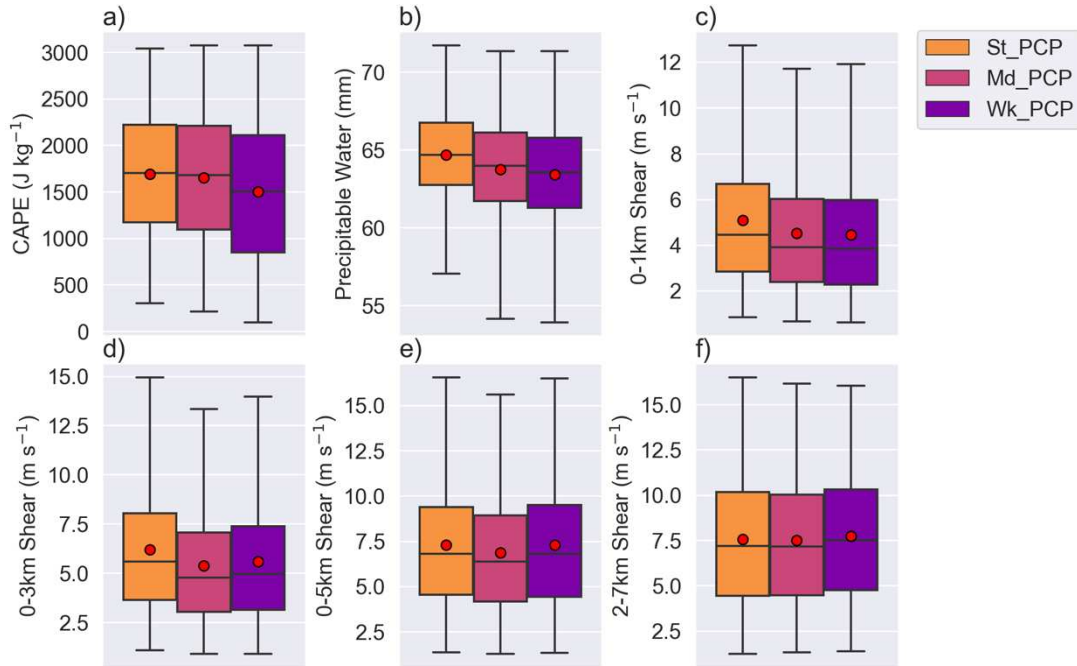


Figure 4.8: As in Figure 2.6, except for the cell precipitation rate bins

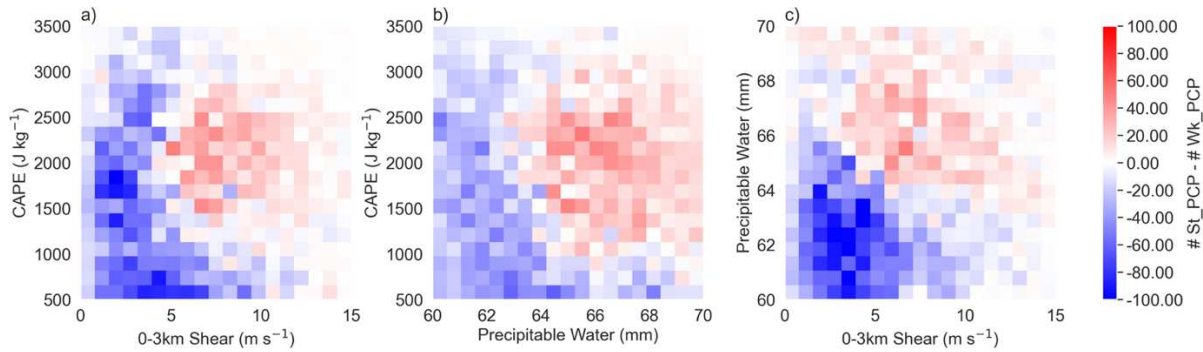


Figure 4.9: As in Figure 2.7, but between  $St\_PCP$  and  $Wk\_PCP$

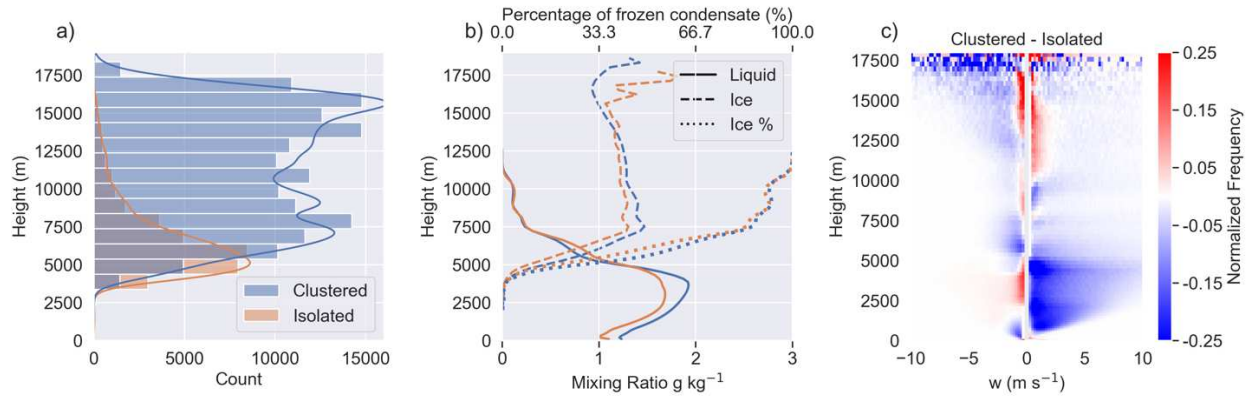


Figure 4.10: Cloud segmentation statistics stratified by cell organization, where blue indicates clustered cells and orange indicates isolated cells. (a-b) as in Figure 4.4a-b but stratified by cell organization; (c) as in Figure 4.4e-f but for the difference between clustered cells and isolated cells. In (c), note that blue values indicate more frequent vertical velocities in that bin from isolated storms, whereas red values indicate more frequent vertical velocities in that bin from clustered storms

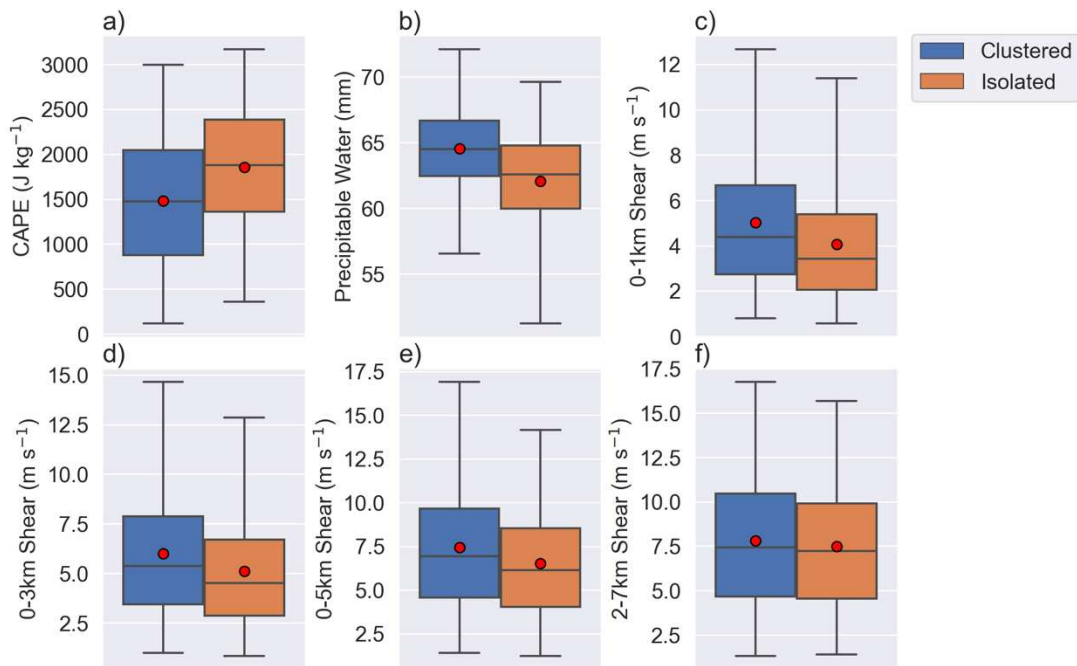


Figure 4.11: As in Figure 6, except stratified by clustered convection (orange) and isolated convection (blue), where the definitions of clustered and isolated convection are defined in the text.

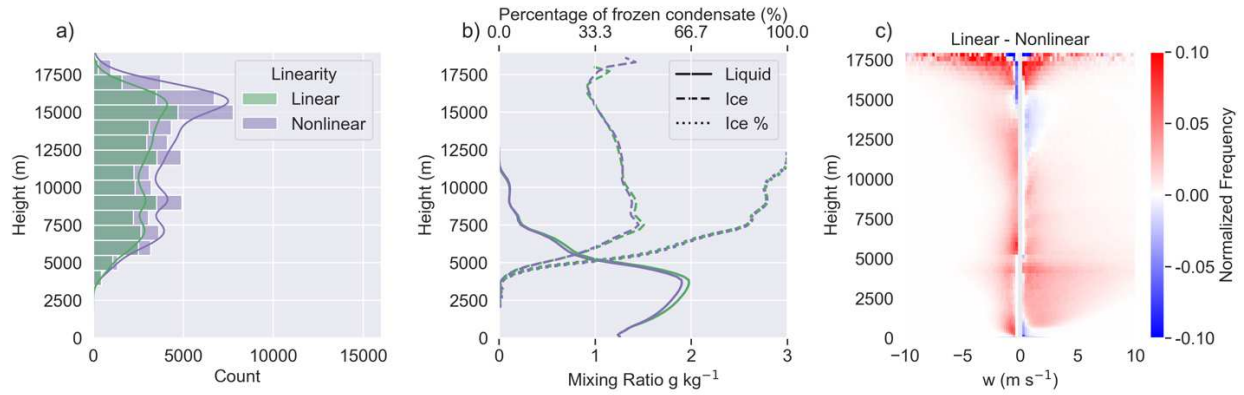


Figure 4.12: As in Figure 4.9, but stratified by linearity, where green indicates Linear organized cells and purple indicates Nonlinear organized cells. Note the change in color bar in (c) compared to Figure 4.9c

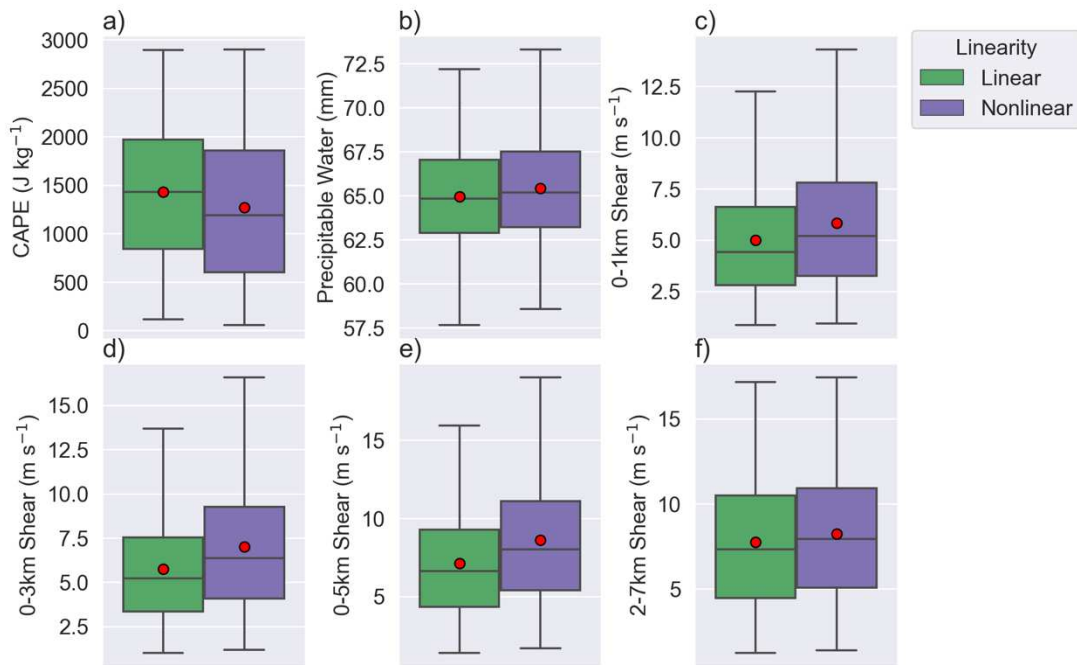


Figure 4.13: as in Figure 4.6, except stratified by linear organized cells (green) and nonlinear organized cells (purple)

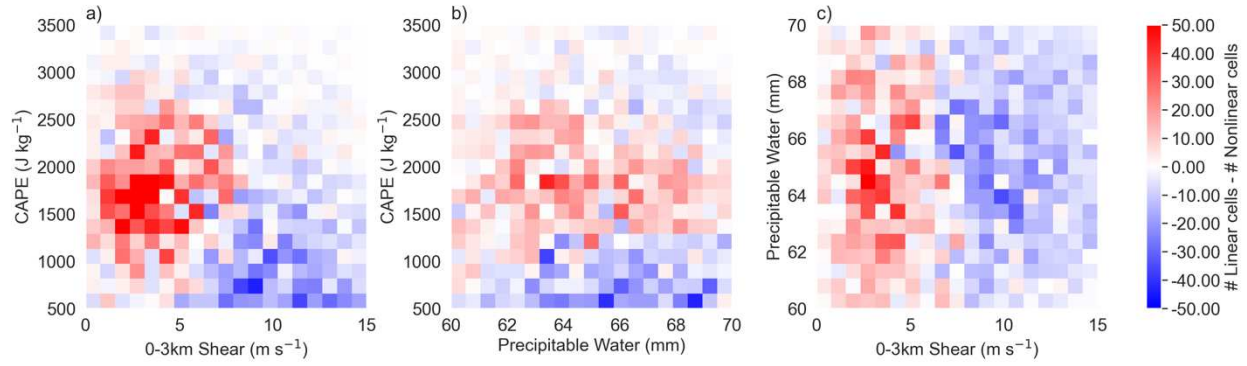


Figure 4.14: as in Figure 2.7, but for the difference in number of cells that are part of clustered linear convection to clustered nonlinear convection, with red colors indicating more linear cells. Note that the color scale has been reduced compared with Figure 4.7 and Figure 4.9, as the total number of clustered storms is smaller than the total number of storms.

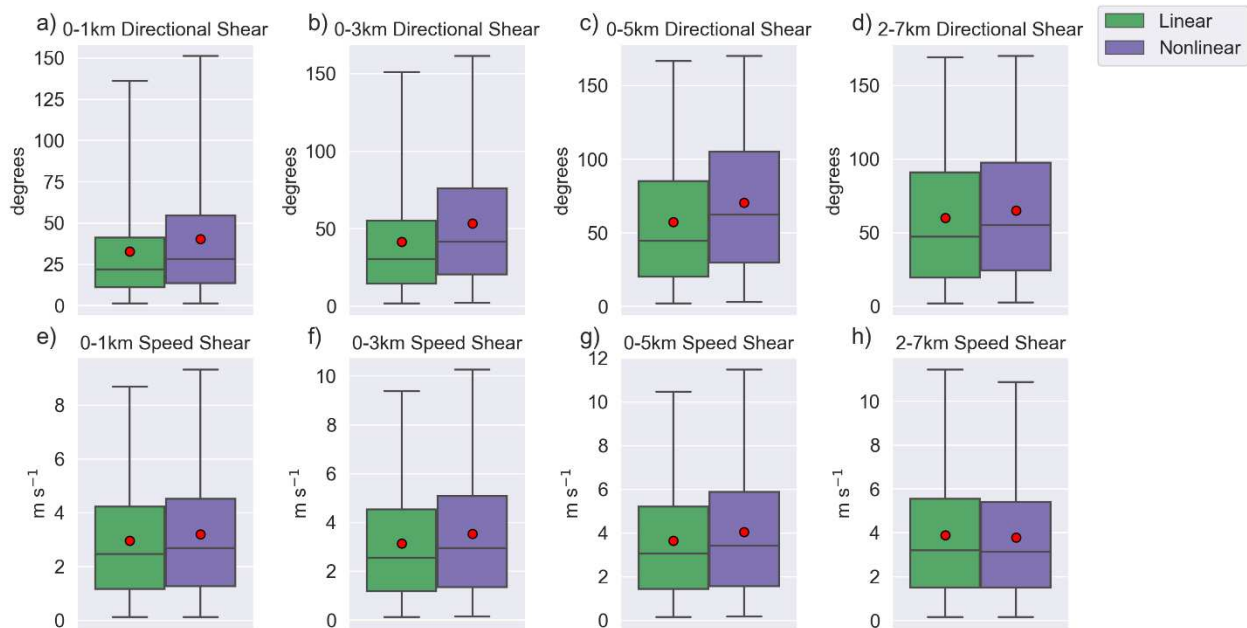


Figure 4.15: Linear and Nonlinear directional (degrees; a-d) and speed ( $\text{m s}^{-1}$ ; e-h) vertical wind shear components at 0-1 km (a, e), 0-3 km (b, f), 0-5 km (c,g), and 2-7 km (d, h).

## **CHAPTER 5: AEROSOL-INDUCED ENHANCEMENT OF CONGESTUS AND SUPPRESSION OF CUMULONIMBUS CLOUDS IN THE TROPICS**

### **5.1. Introduction**

Congestus and Cumulonimbus Clouds (hereafter CCCs), the middle and deep modes of convective clouds in the tropics, are essential contributors to precipitation production in the tropical atmosphere (Johnson et al. 1999). The latent heating released in association with tropical rainfall processes is especially relevant in the Maritime Continent (MC) through its influence on the global circulation (Hartmann et al. 1984; Keenan et al. 2000). In addition to local changes to the production of fresh water, as has been observed in Southeast Asia (Endo et al. 2009; Cruz et al. 2013), any changes to CCC precipitation in the MC can therefore also result in global impacts. Understanding how these convective clouds and their precipitation response to variations in the environment, particularly the aerosol environment, is therefore critical from both a regional and large-scale perspective. Hence, the science question we seek to address here is how does aerosol loading impact convective precipitation in the MC?

Changes in the aerosol environment have long been identified as a source for changing cloud properties (Squires 1958), including suppressing warm rainfall (Squires and Twomey 1960; Warner and Twomey 1968; Albrecht 1989). However, despite extensive efforts, there is still substantial uncertainty on how changing aerosol loading impacts convective cloud properties and precipitation (e.g., Tao et al. 2012; Boucher et al. 2013; Igel and van den Heever 2021; Marinescu et al. 2021). Much of the previous work examining aerosol-cloud interactions (hereafter ACI) on CCCs has investigated these processes by simulating or observing a single deep convective cloud or a small area at a time (Andreae et al. 2004; Xue et al. 2008; Noppel et al. 2010; Grant and van den Heever 2015; Saleeby et al. 2015; Iltoviz and Khain 2016; Iltoviz

et al. 2018). While these techniques can provide novel insights into how cloud properties are locally modulated by aerosol loading, they cannot demonstrate how these modulations feedback onto the large-scale environment and associated clouds.

In addition to the past work examining ACI on one or a few clouds at a time, other previous work has examined aerosol impacts over larger fields of clouds (cloud scene) using observations (Koren et al. 2014; Storer et al. 2014) and numerical models (van den Heever et al. 2011; Seifert et al. 2012; Storer and van den Heever 2013; Sheffield et al. 2015; Barthlott et al. 2018; Marinescu et al. 2021; Barthlott et al. 2022). However, much of this work, with the exception of Seifert et al. (2012), has either examined a relatively short time period, limiting the feedbacks that can occur between ACI and the larger environment, or have been conducted in a 2D idealized mode. These studies have generally found that as aerosol loading increases, convective precipitation decreases (Barthlott et al. 2018; Marinescu et al. 2021; Barthlott et al. 2022). However, this is not a universal finding, with other studies indicating an increase in CCC precipitation with increasing aerosol loading (Seifert et al. 2012; Storer and van den Heever 2013), and still others finding limited scene changes (van den Heever et al. 2011).

As we enter the era of regularly run global cloud resolving models (Satoh et al. 2019; Stevens et al. 2019), an understanding aerosol-induced cloud processes within realistic long-term, large-area simulations is critical. This study represents a novel first step in this direction in that aerosol impacts on surface precipitation within the tropics are evaluated through the use of large-domain, long-duration, high-resolution realistic simulation over the Maritime Continent. Such a setup allows for a large database of convective clouds and the inclusion of local through large-scale feedbacks included. This “basin-scale” simulation setup is needed to examine the

impacts of changing aerosol loading on the CCC precipitation system and prepare for the upcoming era of global cloud resolving models.

## **5.2. Methodology**

### *a. Numerical Simulation Experiments*

To address our science question, a high-resolution, large-domain, long-duration set of simulation experiments in which only the aerosol loading was varied has been conducted using the Regional Atmospheric Modeling System (RAMS; Cotton et al. 2003; Saleeby and van den Heever 2013) version 6.2.14. RAMS has been widely used to examine ACI in a variety of different environments (van den Heever et al. 2006; Grant and van den Heever 2015; Saleeby et al. 2015; Bulatovic et al. 2021; Marinescu et al. 2021).

The details of the model configuration are identical to the basin-scale simulation described by Freeman et al. (2022), but additional information especially relevant to these simulations will be included here. Each of the three simulations was run over a domain of 1800 x 1950 km at a horizontal grid spacing of 1 km and vertical spacing stretched from 100 m to 300 m, with a temporal output of 5 minutes. The three simulations made use of the same exponentially decaying aerosol profile with three different number concentration magnitudes (Figure 5.1a). The aerosol in these experiments was configured to be solely ammonium sulfate ( $\varepsilon=0.90$ ) with a lognormal distribution (geometric mean diameter 40 nm, geometric standard deviation 1.8 nm) and was held constant at every grid point throughout each experiment. The aerosol particles were both radiatively and microphysically active. The most polluted experiment is denoted as HIGH (1200 mg<sup>-1</sup> aerosol at the surface), the moderately polluted experiment as CTL (600 mg<sup>-1</sup> at the surface), and the cleanest experiment as LOW (300 mg<sup>-1</sup> at the surface). Each of the three experiments was simulated for one month, from 15 August 2019 to 20

September 2019, coincident with the NASA Cloud, Aerosol, and Monsoon Processes Philippines Experiment (CAMP<sup>2</sup>Ex) field campaign in the same area (Reid et al. 2022). The first week of the simulation was regarded as model spinup time and discarded from the analysis. The lateral boundaries were nudged with ERA-5 reanalysis (Hersbach et al. 2020), with a nudging zone of 100 km from each boundary, updating hourly, in order to limit synoptic-scale drift of the simulation. This nudging zone is excluded from all analyses and statistics calculated.

### *b. CCC Identification and Tracking*

To examine changes on the individual cloud level, individual clouds were identified and tracked with *tobac* v1.3.0 (Heikenfeld et al. 2019; Chapter 3) in the same manner as Freeman et al. (2022). CCCs are tracked on their maximum midlevel (3-8 km) updrafts, with a minimum threshold of 1 m s<sup>-1</sup>. Cloud volume is then derived from these identified features using a watershedding algorithm (van der Walt et al. 2014), requiring at least 0.5 g kg<sup>-1</sup> total condensate to be identified as part of the cloud. The quality control process used here only removed storms in the areas where the lateral boundaries are nudged, keeping all other tracked *tobac* storms.

## **5.3. Results**

Two primary aerosol-related effects need to be considered as the aerosol loading is increased between these three experiments (LOW, CTL, HIGH). First is the aerosol direct effect (Charlson and Pilat 1969). This effect is fully represented in these experiments and results in decrease in the solar radiation reaching the surface in cloud-free regions through enhanced aerosol scattering with increased aerosol loading. The second effect are the aerosol indirect effects (Twomey et al. 1984; Albrecht 1989), which are also fully represented in these simulations and which result in an increase in the number concentration of cloud droplets as aerosol loading increases (not shown). Through the combination of these two effects, we see a

monotonic decrease in the total amount of precipitation of up to 3.4% as the aerosol loading increases from LOW and HIGH (Table 5.1). This decrease in precipitation with increasing aerosol loading is largely in line with other studies that only represent the aerosol indirect effect including Barthlott et al. (2018; 2022) and Marinescu et al. (2021). However, the literature is not uniform on this point. For example, in a similarly long-duration numerical simulation experiment performed by Seifert et al. (2012) over Germany, they observed an overall increase in precipitation with increasing aerosol loading across the domain (up to 20%, depending on case). With this slight decrease in total precipitation with enhanced aerosol loading as the backdrop, we will now examine changes to both individual clouds and scene-level changes to precipitation.

#### *a. Precipitation Distribution Changes*

We first examine the changes to precipitation over land and ocean regions. As the aerosol concentration increases, the total precipitation over land decreases more so than over ocean (Table 5.1), resulting in a greater percentage of the total scene precipitation occurring over the ocean in more polluted conditions (Figure 5.1b). This effect is especially pronounced during daytime heating (9:00 – 21:00 LT; Figure 5.1b) when the direct aerosol effect is most significant in reducing the amount of solar radiation reaching the surface, and hence the surface heating. In this suite of experiments, the sea surface temperatures are obtained from observations (Reynolds 2007), and are not directly impacted by the aerosol-induced scattering of solar radiation. As such, the aerosol impacts on surface heating will only be realized over land. While this is a shortfall of using fixed ocean surfaces, the large oceanic heat capacities mean that the response of ocean surfaces to aerosol-induced changes in solar radiation is much slower than that over land, and that land will be more significantly affected by changes in radiation caused by the aerosol direct effect. Similar aerosol-induced trends in the precipitation between ocean and land

are therefore still expected, even if the magnitudes may differ. Enhanced aerosol loading therefore shifts the location of precipitation in the mixed land-ocean areas of the MC to be more prominently over maritime regions.

*b. Tracked CCC Changes*

Despite the decrease in oceanic and continental precipitation with increased aerosol loading, we see a monotonic *increase* in the number of tracked CCCs (Table 5.1), with a concomitant decrease in the strongest instantaneous precipitation rates (Figure 5.1c). There is also an overall increase (up to 10.7% between the HIGH and LOW experiments) in the number of tracked CCCs that never precipitate throughout their lifetimes as aerosol loading increases (Table 5.1). Furthermore, on average, tracked CCCs in the HIGH experiment precipitate 4.29% less long than in the LOW experiment (Table 5.1; Figure 5.2b). Increasing aerosol concentrations therefore lead to more total tracked CCCs, but the average CCC precipitates for a shorter time during its lifecycle, and more of the tracked CCCs do not precipitate at all.

As the aerosol loading increases between these experiments, in addition to aerosol-induced impacts on precipitation we also see substantial differences in the properties of the clouds. Examining CCC lifetime cloud top height, the HIGH experiment has 8.1% more terminal congestus clouds (defined here as a CCC that, while tracked, never extends above a cloud top height over 7 km; Johnson et al. 1999; Luo et al. 2009) than the LOW experiment. In comparison, the CTL experiment has 3.3% more terminal congestus clouds than LOW (Table 5.1). The increase in the number of tracked terminal congestus clouds with increased aerosol loading will contribute, in part, to the reduced frequency of upscale growth upscale to cumulonimbus, which is supported by the reduced number of tracked cumulonimbus in the HIGH experiment compared with the CTL and LOW cases (Table 5.1). This overall trend

towards more terminal congestus clouds with lower lifetime cloud top heights and the accompanying decrease in cumulonimbus clouds is also demonstrated in Figure 5.2a.

The increase in frequency of terminal congestus clouds and decrease of cumulonimbus clouds with increasing aerosol concentrations suggests that aerosol invigoration of primarily warm-phase terminal congestus clouds and their subsequent development into deeper cumulonimbus clouds is not prevalent. Further, when examining the precipitation produced by these terminal congestus clouds, we see an overall decrease in the storm maximum precipitation rate as aerosol loading increases (Figure 5.2c). This follows from the aerosol indirect effect, where increasing availability of cloud condensation nuclei (CCN) for the same liquid water content results in smaller cloud droplets, which in turn reduces collision-coalescence processes, and hence the production of rainfall through the warm rain process (Squires 1958; Albrecht 1989). In addition to suppressing the warm rain process, the delay in rain production also allows for entrainment to have more time to erode the cloud and evaporate the condensate before the cloud can produce rainfall, a process that will be further facilitated by a shift in the cloud droplet spectrum to smaller sizes.

When examining deeper cumulonimbus clouds, defined here as those clouds reaching a maximum cloud top height of greater than 7 km AGL, we see limited changes in maximum rainfall rates (Figure 5.2d). This suggests that for deeper convective clouds with more robust ice phase driven precipitation, there is less of an overall impact of increasing aerosol loading on the surface precipitation. The release of additional latent heating in association with the lofting and freezing of the more numerous but smaller cloud droplets (Andreae et al. 2004; Koren et al. 2005, 2014; van den Heever et al. 2006; Rosenfeld et al. 2008; Igel and van den Heever 2021)

may offset the decrease in warm rain production by invigorating the deep convective updraft, however, the impacts appear small.

### *c. Convective Cloud Organization*

So far, we have primarily focused on individual cloud systems. However, a common feature in the summer MC are larger, organized cloud systems, which can produce heavy precipitation (LeMone et al. 1998; Reid et al. 2015; Ling et al. 2019). Here, we will examine organized cloud systems using the same definition of organized as in Chapter 4. This method labels an individual tracked cloud as clustered when the segmented volume of the cloud with a minimum total condensate of  $0.5 \text{ g kg}^{-1}$ , as determined by the *tobac* tracking package, touches another tracked cloud at any point in its lifetime.

Using this definition, we see little change in the percent of tracked clouds that are defined as part of a cluster as a function of aerosol loading, with the LOW case having 77.5% of its tracked clouds classified as organized, CTL having 77.4%, and HIGH having 77.0%. Further, we see relatively little change in the precipitation properties between isolated and organized CCCs, as demonstrated in Figure 5.3. These results indicate that while increasing aerosol has substantial impacts on precipitation at the individual cloud level which results in changes to domain-wide statistics, aerosol impacts on the upscale organization of convection is largely unaffected.

## **5.4. Conclusions**

Aerosol impacts on congestus and cumulonimbus precipitation processes in the tropics, especially within the Maritime Continent (MC), have not been well studied from an integrated scene-wide perspective. In this work, we have investigated aerosol impacts on cloud-scale and scene-scale changes to congestus and cumulonimbus precipitation in the MC region using a suite of realistic large-domain (1950 x 1800 km), high-resolution ( $\Delta x = 1 \text{ km}$ ;  $\Delta z = 50 \text{ to } 300 \text{ m}$ ; 5

minute output), long-duration (~1 month) simulation experiments. The three experiments were identical except for their aerosol loading, which was increased between the LOW, CTL, and HIGH cases. Over one million total congestus and cumulonimbus clouds (CCCs) objects in which simulation were tracked using a convective cloud tracking algorithm. Using this suite of sensitivity experiments, we have drawn the following conclusions:

1. Domain-wide precipitation decreased by 3.4% as aerosol loading was increased between the LOW and HIGH cases, driven both by aerosol-induced radiative and microphysical changes between the three experiments. This decrease in precipitation was stronger over land (-13.5%) than over ocean (-1.65%), forced by the more rapid response of the land surface to changes in incoming radiation than the ocean. Aerosol loading therefore results in a shift in the convective precipitation frequency and magnitude between land and ocean, with the maritime regions being the beneficiaries in more polluted scenarios.
2. Despite the decrease in precipitation, more CCCs (+2.5%) were tracked as aerosol loading was increased, being primarily driven by a significant increase in terminal congestus clouds (+8.1%), while weak reductions in the frequency of cumulonimbus clouds (-1.3%) were also observed. The increase in congestus clouds is similar, although to a much smaller magnitude, to the results in van den Heever et al. (2011), but van den Heever et al. (2011) saw an increase in the number of cumulonimbus, contrary to what we see here.
3. Aerosol loading has little change on the organization of CCCs. Further, organized and isolated CCCs demonstrate the same, although be it very weak, trends in precipitation as aerosol loading increases.

While this study focused on CCC precipitation, cumulus clouds, the smallest of the three canonical cloud types found in the tropical atmosphere (Johnson et al. 1999), are also likely to be affected by varying aerosol concentrations. Any variation in the cumulus field could then feed back onto the two larger cloud types through impacts on premoistening of the boundary layer. However, substantially higher resolution simulations and observations are necessary to capture aerosol impacts on these clouds. Further, future work should explore the impact that the aerosol direct effect has on sea surface temperatures, especially in the extensive littoral areas in the MC.

## 5.5. Tables and Figures

Table 5.1: Percent differences of several domain-wide variables between the HIGH and LOW experiments (left; negative values indicate less in HIGH, while positive values indicate more in HIGH) and the CTL and LOW experiments (right).

<b>Value</b>	<b>HIGH-LOW % Difference</b>	<b>CTL-LOW % Difference</b>
Total Precipitation	-3.41 %	-1.63%
Ocean Precipitation	-1.65%	-0.50%
Land Precipitation	-13.5%	-8.12%
Number of CCCs	+2.45%	+0.72%
Number of nonprecipitating CCCs	+10.7%	+4.63%
Total Cell Time Precipitating	-4.29%	-2.00%
Number of terminal congestus CCCs	+8.06%	+3.28%
Number of cumulonimbus CCCs	-1.26%	-1.00%

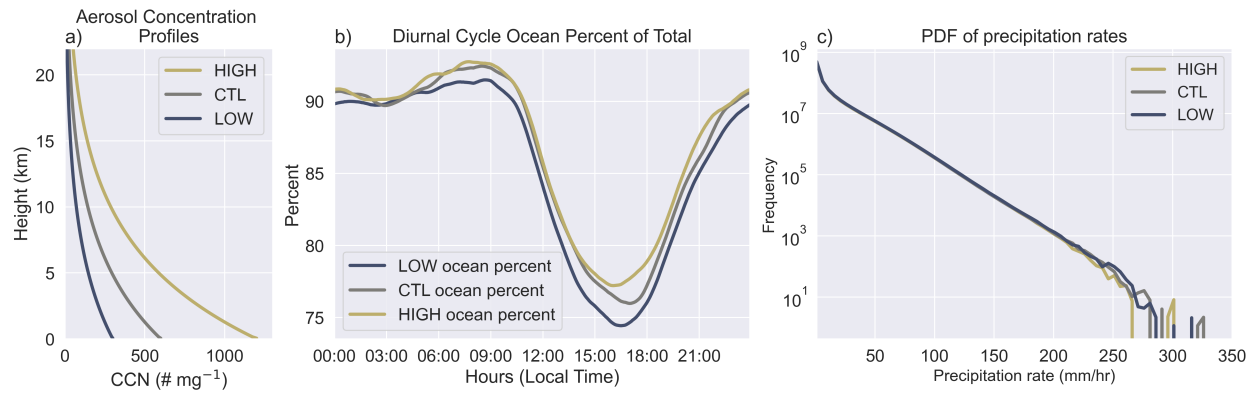


Figure 5.1: Domain-wide changes between the three simulation experiments. a) Static aerosol concentration (number mg<sup>-1</sup>) profile with height (km); b) Average diurnal cycle (time in local time) of percent of the total precipitation that occurs over water (i.e., a value of 100% indicates that all precipitation occurs over ocean); c) Probability distribution function of domain-wide precipitation rates (mm hr<sup>-1</sup>) for each of the three experiments

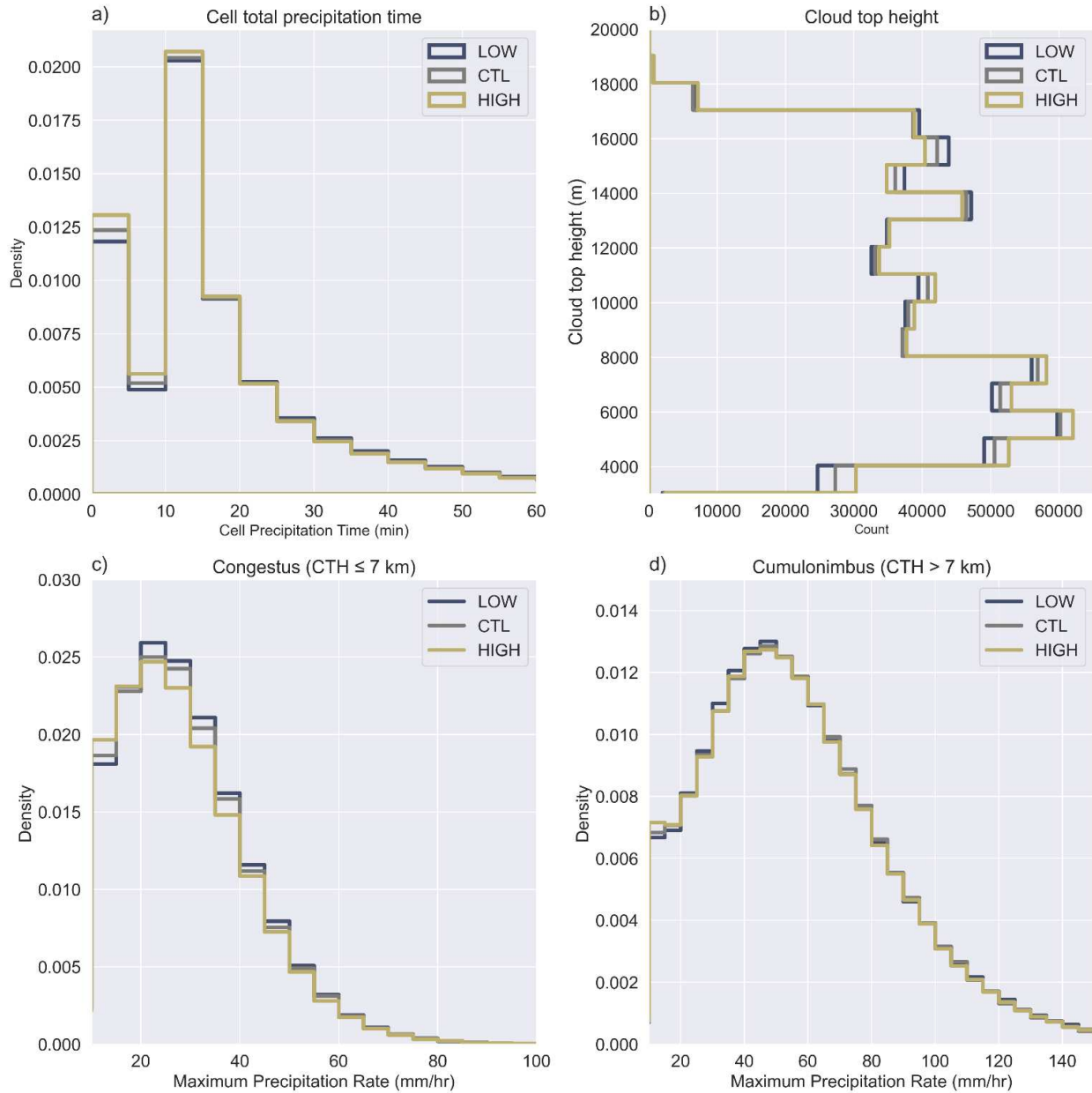


Figure 5.2: Cloud-by-cloud statistics of CCCs and their rainfall, using the tracked clouds from the *tobac* tracking algorithm. a) Total tracked CCC precipitation time histogram binned into 5 minute bins for each of the three experiments; b) maximum tracked CCC cloud top height histogram, binned into 1 km bins, for each of the three experiments; c) histogram of cell maximum precipitation rate for terminal congestus clouds (defined as those having lifetime maximum cloud top heights less than or equal to 7 km) for each of the three experiments; d) As

in c, but for cumulonimbus clouds (lifetime maximum cloud top heights greater than 7 km). Note the difference in scale along the ordinate and abscissa compared to c.

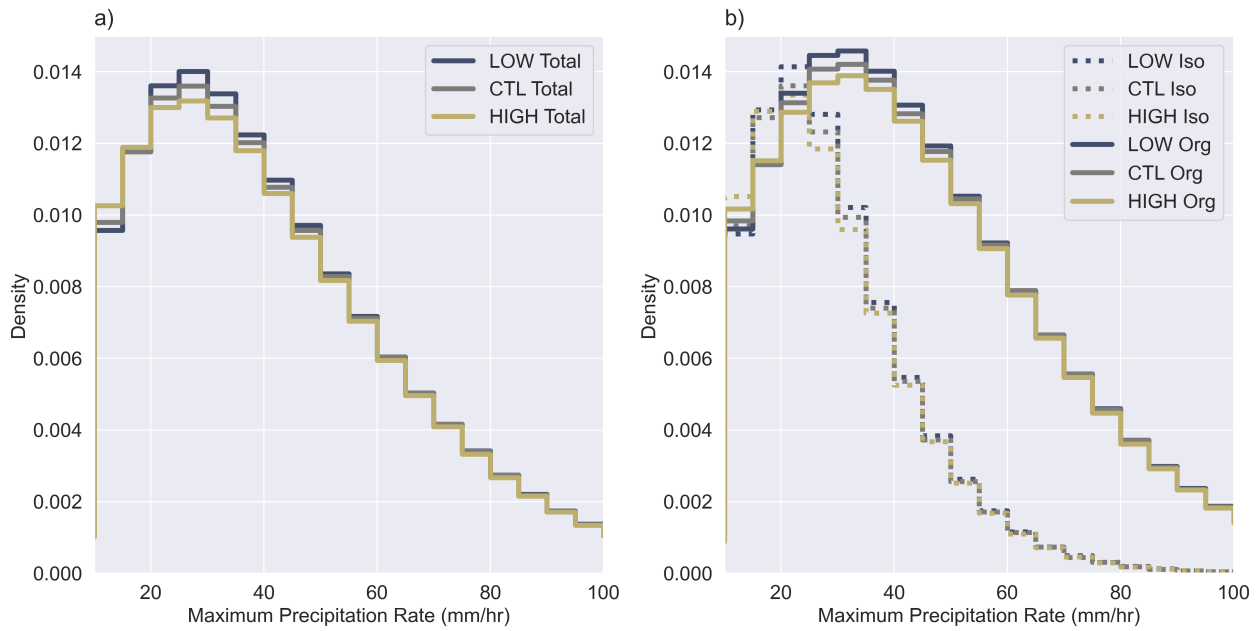


Figure 5.3: Statistics of CCCs, stratified by organized and isolated precipitation a) Histogram of cell maximum precipitation rate for all tracked CCCs, binned into 5 mm hr<sup>-1</sup> bins b) As in a, but divided into organized (solid lines) and isolated (dashed lines) CCCs.

## CHAPTER 6: CONCLUSIONS

### 6.1. Summary of Studies

Convective clouds are critical contributors to both weather and climate. While the basic environmental properties leading to their formation and maintenance are broadly known, there is currently no unified theory linking joint changes in the environment to changes in convective cloud properties. Better tools, such as observing platforms and tracking software, are first necessary to better quantify and track convective clouds and the environments in which they live. With these improved tools, we can then begin to examine the relationships between convective clouds and their environments regionally, before assessing such relationships on a global scale. The overarching goal of the research presented in this dissertation has therefore been to examine the combinations of environmental parameters that produce convective clouds. Two tools were examined to enhance our capabilities to do so: (1) drones with the ability to accurately sample temperature, pressure, and humidity near convective clouds were evaluated, and (2) enhancements were made to a cloud object tracking package capable of identifying and tracking any atmospheric phenomenon, including convective clouds. This enhanced tracking package was then utilized to: (1) examine how tropical convective cloud intensity, organization, and morphology vary with joint changes to the thermodynamic and dynamic properties of the tropical convective environment; and (2) investigate how tropical convective precipitation varies both locally and regionally with changes to the aerosol environment.

The goal of the first study presented in this dissertation (Chapter 2) was to examine the accuracy of eight different temperature, pressure, and relative humidity sensor siting locations on

a multirotor drone. Using a total of 82 flights, including 9 at night, the following conclusions were drawn:

1. All sensor siting locations produced temperature data within 2 K of the more traditional but fixed tethersonde measurement, with the best location (on the landing gear, directly under the propeller) reaching an accuracy of  $-0.83 \text{ K} \leq T \leq +0.61 \text{ K}$
2. When examining temperature *temporal* gradients (e.g., the change in temperature over 1 minute), the accuracy of the best sensor siting location improves slightly to  $-0.57 \text{ K} \leq T \leq +0.63 \text{ K}$ .
3. Dewpoint temperature observations were overall worse than air temperature observations, but when examining temporal gradients, the accuracy of all tested drone sensor positions was within  $\pm 2.0 \text{ K}$ .
4. Pressure errors were found to vary with wind speed

Overall, this study validates the use of multirotor drones for sampling convective boundary layer environments including storm outflows, and gives confidence intervals for their measurements, enabling their future use in research.

In the second study (Chapter 3), enhancements to the Tracking and Object-Based Analysis of Clouds (*tobac*) were presented. In this study, the following new or enhanced features were added:

1. The ability to rapidly identify and track atmospheric phenomena within large datasets, with over a 1,000,000% improvement in tracking speed on the dataset used in Chapter 4.

2. Identifying, tracking, and segmenting atmospheric phenomena can now be performed in three spatial dimensions, and can be done so in datasets with varying spatial coordinates, such as stretched vertical grids.
3. Periodic boundary and zonal global tracking capabilities have now been added, enabling *tobac*'s use across a wide variety of both observational and modeling datasets

This study significantly enhances *tobac*'s capabilities and enables it to be the universal atmospheric tracking tool of the future. *tobac* is already been used in NASA's Cloud, Aerosol, and Monsoon Processes Philippines Experiment (CAMP<sup>2</sup>Ex; Reid et al. 2022) field campaign and the Department of Energy's (DOE) Tracking Aerosol Convection Interactions Experiment (TRACER) field campaign, and is slated for use in NASA's upcoming Atmospheric Observing System (AOS) and Investigation of Convective Updrafts (INCUS) missions.

The third study in this dissertation (Chapter 4) employed some of the *tobac* enhancements to examine how dynamic and thermodynamic environmental conditions influence convective properties in the tropical atmosphere. Using a database of nearly 200,000 clouds, the following conclusions were made:

1. While previous studies have demonstrated the importance of CAPE and PW in convective development, this study demonstrate that large values of **both** CAPE and PW are necessary to support the strongest convective cloud vertical velocities found in the tropical atmosphere. Strength in either CAPE or PW alone is not sufficient to produce clouds with the strongest updrafts sampled.
2. Many of the convective clouds that produce the strongest vertical velocities produce the strongest surface precipitation rates (80.9%), but only 67% of the convective clouds producing the strongest surface precipitation rates produce the strongest vertical

velocities. The primary differentiator between strongly precipitating convective clouds and moderate or weakly precipitating clouds is available moisture.

3. Tropical convective cloud organization is primarily correlated with strong wind shear, and organized convective clouds tend to have higher cloud tops and live longer.
4. Weaker wind shear is more likely to lead to linearly oriented organized convective cloud systems than nonlinear cloud systems.

This study demonstrates the sensitivity of convective clouds to local environments that are supported by a variety of different large-scale synoptic patterns and links the variation in convective environments with variations in convective cloud properties, a first step toward building an understanding of the relationship between convective clouds and their environments globally.

The final study in this dissertation (Chapter 5) used a similar methodology as in Chapter 4 to elucidate the impacts of aerosol particles on the cloud properties and precipitation of congestus and cumulonimbus clouds (CCCs) in the tropics. The following relationships were found in association with increased aerosol loading:

1. A decrease in domain-wide precipitation by up to 3.4%, with the majority of this decrease occurring in terminal congestus clouds (clouds with lifetime cloud top heights lower than 7 km) and little impacts on the precipitation of cumulonimbus clouds
2. An increase in the total number of tracked CCCs (+2.5%), but an overall decrease in cloud top heights, with an increase in the number of congestus clouds (+8%) and fewer cumulonimbus clouds (lifetime cloud top height greater than 7 km; -1.26%)

3. An increase in the number of nonprecipitating clouds (+10.7%) and a decrease in the total amount of time that tracked congestus and cumulonimbus clouds spend precipitating (-4.29%)
4. Little difference to the organization of congestus and cumulonimbus clouds.

This study demonstrates the relationships between aerosol particles and changes to precipitation both on the scales of an individual cloud and for a scene of clouds.

## **6.2 Implications of this research and future work**

The research presented in this dissertation has advanced our understanding of the environments that produce convective clouds both through developing tools to sample these environments, and by examining the relationship between convective environments and the clouds that they produce within high-resolution, long-duration, large-domain numerical simulations. However, many new questions have been raised by this research, including the following:

- How do the measurements from small (i.e., quad-rotor) drones compare to measurements made on the larger drones used in the study in Chapter 2?
- Will forced aspiration and/or shielding produce more consistent pressure, temperature, and humidity observations on multirotor drones?
- How can features that are defined relative to a larger field, such as cold pools, be tracked?
- Can multiple variables (such as updrafts and downdrafts) be used simultaneously to identify and track a single convective cloud over its entire lifecycle?
- How do observations compare to the numerical modeling results in Chapters 4 and 5?

- Why are the tropical linear systems in Chapter 4 generally associated with weaker wind shear than nonlinear systems?
- How does the environment-convective cloud relationship vary globally?
- How does the aerosol environment influence the relationship between thermodynamic and dynamic environmental conditions and convective cloud properties?
- How does the relationship between environmental conditions and convective clouds vary as a function of diurnal cycle?

As we enter the era where individual convective clouds are able to be observed and simulated at high temporal and spatial resolutions, enhancing our understanding of the relationships between environments and convective clouds is possible. This dissertation represents some new steps toward achieving that overarching goal.

This research, especially the improvements to *tobac* discussed in Chapter 3 and the subsequent novel approach towards quantifying convective environments, presents important implications for upcoming observational missions and modeling capabilities. The periodic boundary condition support added in *tobac*, in particular, represents the first steps toward true global tracking of atmospheric phenomena. This is becoming particularly important as global convection resolving models are already being developed and becoming more widely used. Further, the statistical approach leveraging this *tobac* tracking algorithm as performed in Chapters 4 and 5 can be used to enhance the capabilities of the upcoming NASA INCUS and AOS missions. Finally, the use of high-resolution, long-duration, large-area numerical model simulations, as in Chapters 4 and 5, coupled to observing system simulators to produce

Observing System Simulation Experiments (OSSEs), will also allow for a detailed comparison between model output and observations, enabling new understanding of model performance.

## REFERENCES

- Albrecht, B. A., 1989: Aerosols, Cloud Microphysics, and Fractional Cloudiness. *Science*, **245**, 1227–1230.
- Allan, D. B., T. Caswell, N. C. Keim, and C. M. van der Wel, 2019: *soft-matter/trackpy: Trackpy v0.4.2*.
- , ———, ———, ———, and R. W. Verweij, 2021: *soft-matter/trackpy: Trackpy v0.5.0*.
- Altartatz, O., I. Koren, T. Reisin, A. Kostinski, G. Feingold, Z. Levin, and Y. Yin, 2008: Aerosols' influence on the interplay between condensation, evaporation and rain in warm cumulus cloud. *Atmos. Chem. Phys.*, **8**, 15–24.
- Andreae, M. O., D. Rosenfeld, P. Artaxo, A. A. Costa, G. P. Frank, K. M. Longo, and M. a. F. Silva-Dias, 2004: Smoking Rain Clouds over the Amazon. *Science*, **303**, 1337–1342.
- Arya, S. P., 2001: *Introduction to micrometeorology*. 2nd ed. Academic Press, 420 pp.
- Atwood, S. A., and Coauthors, 2017: Size-resolved aerosol and cloud condensation nuclei (CCN) properties in the remote marine South China Sea – Part 1: Observations and source classification. *Atmos. Chem. Phys.*, **17**, 1105–1123.
- Austin, J. M., 1948: A NOTE ON CUMULUS GROWTH IN A NONSATURATED ENVIRONMENT. *J. Atmos. Sci.*, **5**, 103–107.
- Baldauf, M., A. Seifert, J. Förstner, D. Majewski, M. Raschendorfer, and T. Reinhardt, 2011: Operational Convective-Scale Numerical Weather Prediction with the COSMO Model: Description and Sensitivities. *Mon. Weather Rev.*, **139**, 3887–3905.
- Barbieri, L., and Coauthors, 2019/1: Intercomparison of Small Unmanned Aircraft System (sUAS) Measurements for Atmospheric Science during the LAPSE-RATE Campaign. *Sensors*, **19**, 2179.
- Barth, M. C., and Coauthors, 2015: The Deep Convective Clouds and Chemistry (DC3) Field Campaign. *Bull. Am. Meteorol. Soc.*, **96**, 1281–1309.
- Barthlott, C., and C. Hoose, 2018: Aerosol Effects on Clouds and Precipitation over Central Europe in Different Weather Regimes. *Journal of Atmospheric Sciences*, **75**, 4247–4264.
- , A. Zarbo, T. Matsunobu, and C. Keil, 2022: Importance of aerosols and shape of the cloud droplet size distribution for convective clouds and precipitation. *Atmos. Chem. Phys.*, **22**, 2153–2172.

- Becker, T., C. S. Bretherton, C. Hohenegger, and B. Stevens, 2018: Estimating bulk entrainment with unaggregated and aggregated convection. *Geophys. Res. Lett.*, **45**, 455–462.
- Bergemann, M., and C. Jakob, 2016: How important is tropospheric humidity for coastal rainfall in the tropics? *Geophys. Res. Lett.*, **43**, 5860–5868.
- Bhat, G. S., J. Srinivasan, and S. Gadgil, 1996: Tropical Deep Convection, Convective Available Potential Energy and Sea Surface Temperature. *Journal of the Meteorological Society of Japan. Ser. II*, **74**, 155–166.
- Bigelow, F. H., 1908: Studies on the phenomena of the evaporation of water over lakes and reservoirs. *Mon. Weather Rev.*, **36**, 437–445.
- Brady, J. M., M. D. Stokes, J. Bonnardel, and T. H. Bertram, 2016: Characterization of a Quadrotor Unmanned Aircraft System for Aerosol-Particle-Concentration Measurements. *Environ. Sci. Technol.*, **50**, 1376–1383.
- Bukowski, J., and S. C. van den Heever, 2021: Direct radiative effects in haboobs. *J. Geophys. Res.*, **126**, <https://doi.org/10.1029/2021jd034814>.
- Carbajo Fuertes, F., L. Wilhelm, and F. Porté-Agel, 2019: Multirotor UAV-based platform for the measurement of atmospheric turbulence: validation and signature detection of tip vortices of wind turbine blades. *J. Atmos. Ocean. Technol.*, <https://doi.org/10.1175/JTECH-D-17-0220.1>.
- Cecil, D. J., S. J. Goodman, D. J. Boccippio, E. J. Zipser, and S. W. Nesbitt, 2005: Three Years of TRMM Precipitation Features. Part I: Radar, Radiometric, and Lightning Characteristics. *Mon. Weather Rev.*, **133**, 543–566.
- Charlson, R. J., and M. J. Pilat, 1969: Climate: The Influence of Aerosols. *J. Appl. Meteorol. Climatol.*, **8**, 1001–1002.
- Chen, S., N. Z. Wong, D. Ma, P. W. Chan, and Z. Kuang, 2021: Dependence of precipitation on precipitable water vapor over the maritime continent and implications to the madden-Julian oscillation. *Geophys. Res. Lett.*, **48**, <https://doi.org/10.1029/2021gl094648>.
- Cione, J. J., E. A. Kalina, E. W. Uhlhorn, A. M. Farber, and B. Damiano, 2016: Coyote unmanned aircraft system observations in Hurricane Edouard (2014). *Life Support Biosph. Sci.*, **3**, 370–380.
- Coelho, L. P., 2017: Jug: Software for parallel reproducible computation in python. *J. Open Res. Softw.*, **5**, <https://doi.org/10.5334/jors.161>.
- Cotton, W. R., and R. A. Anthes, eds., 1992: Chapter 2 Fundamental Equations Governing Cloud Processes. *International Geophysics*, Vol. 44 of, Academic Press, 13–46.
- Cotton, W. R., and Coauthors, 2003: RAMS 2001: Current status and future directions.

*Meteorol. Atmos. Phys.*, **82**, 5–29.

Crewe, T. L., D. Kendal, and H. A. Campbell, 2020: Motivations and fears driving participation in collaborative research infrastructure for animal tracking. *PLoS One*, **15**, e0241964.

Cruz, F. T., G. T. Narisma, M. Q. Villafuerte, K. U. Cheng Chua, and L. M. Olaguera, 2013: A climatological analysis of the southwest monsoon rainfall in the Philippines. *Atmos. Res.*, **122**, 609–616.

Dawe, J. T., and P. H. Austin, 2012: Statistical analysis of an LES shallow cumulus cloud ensemble using a cloud tracking algorithm. *Atmos. Chem. Phys.*, **12**, 1101–1119.

De Bothezat, G., 1930: Helicopter. *US Patent*.

Dexheimer, D., M. Apple, A. Bendure, D. Callow, C. Longbottom, D. Novick, and C. Wilson, 2018: *Joint UAS-Balloon Activities (JUBA) Field Campaign Report*. ARM Climate Research Facility, Pacific Northwest National Laboratory, Richland, WA, <https://www.osti.gov/biblio/1422521> (Accessed April 15, 2019).

Dickerson, R. R., and Coauthors, 1987: Thunderstorms: an important mechanism in the transport of air pollutants. *Science*, **235**, 460–465.

Dixon, M., and G. Wiener, 1993: TITAN: Thunderstorm Identification, Tracking, Analysis, and Nowcasting—A Radar-based Methodology. *J. Atmos. Ocean. Technol.*, **10**, 785–797.

Douville, H., K. Raghavan, J. Renwick, R.P. Allan, P.A. Arias, M. Barlow, R. Cerezo-Mota, A. Cherchi, T.Y. Gan, J. Gergis, D. Jiang, A. Khan, W. Pokam Mba, D. Rosenfeld, J. Tierney, and O. Zolina, Water Cycle Changes. *Climate Change 2021: The Physical Science Basis. Contribution of Working Group I to the Sixth Assessment Report of the Intergovernmental Panel on Climate Change*, Masson-Delmotte, V., P. Zhai, A. Pirani, S.L. Connors, C. Péan, S. Berger, N. Caud, Y. Chen, L. Goldfarb, M.I. Gomis, M. Huang, K. Leitzell, E. Lonnoy, J.B.R. Matthews, T.K. Maycock, T. Waterfield, O. Yelekçi, R. Yu, and B. Zhou, Ed., Cambridge University Press.

Drager, A. J., and S. C. van den Heever, 2017: Characterizing convective cold pools. *Journal of Advances in Modeling Earth Systems*, **9**, 1091–1115.

—, L. D. Grant, and S. C. van den Heever, 2020: Cold Pool Responses to Changes in Soil Moisture. *Journal of Advances in Modeling Earth Systems*, **12**, e2019MS001922.

Dumas, E., M. S. Buban, and C. B. Baker, 2017: Small Unmanned Aircraft System (sUAS) measurements during the 2017 Verifications of the Origins of Rotation in Tornadoes Experiment Southeast (VORTEX-SE). <https://doi.org/10.7289/v5/tm-oar-ar1-274>.

Elston, J., B. Argrow, M. Stachura, D. Weibel, D. Lawrence, and D. Pope, 2014: Overview of Small Fixed-Wing Unmanned Aircraft for Meteorological Sampling. *J. Atmos. Ocean. Technol.*, **32**, 97–115.

- Endo, N., J. Matsumoto, and T. Lwin, 2009: Trends in Precipitation Extremes over Southeast Asia. *SOLAIA*, **5**, 168–171.
- Engerer, N. A., D. J. Stensrud, and M. C. Coniglio, 2008: Surface Characteristics of Observed Cold Pools. *Mon. Weather Rev.*, **136**, 4839–4849.
- Fan, J., Y. Zhang, Z. Li, J. Hu, and D. Rosenfeld, 2020: Urbanization-induced land and aerosol impacts on sea-breeze circulation and convective precipitation. *Atmos. Chem. Phys.*, **20**, 14163–14182.
- Feng, Z., S. Hagos, A. K. Rowe, C. D. Burleyson, M. N. Martini, and S. P. de Szoeke, 2015: Mechanisms of convective cloud organization by cold pools over tropical warm ocean during the AMIE/DYNAMO field campaign. *Journal of Advances in Modeling Earth Systems*, **7**, 357–381.
- Fuchs, B. R., and Coauthors, 2015: Environmental controls on storm intensity and charge structure in multiple regions of the continental United States. *J. Geophys. Res.*, **120**, 6575–6596.
- Fuchs, M., and C. B. Tanner, 1965: Radiation Shields for Air Temperature Thermometers. *J. Appl. Meteorol.*, **4**, 544–547.
- Gallus, W. A., N. A. Snook, and E. V. Johnson, 2008: Spring and Summer Severe Weather Reports over the Midwest as a Function of Convective Mode: A Preliminary Study. *Weather Forecast.*, **23**, 101–113.
- Gambheer, A. V., and G. S. Bhat, 2000: Life Cycle Characteristics of Deep Cloud Systems over the Indian Region Using INSAT-1B Pixel Data. *Mon. Weather Rev.*, **128**, 4071–4083.
- Geerts, B., and Coauthors, 2017: Community Workshop on Developing Requirements for In Situ and Remote Sensing Capabilities in Convective and Turbulent Environments (C-RITE). *UCAR/NCAR Earth Observing Laboratory*, <https://doi.org/10.5065/d6db80kr>.
- , and Coauthors, 2018: Recommendations for In Situ and Remote Sensing Capabilities in Atmospheric Convection and Turbulence. *Bull. Am. Meteorol. Soc.*, **99**, 2463–2470.
- Gill, A. E., and E. M. Rasmusson, 1983: The 1982–83 climate anomaly in the equatorial Pacific. *Nature*, **306**, 229–234.
- Grabowski, W. W., 2006: Indirect Impact of Atmospheric Aerosols in Idealized Simulations of Convective–Radiative Quasi Equilibrium. *J. Clim.*, **19**, 4664–4682.
- Grabowski, W. W., and M. W. Moncrieff, 2004: Moisture–convection feedback in the tropics. *Quart. J. Roy. Meteor. Soc.*, **130**, 3081–3104.
- , and H. Morrison, 2011: Indirect Impact of Atmospheric Aerosols in Idealized Simulations of Convective–Radiative Quasi Equilibrium. Part II: Double-Moment Microphysics. *J. Clim.*, **24**,

1897–1912.

Grandey, B. S., P. Stier, and T. M. Wagner, 2013: Investigating relationships between aerosol optical depth and cloud fraction using satellite, aerosol reanalysis and general circulation model data. *Atmos. Chem. Phys.*, **13**, 3177–3184.

Grant, L. D., and S. C. van den Heever, 04/2015: Cold Pool and Precipitation Responses to Aerosol Loading: Modulation by Dry Layers. *J. Atmos. Sci.*, **72**, 1398–1408.

———, T. P. Lane, and S. C. van den Heever, 08/2018: The Role of Cold Pools in Tropical Oceanic Convective Systems. *J. Atmos. Sci.*, **75**, 2615–2634.

———, M. W. Moncrieff, T. P. Lane, and S. C. Heever, 2020: Shear-parallel tropical convective systems: Importance of cold pools and wind shear. *Geophys. Res. Lett.*, **47**, <https://doi.org/10.1029/2020gl087720>.

Greene, B. R., A. R. Segales, T. M. Bell, E. A. Pillar-Little, and P. B. Chilson, 2019/1: Environmental and Sensor Integration Influences on Temperature Measurements by Rotary-Wing Unmanned Aircraft Systems. *Sensors* , **19**, 1470.

———, ——, S. Waugh, S. Duthoit, and P. B. Chilson, 2018: Considerations for temperature sensor placement on rotary-wing unmanned aircraft systems. *Atmospheric Measurement Techniques*, **11**, 5519–5530.

Gropp, M. E., and C. E. Davenport, 2021: Python-Based Supercell Tracking for Coarse Temporal and Spatial Resolution Numerical Model Simulations. *J. Atmos. Ocean. Technol.*, **38**, 1551–1559.

Guo, H., J. E. Penner, M. Herzog, and H. Pawlowska, 2007: Examination of the aerosol indirect effect under contrasting environments during the ACE-2 experiment. *Atmos. Chem. Phys.*, **7**, 535–548.

Hagberg, A., P. Swart, and D. S Chult, 2008: *Exploring network structure, dynamics, and function using NetworkX*. Los Alamos National Lab.(LANL), Los Alamos, NM (United States), <https://www.osti.gov/servlets/purl/960616>.

Hamada, A., Y. N. Takayabu, C. Liu, and E. J. Zipser, 2015: Weak linkage between the heaviest rainfall and tallest storms. *Nat. Commun.*, **6**, 6213.

Hannah, W. M., 2017: Entrainment versus Dilution in Tropical Deep Convection. *J. Atmos. Sci.*, **74**, 3725–3747.

Harrington, J. Y., 1997: The effects of radiative and microphysical processes on simulated warm and transition season arctic stratus. <http://adsabs.harvard.edu/abs/1997PhDT.....45H> (Accessed February 3, 2020).

- Hartmann, D. L., H. H. Hendon, and R. A. Houze, 1984: Some Implications of the Mesoscale Circulations in Tropical Cloud Clusters for Large-Scale Dynamics and Climate. *J. Atmos. Sci.*, **41**, 113–121.
- Hassim, M. E. E., T. P. Lane, and W. W. Grabowski, 2016: The diurnal cycle of rainfall over New Guinea in convection-permitting WRF simulations. *Atmos. Chem. Phys.*, **16**, 161–175.
- van den Heever, S. C., G. G. Carrió, W. R. Cotton, P. J. DeMott, and A. J. Prenni, 2006: Impacts of Nucleating Aerosol on Florida Storms. Part I: Mesoscale Simulations. *J. Atmos. Sci.*, **63**, 1752–1775.
- , G. L. Stephens, and N. B. Wood, 2011: Aerosol Indirect Effects on Tropical Convection Characteristics under Conditions of Radiative–Convective Equilibrium. *J. Atmos. Sci.*, **68**, 699–718.
- , and Coauthors, 2021: The Colorado State University Convective CLOUD Outflows and UpDrafts Experiment (C3LOUD-Ex). *Bull. Am. Meteorol. Soc.*, **102**, E1283–E1305.
- Heikenfeld, M., P. J. Marinescu, M. Christensen, D. Watson-Parris, F. Senf, S. C. van den Heever, and P. Stier, 2019: tobac 1.2: towards a flexible framework for tracking and analysis of clouds in diverse datasets. *Geoscientific Model Development*, **12**, 4551–4570.
- Hemingway, B. L., A. E. Frazier, B. R. Elbing, and J. D. Jacob, 2017/9: Vertical Sampling Scales for Atmospheric Boundary Layer Measurements from Small Unmanned Aircraft Systems (sUAS). *Atmosphere*, **8**, 176.
- Hersbach, H., and Coauthors, 2020a: The ERA5 global reanalysis. *Quart. J. Roy. Meteor. Soc.*, **146**, 1999–2049.
- , and Coauthors, 2020b: The ERA5 global reanalysis. *Quart. J. Roy. Meteor. Soc.*, **146**, 1999–2049.
- Heus, T., and A. Seifert, 2013: Automated tracking of shallow cumulus clouds in large domain, long duration large eddy simulations. *Geosci. Model Dev.*, **6**, 1261–1273.
- Heus, T., H. J. J. Jonker, H. E. A. Van den Akker, E. J. Griffith, M. Koutek, and F. H. Post, 2009: A statistical approach to the life cycle analysis of cumulus clouds selected in a virtual reality environment. *J. Geophys. Res.*, **114**, <https://doi.org/10.1029/2008jd010917>.
- Hill, G. E., 1974: Factors Controlling the Size and Spacing of Cumulus Clouds as Revealed by Numerical Experiments. *J. Atmos. Sci.*, **31**, 646–673.
- Holloway, C. E., and J. David Neelin, 2009: Moisture Vertical Structure, Column Water Vapor, and Tropical Deep Convection. *J. Atmos. Sci.*, **66**, 1665–1683.
- , and ———, 2010: Temporal Relations of Column Water Vapor and Tropical Precipitation.

*J. Atmos. Sci.*, **67**, 1091–1105.

Houston, A. L., B. Argrow, J. Elston, J. Lahowetz, E. W. Frew, and P. C. Kennedy, 2011: The Collaborative Colorado–Nebraska Unmanned Aircraft System Experiment. *Bull. Am. Meteorol. Soc.*, **93**, 39–54.

———, R. J. Laurence, T. W. Nichols, S. Waugh, B. Argrow, and C. L. Ziegler, 2016: Intercomparison of Unmanned Aircraftborne and Mobile Mesonet Atmospheric Sensors. *J. Atmos. Ocean. Technol.*, **33**, 1569–1582.

Houze, R. A., and C.-P. Cheng, 1977: Radar Characteristics of Tropical Convection Observed During GATE: Mean Properties and Trends Over the Summer Season. *Mon. Weather Rev.*, **105**, 964–980.

Hoyer, S., and J. Hamman, 2017: xarray: N-D labeled Arrays and Datasets in Python. *J. Open Res. Softw.*, **5**, 10.

Hu, J., and Coauthors, 2019: Tracking and characterization of convective cells through their maturation into stratiform storm elements using polarimetric radar and lightning detection. *Atmos. Res.*, **226**, 192–207.

Humphrey, P. A., 1961: An Evaluation of the Aerometric Probe. *J. Air Pollut. Control Assoc.*, **11**, 362–383.

Igel, A. L., and S. C. Heever, 2021a: Invigoration or enervation of convective clouds by aerosols? *Geophys. Res. Lett.*, **48**, <https://doi.org/10.1029/2021gl093804>.

———, and ———, 2021b: Invigoration or enervation of convective clouds by aerosols? *Geophys. Res. Lett.*, **48**, <https://doi.org/10.1029/2021gl093804>.

Ilotoviz, E., A. Khain, A. V. Ryzhkov, and J. C. Snyder, 2018: Relationship between Aerosols, Hail Microphysics, and ZDR Columns. *J. Atmos. Sci.*, **75**, 1755–1781.

Inoue, T., M. Satoh, H. Miura, and B. Mapes, 2008: Characteristics of Cloud Size of Deep Convection Simulated by a Global Cloud Resolving Model over the Western Tropical Pacific. *Journal of the Meteorological Society of Japan*, **86A**, 1–15.

International Met Systems, 2018: *iMet-XQ: Atmospheric Sensor System for Rotary Wing UAV Integration Specifications*. [http://www.intermetssystems.com/ee/pdf/202020\\_iMet-XQ\\_161005.pdf](http://www.intermetssystems.com/ee/pdf/202020_iMet-XQ_161005.pdf).

Islam, A., A. L. Houston, A. Shankar, and C. Detweiler, 2019/1: Design and Evaluation of Sensor Housing for Boundary Layer Profiling Using Multirotors. *Sensors*, **19**, 2481.

Jacob, J. D., P. B. Chilson, A. L. Houston, and S. W. Smith, 2018/7: Considerations for Atmospheric Measurements with Small Unmanned Aircraft Systems. *Atmosphere*, **9**, 252.

- Jensen, M. P., and A. D. Del Genio, 2006: Factors Limiting Convective Cloud-Top Height at the ARM Nauru Island Climate Research Facility. *J. Clim.*, **19**, 2105–2117.
- Johnson, R. H., T. M. Rickenbach, S. A. Rutledge, P. E. Ciesielski, and W. H. Schubert, 1999: Trimodal Characteristics of Tropical Convection. *J. Clim.*, **12**, 2397–2418.
- Jones, W. K., M. W. Christensen, and P. Stier, 2022: A semi-Lagrangian method for detecting and tracking deep convective clouds in geostationary satellite observations. *Atmospheric Measurement Techniques Discussions*, <https://doi.org/10.5194/amt-2022-31>.
- Jourdain, N. C., A. S. Gupta, A. S. Taschetto, C. C. Ummenhofer, A. F. Moise, and K. Ashok, 2013: The Indo-Australian monsoon and its relationship to ENSO and IOD in reanalysis data and the CMIP3/CMIP5 simulations. *Clim. Dyn.*, **41**, 3073–3102.
- Kang, S., E.-S. Im, and E. A. B. Eltahir, 2019: Future climate change enhances rainfall seasonality in a regional model of western Maritime Continent. *Clim. Dyn.*, **52**, 747–764.
- Keenan, T., and Coauthors, 2000: The Maritime Continent — Thunderstorm Experiment (MCTEX): Overview and Some Results. *Bull. Am. Meteorol. Soc.*, **81**, 2433–2456.
- Kirkpatrick, C., E. W. McCaul, and C. Cohen, 2011: Sensitivities of Simulated Convective Storms to Environmental CAPE. *Mon. Weather Rev.*, **139**, 3514–3532.
- Klemp, J. B., and R. B. Wilhelmson, 1978: The Simulation of Three-Dimensional Convective Storm Dynamics. *J. Atmos. Sci.*, **35**, 1070–1096.
- Knight, S. M., G. M. Pitman, D. T. T. Flockhart, and D. R. Norris, 2019: Radio-tracking reveals how wind and temperature influence the pace of daytime insect migration. *Biol. Lett.*, **15**, 20190327.
- Koch, S. E., M. Fengler, P. B. Chilson, K. L. Elmore, B. Argrow, D. L. Andra, and T. Lindley, 2018: On the Use of Unmanned Aircraft for Sampling Mesoscale Phenomena in the Preconvective Boundary Layer. *J. Atmos. Ocean. Technol.*, **35**, 2265–2288.
- Konrad, T. G., M. L. Hill, J. R. Rowland, and J. H. Meyer, September–October 1970: A Small, Radio-Controlled Aircraft as a Platform for Meteorological Sensors. *APL Technical Digest*, **10**, 11–19.
- Koren, I., Y. J. Kaufman, D. Rosenfeld, L. A. Remer, and Y. Rudich, 2005: Aerosol invigoration and restructuring of Atlantic convective clouds: AEROSOL RESTRUCTURING CONVECTIVE CLOUDS. *Geophys. Res. Lett.*, **32**, <https://doi.org/10.1029/2005gl023187>.
- , G. Dagan, and O. Altaratz, 2014: From aerosol-limited to invigoration of warm convective clouds. *Science*, **344**, 1143–1146.

- van den Kroonenberg, A., T. Martin, M. Buschmann, J. Bange, and P. Vörsmann, 2008: Measuring the Wind Vector Using the Autonomous Mini Aerial Vehicle M2AV. *J. Atmos. Ocean. Technol.*, **25**, 1969–1982.
- Kruskal, J. B., 1956: On the Shortest Spanning Subtree of a Graph and the Traveling Salesman Problem. *Proc. Am. Math. Soc.*, **7**, 48–50.
- Kukulies, J., D. Chen, and J. Curio, 2021: The role of mesoscale convective systems in precipitation in the Tibetan plateau region. *J. Geophys. Res.*, **126**, <https://doi.org/10.1029/2021jd035279>.
- Kumar, V. V., A. Protat, C. Jakob, and P. T. May, 2014: On the Atmospheric Regulation of the Growth of Moderate to Deep Cumulonimbus in a Tropical Environment. *J. Atmos. Sci.*, **71**, 1105–1120.
- Lane, T. P., and M. W. Moncrieff, 2015: Long-Lived Mesoscale Systems in a Low–Convective Inhibition Environment. Part I: Upshear Propagation. *J. Atmos. Sci.*, **72**, 4297–4318.
- Lee, S. S., L. J. Donner, V. T. J. Phillips, and Y. Ming, 2008: The dependence of aerosol effects on clouds and precipitation on cloud-system organization, shear and stability. *JOURNAL OF GEOPHYSICAL RESEARCH-ATMOSPHERES*, **113**, <https://doi.org/10.1029/2007JD009224>.
- , ———, and J. E. Penner, 2010: Thunderstorm and stratocumulus: how does their contrasting morphology affect their interactions with aerosols? *Atmos. Chem. Phys.*, **10**, 6819–6837.
- Lee, T. J., 1992: The Impact of Vegetation on the Atmospheric Boundary Layer and Convective Storms. <https://ui.adsabs.harvard.edu/abs/1992PhDT.....244L>.
- Lee, T. R., M. Buban, E. Dumas, and C. B. Baker, 2019/1: On the Use of Rotary-Wing Aircraft to Sample Near-Surface Thermodynamic Fields: Results from Recent Field Campaigns. *Sensors*, **19**, 10.
- , ———, ———, and ———, 2017a: A New Technique to Estimate Sensible Heat Fluxes around Micrometeorological Towers Using Small Unmanned Aircraft Systems. *J. Atmos. Ocean. Technol.*, **34**, 2103–2112.
- , ———, ———, and ———, 2017b: A New Technique to Estimate Sensible Heat Fluxes around Micrometeorological Towers Using Small Unmanned Aircraft Systems. *J. Atmos. Ocean. Technol.*, **34**, 2103–2112.
- LeMone, M. A., G. M. Barnes, and E. J. Zipser, 1984: Momentum Flux by Lines of Cumulonimbus over the Tropical Oceans. *J. Atmos. Sci.*, **41**, 1914–1932.
- , E. J. Zipser, and S. B. Trier, 1998: The Role of Environmental Shear and Thermodynamic Conditions in Determining the Structure and Evolution of Mesoscale Convective Systems during TOGA COARE. *J. Atmos. Sci.*, **55**, 3493–3518.

- Li, Y., Y. Liu, Y. Chen, B. Chen, X. Zhang, W. Wang, Z. Shu, and Z. Huo, 2021: Characteristics of Deep Convective Systems and Initiation during Warm Seasons over China and Its Vicinity. *Remote Sensing*, **13**, 4289.
- Louf, V., C. Jakob, A. Protat, M. Bergemann, and S. Narsey, 2019: The relationship of cloud number and size with their large-scale environment in deep tropical convection. *Geophys. Res. Lett.*, **46**, 9203–9212.
- Luo, Z., G. Y. Liu, G. L. Stephens, and R. H. Johnson, 2009: Terminal versus transient cumulus congestus: A CloudSat perspective. *Geophys. Res. Lett.*, **36**, <https://doi.org/10.1029/2008gl036927>.
- MacHattie, L. B., 1965: Radiation Screens for Air Temperature Measurement. *Ecology*, **46**, 533–538.
- Mapes, B. E., 1993: Gregarious Tropical Convection. *J. Atmos. Sci.*, **50**, 2026–2037.
- Marinescu, P. J., and Coauthors, 2021: Impacts of Varying Concentrations of Cloud Condensation Nuclei on Deep Convective Cloud Updrafts—A Multimodel Assessment. *J. Atmos. Sci.*, **78**, 1147–1172.
- Marino, M., A. Fisher, R. Clothier, S. Watkins, S. Prudden, and C. S. Leung, 2015: An Evaluation of Multi-Rotor Unmanned Aircraft as Flying Wind Sensors. *International Journal of Micro Air Vehicles*, **7**, 285–299.
- Masunaga, H., 2013: A Satellite Study of Tropical Moist Convection and Environmental Variability: A Moisture and Thermal Budget Analysis. *J. Atmos. Sci.*, **70**, 2443–2466.
- May, R., S. Arms, P. Marsh, E. Bruning, J. Leeman, and Z. Bruick, 2020: *MetPy: A Python Package for Meteorological Data*. UCAR/NCAR - Unidata,.
- McGee, C. J., and S. C. van den Heever, 2014: Latent Heating and Mixing due to Entrainment in Tropical Deep Convection. *J. Atmos. Sci.*, **71**, 816–832.
- Miller, D., and J. M. Fritsch, 1991: Mesoscale Convective Complexes in the Western Pacific Region. *Mon. Weather Rev.*, **119**, 2978–2992.
- Neale, R., and J. Slingo, 2003: The Maritime Continent and Its Role in the Global Climate: A GCM Study. *J. Clim.*, **16**, 834–848.
- Noppel, H., U. Blahak, A. Seifert, and K. D. Beheng, 2010: Simulations of a hailstorm and the impact of CCN using an advanced two-moment cloud microphysical scheme. *Atmos. Res.*, **96**, 286–301.
- Núñez Ocasio, K. M., J. L. Evans, and G. S. Young, 2020: Tracking Mesoscale Convective

Systems that are Potential Candidates for Tropical Cyclogenesis. *Mon. Weather Rev.*, **148**, 655–669.

de Oliveira, F. P., and M. D. Oyama, 2015: Antecedent Atmospheric Conditions Related to Squall-Line Initiation over the Northern Coast of Brazil in July. *Weather Forecast.*, **30**, 1254–1264.

Palomaki, R. T., N. T. Rose, M. van den Bossche, T. J. Sherman, and S. F. J. De Wekker, 2017: Wind Estimation in the Lower Atmosphere Using Multirotor Aircraft. *J. Atmos. Ocean. Technol.*, **34**, 1183–1191.

Park, J. M., S. C. Heever, A. L. Igel, L. D. Grant, J. S. Johnson, S. M. Saleeby, S. D. Miller, and J. S. Reid, 2020: Environmental controls on tropical Sea Breeze convection and resulting aerosol redistribution. *J. Geophys. Res.*, **125**, e2019JD031699.

Parker, M. D., and R. H. Johnson, 2000: Organizational Modes of Midlatitude Mesoscale Convective Systems. *Mon. Weather Rev.*, **128**, 3413–3436.

Peters, J. M., H. Morrison, A. C. Varble, W. M. Hannah, and S. E. Giangrande, 2020: Thermal Chains and Entrainment in Cumulus Updrafts. Part II: Analysis of Idealized Simulations. *J. Atmos. Sci.*, **77**, 3661–3681.

Plant, R. S., 2009: Statistical properties of cloud lifecycles in cloud-resolving models. *Atmos. Chem. Phys.*, **9**, 2195–2205.

Posselt, D. J., F. He, J. Bukowski, and J. S. Reid, 2019: On the Relative Sensitivity of a Tropical Deep Convective Storm to Changes in Environment and Cloud Microphysical Parameters. *J. Atmos. Sci.*, **76**, 1163–1185.

Ramage, C. S., 1968: ROLE OF A TROPICAL “MARITIME CONTINENT” IN THE ATMOSPHERIC CIRCULATION. *Mon. Weather Rev.*, **96**, 365–370.

Ratcliffe, C. A., and E. M. Sheen, 1964: An Automatic Data Collection System for Meteorological Tower Instrumentation. *J. Appl. Meteorol.*, **3**, 807–809.

Rauniyar, S. P., and K. J. E. Walsh, 2011: Scale Interaction of the Diurnal Cycle of Rainfall over the Maritime Continent and Australia: Influence of the MJO. *J. Clim.*, **24**, 325–348.

Raut, B. A., R. Jackson, M. Picel, S. M. Collis, M. Bergemann, and C. Jakob, 2021: An Adaptive Tracking Algorithm for Convection in Simulated and Remote Sensing Data. *J. Appl. Meteorol. Climatol.*, **60**, 513–526.

Reid, J. S., and Coauthors, 2015: Observations of the temporal variability in aerosol properties and their relationships to meteorology in the summer monsoonal South China Sea/East Sea: the scale-dependent role of monsoonal flows, the Madden–Julian Oscillation, tropical cyclones, squall lines and cold pools. *Atmos. Chem. Phys.*, **15**, 1745–1768.

- Reynolds, R. W., T. M. Smith, C. Liu, D. B. Chelton, K. S. Casey, and M. G. Schlax, 2007: Daily High-Resolution-Blended Analyses for Sea Surface Temperature. *J. Clim.*, **20**, 5473–5496.
- Riehl, H., and J. S. Malkus, 1958: On the Heat Balance in the Equatorial Trough Zone. *Geophysica*, **6**, 503–538.
- Riganti, C. J., and A. L. Houston, 2017: Rear-Flank Outflow Dynamics and Thermodynamics in the 10 June 2010 Last Chance, Colorado, Supercell. *Mon. Weather Rev.*, **145**, 2487–2504.
- Riley Dellaripa, E. M., E. Maloney, and S. C. van den Heever, 2018: Wind–Flux Feedbacks and Convective Organization during the November 2011 MJO Event in a High-Resolution Model. *J. Atmos. Sci.*, **75**, 57–84.
- Riley, E. M., B. E. Mapes, and S. N. Tulich, 2011: Clouds Associated with the Madden–Julian Oscillation: A New Perspective from CloudSat. *J. Atmos. Sci.*, **68**, 3032–3051.
- Ritter, B., and J.-F. Geleyn, 1992: A Comprehensive Radiation Scheme for Numerical Weather Prediction Models with Potential Applications in Climate Simulations. *Mon. Weather Rev.*, **120**, 303–325.
- Rotunno, R., J. B. Klemp, and M. L. Weisman, 1988: A Theory for Strong, Long-Lived Squall Lines. *J. Atmos. Sci.*, **45**, 463–485.
- Rowland, J. R., 1973: Intensive Probing of a Clear Air Convective Field by Radar and Instrumented Drone Aircraft. *J. Appl. Meteorol.*, **12**, 149–155.
- Ruppert, J. H., and R. H. Johnson, 2015: Diurnally Modulated Cumulus Moistening in the Preonset Stage of the Madden–Julian Oscillation during DYNAMO. *J. Atmos. Sci.*, **72**, 1622–1647.
- Rypina, I. I., A. Kirincich, S. Lentz, and M. Sundermeyer, 2016: Investigating the Eddy Diffusivity Concept in the Coastal Ocean. *J. Phys. Oceanogr.*, **46**, 2201–2218.
- Saleeby, S. M., and S. C. van den Heever, 2013: Developments in the CSU-RAMS Aerosol Model: Emissions, Nucleation, Regeneration, Deposition, and Radiation. *J. Appl. Meteorol. Climatol.*, **52**, 2601–2622.
- , S. R. Herbener, S. C. van den Heever, and T. L’Ecuyer, 2015: Impacts of Cloud Droplet–Nucleating Aerosols on Shallow Tropical Convection. *J. Atmos. Sci.*, **72**, 1369–1385.
- Schafer, R., P. T. May, T. D. Keenan, K. McGuffie, W. L. Ecklund, P. E. Johnston, and K. S. Gage, 2001: Boundary Layer Development over a Tropical Island during the Maritime Continent Thunderstorm Experiment. *J. Atmos. Sci.*, **58**, 2163–2179.
- Schiro, K. A., J. David Neelin, D. K. Adams, and B. R. Lintner, 2016: Deep Convection and

Column Water Vapor over Tropical Land versus Tropical Ocean: A Comparison between the Amazon and the Tropical Western Pacific. *J. Atmos. Sci.*, **73**, 4043–4063.

Seifert, A., C. Köhler, and K. D. Beheng, 2012: Aerosol-cloud-precipitation effects over Germany as simulated by a convective-scale numerical weather prediction model. *Atmos. Chem. Phys.*, **12**, 709–725.

Sheffield, A. M., S. M. Saleeby, and S. C. van den Heever, 2015: Aerosol-induced mechanisms for cumulus congestus growth. *J. Geophys. Res. D: Atmos.*, **120**, 8941–8952.

Sherman, D. J., 1987: The Passage of a Weak Thunderstorm Downburst over an Instrumented Tower. *Mon. Weather Rev.*, **115**, 1193–1205.

Shige, S., and T. Satomura, 2001: Westward Generation of Eastward-Moving Tropical Convective Bands in TOGA COARE. *J. Atmos. Sci.*, **58**, 3724–3740.

Shuqing, M., W. Gai, P. Yi, and W. Ling, 1999: An Analytical Method for Wind Measurements by a Mini-Aircraft. *Chinese Journal of Atmospheric Sciences*, **23**, 377–284.

Singarayer, J. S., J. L. Bamber, and P. J. Valdes, 2006: Twenty-First-Century Climate Impacts from a Declining Arctic Sea Ice Cover. *J. Clim.*, **19**, 1109–1125.

Slingo, A., and J. M. Slingo, 1988: The response of a general circulation model to cloud longwave radiative forcing. I: Introduction and initial experiments. *Quart. J. Roy. Meteor. Soc.*, **114**, 1027–1062.

Smagorinsky, J., 1963: GENERAL CIRCULATION EXPERIMENTS WITH THE PRIMITIVE EQUATIONS: I. THE BASIC EXPERIMENT. *Mon. Weather Rev.*, **91**, 99–164.

Spieß, T., J. Bange, M. Buschmann, and P. Vörsmann, 2007: First application of the meteorological Mini-UAV “M2AV.” *Meteorol. Z.*, **16**, 159–169.

Squires, P., 1958: The microstructure and colloidal stability of warm clouds. *Tellus*, **10**, 262–271.

———, and S. Twomey, 1960: The relation between cloud droplet spectra and the spectrum of cloud nuclei. *Washington DC American Geophysical Union Geophysical Monograph Series*, **5**, 211–219.

Storer, R. L., and S. C. van den Heever, 2013: Microphysical Processes Evident in Aerosol Forcing of Tropical Deep Convective Clouds. *J. Atmos. Sci.*, **70**, 430–446.

———, and D. J. Posselt, 2019: Environmental impacts on the flux of mass through deep convection. *Quart. J. Roy. Meteor. Soc.*, **145**, 3832–3845.

Straka, J. M., E. N. Rasmussen, and S. E. Fredrickson, 1996: A Mobile Mesonet for Finescale

Meteorological Observations. *J. Atmos. Ocean. Technol.*, **13**, 921–936.

Su, H., W. G. Read, J. H. Jiang, J. W. Waters, D. L. Wu, and E. J. Fetzer, 2006: Enhanced positive water vapor feedback associated with tropical deep convection: New evidence from Aura MLS. *Geophys. Res. Lett.*, **33**, <https://doi.org/10.1029/2005gl025505>.

Takahashi, T., and T. D. Keenan, 2004: Hydrometeor mass, number, and space charge distribution in a “Hector” squall line. *J. Geophys. Res.*, **109**, <https://doi.org/10.1029/2004jd004667>.

Takemi, T., 2007a: Environmental stability control of the intensity of squall lines under low-level shear conditions. *J. Geophys. Res.*, **112**, <https://doi.org/10.1029/2007jd008793>.

———, 2007b: A sensitivity of squall-line intensity to environmental static stability under various shear and moisture conditions. *Atmos. Res.*, **84**, 374–389.

———, 2014: Convection and precipitation under various stability and shear conditions: Squall lines in tropical versus midlatitude environment. *Atmos. Res.*, **142**, 111–123.

———, 2015: Relationship between Cumulus Activity and Environmental Moisture during the CINDY2011/DYNAMO Field Experiment as Revealed from Convection-Resolving Simulations. *Journal of the Meteorological Society of Japan. Ser. II*, **93A**, 41–58.

Themistocleous, K., 2017: The use of UAVs for monitoring land degradation. *Earth Resources and Environmental Remote Sensing/GIS Applications VIII*, Vol. 10428 of, Earth Resources and Environmental Remote Sensing/GIS Applications VIII, International Society for Optics and Photonics, 104280E (Accessed April 15, 2019).

Tobin, I., S. Bony, and R. Roca, 2012: Observational Evidence for Relationships between the Degree of Aggregation of Deep Convection, Water Vapor, Surface Fluxes, and Radiation. *J. Clim.*, **25**, 6885–6904.

Tompkins, A. M., 2001: On the Relationship between Tropical Convection and Sea Surface Temperature. *J. Clim.*, **14**, 633–637.

Toms, B. A., E. A. Barnes, E. D. Maloney, and S. C. Heever, 2020a: The global teleconnection signature of the madden-Julian oscillation and its modulation by the quasi-biennial oscillation. *J. Geophys. Res.*, **125**, <https://doi.org/10.1029/2020jd032653>.

———, S. C. van den Heever, E. M. Riley Dellaripa, S. M. Saleeby, and E. D. Maloney, 2020b: The Boreal Summer Madden–Julian Oscillation and Moist Convective Morphology over the Maritime Continent. *J. Atmos. Sci.*, **77**, 647–667.

Twomey, S., 1977: The Influence of Pollution on the Shortwave Albedo of Clouds. *J. Atmos. Sci.*, **34**, 1149–1152.

- Vincent, C. L., and T. P. Lane, 2016: Evolution of the Diurnal Precipitation Cycle with the Passage of a Madden–Julian Oscillation Event through the Maritime Continent. *Mon. Weather Rev.*, **144**, 1983–2005.
- Vömel, H., and Coauthors, 2018: The NCAR/EOL Community Workshop on Unmanned Aircraft Systems for Atmospheric Research - Final Report. *University Corporation For Atmospheric Research (UCAR):National Center For Atmospheric Research (NCAR):Earth Observing Laboratory (EOL)*, <https://doi.org/10.5065/d6x9292s>.
- Vorontsov, P. A., V. M. Mikhel, and A. A. Erler, 1958: *Utilization of Guided Model Airplanes for Aerological Investigations of the Lower Layers of the Atmosphere*. Glavnaia Geofizicheskaiia Observatoriia, Trudy,.
- Walko, R. L., and Coauthors, 2000: Coupled Atmosphere–Biophysics–Hydrology Models for Environmental Modeling. *J. Appl. Meteorol. Climatol.*, **39**, 931–944.
- van der Walt, S., and Coauthors, 2014: scikit-image: image processing in Python. *PeerJ*, **2**, e453.
- Warner, J., and S. Twomey, 1967: The Production of Cloud Nuclei by Cane Fires and the Effect on Cloud Droplet Concentration. *J. Atmos. Sci.*, **24**, 704–706.
- Waugh, S., and S. E. Fredrickson, 2010: An Improved Aspirated Temperature System for Mobile Meteorological Observations, Especially in Severe Weather. Vol. P5.2 of, 25th Conference on Severe Local Storms, Denver, CO  
[https://ams.confex.com/ams/25SLS/techprogram/paper\\_176205.htm](https://ams.confex.com/ams/25SLS/techprogram/paper_176205.htm) (Accessed April 3, 2019).
- Weickmann, K. M., 1983: Intraseasonal Circulation and Outgoing Longwave Radiation Modes During Northern Hemisphere Winter. *Mon. Weather Rev.*, **111**, 1838–1858.
- Weisman, M. L., and J. B. Klemp, 1982: The Dependence of Numerically Simulated Convective Storms on Vertical Wind Shear and Buoyancy. *Mon. Weather Rev.*, **110**, 504–520.
- Weisman, M. L., and C. A. Davis, 1998: Mechanisms for the Generation of Mesoscale Vortices within Quasi-Linear Convective Systems. *J. Atmos. Sci.*, **55**, 2603–2622.
- , and R. Rotunno, 2004: “A Theory for Strong Long-Lived Squall Lines” Revisited. *J. Atmos. Sci.*, **61**, 361–382.
- White, B. A., A. M. Buchanan, C. E. Birch, P. Stier, and K. J. Pearson, 2018: Quantifying the Effects of Horizontal Grid Length and Parameterized Convection on the Degree of Convective Organization Using a Metric of the Potential for Convective Interaction. *J. Atmos. Sci.*, **75**, 425–450.
- Wrenger, B., and J. Cuxart, 2017: Evening Transition by a River Sampled Using a Remotely-Piloted Multicopter. *Bound.-Layer Meteorol.*, **165**, 535–543.

- Wulfmeyer, V., and Coauthors, 2018: A New Research Approach for Observing and Characterizing Land–Atmosphere Feedback. *Bull. Am. Meteorol. Soc.*, **99**, 1639–1667.
- Xue, H., G. Feingold, and B. Stevens, 2008: Aerosol Effects on Clouds, Precipitation, and the Organization of Shallow Cumulus Convection. *J. Atmos. Sci.*, **65**, 392–406.
- Yang, S., and E. A. Smith, 2008: Convective–Stratiform Precipitation Variability at Seasonal Scale from 8 Yr of TRMM Observations: Implications for Multiple Modes of Diurnal Variability. *J. Clim.*, **21**, 4087–4114.
- Ye, H., E. J. Fetzer, S. Wong, and B. H. Lambrigtsen, 2017: Rapid decadal convective precipitation increase over Eurasia during the last three decades of the 20th century. *Sci Adv*, **3**, e1600944.
- Yoon, S., H. C. Lee, and T. H. Pulliam, 2016: Computational Analysis of Multi-Rotor Flows. *AIAA SciTech Forum*, 54th AIAA Aerospace Sciences Meeting, San Diego, CA, USA, American Institute of Aeronautics and Astronautics.
- Yuter, S. E., and R. A. Houze, 1995: Three-Dimensional Kinematic and Microphysical Evolution of Florida Cumulonimbus. Part II: Frequency Distributions of Vertical Velocity, Reflectivity, and Differential Reflectivity. *Mon. Weather Rev.*, **123**, 1941–1963.
- Zhang, H., and Coauthors, 2022: Development and application of a street-level meteorology and pollutant tracking system (S-TRACK). *Atmos. Chem. Phys.*, **22**, 2221–2236.
- Zhao, M., and P. H. Austin, 2005a: Life Cycle of Numerically Simulated Shallow Cumulus Clouds. Part II: Mixing Dynamics. *J. Atmos. Sci.*, **62**, 1291–1310.
- , and ———, 2005b: Life Cycle of Numerically Simulated Shallow Cumulus Clouds. Part I: Transport. *J. Atmos. Sci.*, **62**, 1269–1290.
- Zipser, E. J., and M. A. LeMone, 1980: Cumulonimbus Vertical Velocity Events in GATE. Part II: Synthesis and Model Core Structure. *J. Atmos. Sci.*, **37**, 2458–2469.
- Zipser, E. J., and K. R. Lutz, 1994: The Vertical Profile of Radar Reflectivity of Convective Cells: A Strong Indicator of Storm Intensity and Lightning Probability? *Mon. Weather Rev.*, **122**, 1751–1759.
- Zipser, E. J., D. J. Cecil, C. Liu, S. W. Nesbitt, and D. P. Yorty, 2006: WHERE ARE THE MOST INTENSE THUNDERSTORMS ON EARTH? *Bull. Am. Meteorol. Soc.*, **87**, 1057–1072.
- Zuluaga, M. D., and R. A. Houze, 2013: Evolution of the Population of Precipitating Convective Systems over the Equatorial Indian Ocean in Active Phases of the Madden–Julian Oscillation. *J. Atmos. Sci.*, **70**, 2713–2725.

Matrice 600 Pro Specs, FAQ, Tutorials and Downloads - DJI. *DJI Official*,  
<https://www.dji.com/matrice600-pro/info> (Accessed April 3, 2019).